

TIDAL DISSIPATION IN EXTRASOLAR PLANETS

by

Fernando Gabriel Peña

A thesis submitted in conformity with the requirements
for the degree of Doctor of Philosophy
Graduate Department of Astronomy & Astrophysics
University of Toronto

Copyright © 2010 by Fernando Gabriel Peña

Abstract

Tidal Dissipation in Extrasolar Planets

Fernando Gabriel Peña

Doctor of Philosophy

Graduate Department of Astronomy & Astrophysics

University of Toronto

2010

Many known extra-solar giant planets lie close to their host stars. Around 60 have their semi-major axes smaller than 0.05 AU. In contrast to planets further out, the vast majority of these close-in planets have low eccentricity orbits. This suggests that their orbits have been circularized likely due to tidal dissipation inside the planets.

These exoplanets share with our own Jupiter at least one trait in common: when they are subject to periodic tidal forcing, they behave like a lossy spring, with a tidal “quality factor”, Q , of order 10^5 . This parameter is the ratio between the energy in the tide and the energy dissipated per period. To explain this, a possible solution is resonantly forced internal oscillation. If the frequency of the tidal forcing happens to land on that of an internal eigenmode, this mode can be resonantly excited to a very large amplitude. The damping of such a mode inside the planet may explain the observed Q value.

The only normal modes that fall in the frequency range of the tidal forcing (\sim few days) are inertial modes, modes restored by the Coriolis force.

We present a new numerical technique to solve for inertial modes in a convective, rotating sphere. This technique combines the use of an ellipsoidal coordinate system with a pseudo-spectral method to solve the partial differential equation that governs the inertial oscillations. We show that, this technique produces highly accurate solutions when the density profile is smooth. In particular, the lines of nodes are roughly parallel to the ellipsoidal coordinate axes. In particular, using these accurate solutions, we estimate

the resultant tidal dissipation for giant planets, and find that turbulent dissipation of inertial modes in planets with smooth density profiles do not give rise to dissipation as strong as the one observed. We also study inertial modes in density profiles that exhibit discontinuities, as some recent models of Jupiter show. We found that, in this case, our method could not produce convergent solutions for the inertial modes.

Additionally, we propose a way to observe inertial modes inside Saturn indirectly, by observing waves in its rings that may be excited by inertial modes inside Saturn.

Acknowledgements

First of all my thanks go to my PhD supervisor, Dr. Yanqin Wu. Her support and encouragement even at difficult times helped me to keep working until the end. She has contributed with revisions, scientific discussions and suggestions in every chapter of this Thesis. During the couple of months prior to my defense, her massive editing was crucial to finish on time.

To my PhD committee members, Dr. Norm Murray and Dr. Ray Jayawardhana, whose fair criticism, scientific ideas and support was very helpful during all these years.

I also thank Dr. Marten van Kerkwijk, who supervised me during my first year research project. For his patience and incredible time availability even for answering the most annoying questions. I learned a lot of data reduction techniques and observations.

To Dr. Tristan Guillot for providing updated Saturn and Jupiter models.

And to many of the graduate students of UofT DAA; Rodrigo Fernandez, Daniela Goncalves, Santiago Gonzalez, Brian Lee, Duy Cuong Nguyen, Marija Stankovic and Sherry Yeh. And special thanks to the patience of Kaitlin Kratter, Hilding Neilson and Arabindo Roy with whom I spent quite some time discussing about science and getting help for the usual technical problems one experience during graduate school.

Finally to my thanks go to my family; father Rigoberto, mother Luz Marina, and brothers Alejandro and Roberto.

Contents

1	Introduction	1
1.1	Observations of Tidal Dissipation	1
1.1.1	Inside the Solar System	2
1.1.2	Outside the Solar System	4
1.2	Tidal Dissipation Theory: General	7
1.2.1	Timescales for orbital synchronization and circularization	7
1.2.2	The equilibrium tide vs dynamical tide	11
1.2.3	Recent estimations of Q due to dissipation in the dynamical tide .	14
1.3	Structure of a Giant Planet	16
1.4	Inertial Modes	18
1.5	Goal of This Thesis	20
2	Equation of Motion that Govern Inertial Modes	24
2.1	Equation of Motion in Vector form	24
2.2	Equation of Motion in Ellipsoidal Coordinates	28
2.3	Boundary Conditions	34
2.3.1	Surface	34
2.3.2	Equator	36
2.3.3	Polar Axis	36

3	Spectral and Pseudo-spectral Methods	37
3.1	Rational	37
3.1.1	Which Solver for the Partial Differential Equation?	37
3.1.2	Which Basis Function?	38
3.2	Preparatory Derivations	41
3.3	Spectral Method	43
3.3.1	The Non-separable Case	44
3.3.2	The Separable Case	47
3.3.3	A Test Run	54
3.4	Pseudo-spectral Method	54
3.4.1	Principles of the pseudo-spectral method	54
3.4.2	Implementation	60
4	Applications: Seismology using Saturn's Rings	62
4.1	Introduction	62
4.2	Exciting Waves in Disks by inertial Oscillations	66
4.2.1	Resonances and Waves	66
4.2.2	Resonant Torques	72
4.2.3	Unexplained Features in Voyager I data	75
4.3	Inertial Modes as Candidates	75
4.3.1	Solutions for Inertial modes	75
4.3.2	Torques by Inertial Modes	77
4.3.3	Results	81
4.4	Conclusions	85
5	Inertial Modes in a Polytrope Model	88
5.1	Solving for the Eigenvalue Problem	88
5.1.1	Finding Eigenvalues and Eigenvectors	89

5.1.2	Spurious Eigenmodes	91
5.2	Comparison with Previous Studies	96
5.3	Tidal Overlap Integrals and Implications on Tidal Damping	102
5.4	Possible Improvements	105
6	Density discontinuity inside Jupiter	108
6.1	Technical problems	109
6.1.1	1-d confined sound waves	114
6.2	The presence of a solid core	120
6.3	Future work	121
7	The Effect of the Compressional Term	123
7.1	Toy model of Goodman and Lackner (2009)	124
7.1.1	Tidal Overlap of Waves in the Toy Model	125
7.1.2	Tidal Excitation as an Initial Value Problem	127
7.2	Including Compressional Term for the Power-law Density Models	129
7.3	Summary	129
8	Conclusions and future work	132
	Bibliography	135

Chapter 1

Introduction

1.1 Observations of Tidal Dissipation

The effects of tidal interaction in the solar system were first studied in the seminal paper by Goldreich and Soter (1966). The presence of friction in the distorted body makes the high tide lead (lag) the disturbing object if the orbital period is longer (shorter) than the rotation period. The departure of perfect elasticity of the distorted body is measured by the tidal dissipation quality factor Q :

$$Q^{-1} = \frac{1}{2\pi E_0} \oint \left(-\frac{dE}{dt} \right) dt, \quad (1.1.1)$$

where E_0 is the maximum energy stored in the tide, and dE/dt the rate of dissipation¹. The integral is evaluated over a tidal period.

The relationship between Q and the angle Θ between the high tide and the orbiting body is:

$$Q^{-1} = \tan(2\Theta), \quad (1.1.2)$$

and since $Q \gg 1$, $Q^{-1} \sim 2\Theta$. For example, observations of the Earth-Moon tidal angle have shown that the Earth's tide is $\Theta_{Earth-Moon} = 2^\circ.16$ (MacDonald 1964) ahead of

¹Therefore Q is inversely proportional to the tidal dissipation efficiency.

Moon, which leads² to $Q = 13$.

1.1.1 Inside the Solar System

The orbital and rotational evolution of the bodies is controlled by the asymmetrical position of the tidal bulge with respect of the line that passes through their centers. In the orbiting plane, if the bulge leads the perturbing body ($\Theta > 0$), the near side of the bulge exerts a stronger force on the disturbing object. This creates a torque, which acts to transfer angular momentum and energy from the planet's rotation to the disturbing object's orbit. This effect is observed in our own Earth-Moon system (Mignard 1981), where the lunar semi-major axis increases at the expense of the Earth's rotation. The arrival times of laser beams sent to reflectors on the Moon surface³ have measured that the Earth-Moon distance increases about 3.8 cm/year (Lambeck 1988). The Earth raises tides in the Moon too, and that is what has caused the Moon's spin to become synchronized with the orbital period.

If the orbit is eccentric, the tidal torque on the planet mentioned above is larger at the pericenter than the apocenter. Impulses at the pericenter increase the apocenter distance without altering the pericenter distance (Goldstein et al. 2002). Because the greater impulse is exerted near pericenter, the net effect of the tidal torque is to increase the eccentricity, as well as the semi-major axis of the satellite's orbit. Besides torques, radial forces (parallel to the line that connect the centers of both objects) can also change the eccentricity (Goldreich and Soter 1966). If the Earth were synchronized to the orbital period of the Moon, but the orbit were not circular, the larger tide on the Earth would happen at the pericenter. Since there is no torque, there is no change in angular momentum, but the periodic distortion of the Earth due the eccentric orbit has

²For short-time scale studies, like the one in MacDonald (1964), Q can be assumed constant. However one have to notice that Q is probably dependent on the internal dynamical structure and also the tidal frequency.

³The reflectors, of about 48 cm^2 of surface area, were left on the Moon surface by the Apollo missions.

to dissipate energy, and therefore the eccentricity must decrease. A decreasing of the eccentricity is also expected when we calculate the radial distortion of the Moon due to the gravitational effect of an eccentric Earth, this mechanism is expected to be dominant also in the circularization of hot-Jupiters.

Mercury and Venus are the closest planets to the Sun and have no satellites orbiting them. Therefore we can consider the systems Sun-Mercury and Sun-Venus as the only cause of tidal effects on the planets. Mercury currently rotates with a period of 58 days, and in order to slow it down to that period, tidal spindown needs to be taking into account. However its current orbital period (88 days) shows a mayor deviation from synchronism. Instead it was discovered that the system is in a 3:2 spin-orbit resonance (Colombo 1965). Simulations indicate that the orbital eccentricity of Mercury changes in the range of $0 < e < 0.45$ in a timescale of millions of years due perturbations from other planets (Correia and Laskar 2009), which may explain the current state of resonance as it is likely to happen in a period of high eccentricity (Correia and Laskar 2004). In the case of Venus, the evidence of tidal dissipation does not confirm the expected effect of the Sun on its rotation: Venus has a retrograde rotation with a period of -243 days (orbital period being 224 days) attributed to its early evolutionary stage of initial rotation and obliquity (Correia et al. 2003).

Mars is outside the tidal influence from the Sun⁴, but it has two satellites, Phobos and Deimos. The inertia of these objects are so small that they barely affect the spin of the planet, but Mars does affect the orbital evolution of the satellites. In the case of Phobos, the satellite has an orbital period shorter than the spin of the planet, the reverse of the system Earth-Moon. The high tide of Mars lags behind Phobos, and therefore orbital angular momentum is transferred from the satellite to the planet (Goldreich and Soter 1966), making Phobos spiral in towards Mars (Raine and Aharonson 2006).

The outer gaseous planets are massive with respect to their moons and tend to have

⁴The Sun raises a tide in Mars of height $h \sim 3$ cm.

many of them. Therefore it is possible to study the evolution of the orbital elements of the satellites in order to study the tidal effects.

Since gaseous planets like Jupiter rotate very fast ($P_J \sim 10$ hrs), the transfer of angular momentum is therefore from the planet's rotation to the satellite orbit. At the same time, the rotational angular momentum of the satellites is so small that one can expect synchronization in all the satellites, and the vast majority of the Solar System satellites for which rotational periods have been measured show synchronization. Lainey et al. (2009) has studied almost a century of astrometric data for the Galilean moons, finding that $Q_J \approx 4 \times 10^4$, the net effect of the angular momentum transfer from Jupiter's rotation to the Galilean moons motion, is that the semi-major axis increases with time. Since Kepler's law establish that $n^2 r^3 = GM$ an increase in the satellites distance implies deceleration of their orbits, a measurable quantity.

For the next set of outer planets, there are no accurate measurements of tidal dissipation on the planets. It is logical to think that tides raised on Saturn, Uranus and Neptune affect the orbital elements of their satellites. Constraints on Q can be obtained -assuming that it is constant- as the satellites are permanently pushed away from the planets. One can argue (Goldreich and Soter 1966) that there is a minimum Q (proportional to the time scale of the orbital expansion) for which a satellite released from the planet's surface reaches its actual location during the age of the Solar System. A smaller Q (meaning a more efficient dissipation) would imply that the actual location of the satellite would be further away.

1.1.2 Outside the Solar System

In stars, tidal effects can be seen on short and long time scales. For binary stars with orbital periods of a few days we can observe the direct effects of the tidal deformation through photometry and spectroscopy. The projected surface area and thus flux from one or both components becomes a function of time. Kopal (1959) calculates this ellipsoidal

effect while assuming that the components are synchronized and the orbits circularized Zahn (1977a). For main sequence stars orbiting with periods of a few days the fractional variation of the flux of one component is of the order of few percent.

Long term tidal effects can be extrapolated from solar type binaries. These effects change the orbital elements of the system and rotation of the components in timescales of millions or billions of years (Zahn 1975). Figure 1 in Mayor and Mermilliod (1984) shows the distribution of 33 solar-type main-sequence spectroscopic binaries in a eccentricity vs period plot. The eccentricities of the binaries suffer a marked change at around a period of 5.7 days. All the binaries with periods shorter than this critical period have circular orbits ($e \ll 0.05$), while binaries with longer periods show a scattered distribution of eccentricities. Similar behavior but with different transition periods have been presented in works by Duquennoy and Mayor (1991) and Meibom and Mathieu (2005). The behavior suggest that the efficiency of the circularization is a function of the period, or, semi-major axis (Zahn 1975), i.e., the larger the separation the longer the time scale for circularization. It is still a matter of debate how to understand the fact that the transition period seems to change with different samples of main-sequence binary stars (Mazeh 2008).

Early-type binaries also show a similar behavior as the main sequence sample of Mayor and Mermilliod (1984). The theory of Zahn (1975) predicts that the circularization time-scale of stars with radiative envelopes is larger compared to tidal dissipation in stars with convective envelopes, due to other dissipation mechanisms. Turbulent viscosity in the convective envelopes is more efficient than radiative damping in the radiative envelopes (Zahn 1977b). However Giuricin et al. (1984) have acquired a sample of around 200 spectroscopic and eclipsing binaries that have an early-type star as a primary. They have found out that most of the binaries with periods shorter than 2 days are circular, and that there is an upper envelope ‘in eccentricity’ that goes up to an eccentricity of 0.6. This ‘envelope’ is also present in late-type binaries and can be given the interpretation

that the binaries formed above the envelope have been pushed down inside the envelope by the circularization process (Mazeh 2008).

Tidal forces also tend to synchronize the rotation of the binary components with the orbital period. Witte and Savonije (2002) predict that the synchronization timescale will be two or three orders of magnitude shorter than circularization timescale. The fact that the angular momentum associated with the orbital motion is larger than the one associated with the rotation allows the system to synchronize more quickly. Observing this effect is difficult as stellar rotation is not well defined yet, and observational measurements of rotation show large uncertainties. Mazeh (2008) in Figure 4 shows a sample of 6 young stars that have been synchronized.

Extrasolar hot-Jupiters and Jupiter are thought to be very similar in composition. However their evolution has been significantly different, as it is thought that hot-Jupiters reach their current orbits ($a \leq 0.05$ AU) either after tidal interactions with the protostellar disk (Moorhead and Adams 2007), or by interactions with other undetected planets (Zhou et al. 2007). Once they are close to the host-star the tidal interaction starts to take control and at the same time the planet can develop a radiative envelope (see §1.3). As in the case of stars, one can also produce an eccentricity vs period (or semi-major axis) plot from the spectroscopic signal of the host-star, like the one in Figure 1.1 (Data taken from the Extrasolar Planets Encyclopedia⁵), and find signs of orbital circularization. Most of the planets with periods shorter than 2.5 days (hot-Jupiters) have circular orbits while planets with longer periods show a scatter with an envelope that raises to an eccentricity of 0.8. Signs of synchronization can be also be traced as a planet that shows its ‘same face’ to the host-star should have the correspondent hemisphere exposed to the intense radiation field of the host, causing a significant difference between day and night temperatures. This effect can be either seen as a phase modulation if the IR photometry in non-transiting planets (Seager et al. 2005) or as IR emission of the day-side of

⁵<http://www.obspm.fr/encycl/encycl.html>.

the eclipsing planets HD 209458b (Deming et al. 2007) and TrES-1 (Charbonneau et al. 2005).

1.2 Tidal Dissipation Theory: General

1.2.1 Timescales for orbital synchronization and circularization

In section 1.1 we introduced the tidal quality factor, and show that observations of stars, planets, and natural satellites, in some cases show signs of tidal dissipation. We use order of magnitude theory to derive the tidal synchronization time-scale and the tidal circularization time-scale.

In order to understand the tidal synchronization of an object like the Moon, one can derive the synchronization time scale using the fact that the change in the spin is related to the torque on the Moon by the Earth as $\Gamma = I d\Omega_{rot}/dt$, where I is the moment of inertia of the Moon (assumed constant).

In the absence of synchronization, a tide raised on the Moon by the Earth exerts a torque that can be thought of as the torque along a rod that has its rotation axis at the center of the planet, and at each end the rod has masses of the order of the tidal bulge δM . There is an lag angle between the rod and the line that connects the centers of rotation of the two bodies. The bulge that is closer to the Earth feels a stronger torque than the bulge at exactly the opposite side. An estimation of the differential force between both bulges is:

$$\Delta F \approx -\delta M \frac{GM_{\oplus} R_{Moon}}{d_{Earth-Moon}^3}. \quad (1.2.1)$$

The net torque is therefore:

$$\Gamma \approx \Delta F R_{Moon} \sin \Theta. \quad (1.2.2)$$

Assuming that the density of the Moon is constant the mass in the bulge is simply $\delta M \approx M_{Moon}(h/R_{Moon})$, where h is the height of the tide. The height can be estimated

when the surface gravity of the bulge balances the differential acceleration of the bulge.

This implies:

$$\rho Gh \approx \frac{GM_{\oplus}R_{Moon}}{d_{Earth-Moon}^3}, \quad (1.2.3)$$

and since $\rho \approx M_{Moon}/R_{Moon}^3$ the height is:

$$h \approx \frac{M_{\oplus}}{M_{Moon}} \left(\frac{R_{Moon}}{d_{Earth-Moon}} \right)^3 R_{Moon}. \quad (1.2.4)$$

Therefore the net torque is:

$$\Gamma \approx -\frac{GM_{\oplus}^2}{R_{Moon}} \left(\frac{R_{Moon}}{d_{Earth-Moon}} \right)^6 \sin \Theta. \quad (1.2.5)$$

The moment of inertia is $I \approx \alpha_{Moon}M_{Moon}R_{Moon}^2$, where α_{Moon} is a constant. The deceleration of the Moon $d\Omega_{rot}/dt$ is:

$$\frac{d\Omega_{rot}}{dt} = -\frac{G}{\alpha_{Moon}M_{Moon}R_{Moon}^2} \left(\frac{M_{\oplus}^2}{R_{Moon}} \right) \left(\frac{R_{Moon}}{d_{Earth-Moon}} \right)^6 \sin \Theta. \quad (1.2.6)$$

As we mentioned in section 1.1, the tidal dissipation quality factor is related to the lag angle as $Q^{-1} \approx \tan(2\Theta) \approx 2 \sin(\Theta)$. We can estimate the characteristic synchronization time scale as:

$$\frac{1}{\Omega_{rot}} \frac{d\Omega_{rot}}{dt} = \frac{1}{\tau_{sync}}. \quad (1.2.7)$$

Dividing equation (1.2.6) by Ω_{rot} we finally obtain the synchronization timescale:

$$\frac{1}{\tau_{sync}} = \frac{G}{\alpha_{Moon}\Omega_{rot}R_{Moon}^3} \left(\frac{M_{\oplus}^2}{M_{Moon}} \right) \left(\frac{R_{Moon}}{d_{Earth-Moon}} \right)^6 \frac{1}{Q_{Moon}}. \quad (1.2.8)$$

The actual derivation gives (Murray and Dermott 2000):

$$\frac{1}{\tau_{sync}} = \frac{3Gk_{2Moon}}{2\alpha_{Moon}\Omega_{rot}R_{Moon}^3} \left(\frac{M_{\oplus}^2}{M_{Moon}} \right) \left(\frac{R_{Moon}}{d_{Earth-Moon}} \right)^6 \frac{1}{Q_{Moon}}, \quad (1.2.9)$$

where k_{2Moon} is the tidal Love number. For the Moon (Yoder 1995) $k_{2Moon} = 0.030$, $Q = 13$, $\alpha_{Moon} \approx 2/5$ and therefore $\tau_{sync} = 7 \times 10^7$ years. Therefore, the torques over the tides raised on the Moon by the Earth are strong enough to explain the lunar synchronization.

For tidal circularization of the orbiting body (eg, the Moon, an exoplanet), we refer to the work of Hut (1981). To estimate the tidal circularization time scale, we assume some eccentricity in the system and perfect synchronization of the Moon. When synchronized there is no net torque due to a tide raised by the Earth. However, tidal dissipation exists, as the differential radial force between the center and the surface of the Moon changes during the orbit, being this effect larger at the pericenter. The orbital angular momentum⁶ L is:

$$L^2 = G \frac{M_{\oplus}^2 M_{Moon}^2}{M_{\oplus} + M_{Moon}} a(1 - e^2). \quad (1.2.10)$$

If L is constant:

$$\frac{1}{a} \frac{da}{dt} = \frac{2e}{(1 - e^2)} \frac{de}{dt}. \quad (1.2.11)$$

The energy dissipated by the lunar tide is extracted from the orbit, $E_{orb} = -GM_{\oplus}M_{Moon}/2a$, and therefore:

$$\frac{dE_{orb}}{dt} = \frac{GM_{\oplus}M_{Moon}}{2a} \frac{1}{a} \frac{da}{dt}, \quad (1.2.12)$$

and since $\dot{E}_{orb} < 0$, $\dot{a} < 0$ and so $\dot{e} < 0$. Therefore tides raised on a satellite (less massive companion), when dissipated, circularize the orbit.

In order to estimate the energy dissipated we can estimate the work done by the satellite (of orbital frequency ω) on the tide. Dissipation introduces a delay in the amplitude and direction of the tide, the time-dependent part being of the order of $\cos(\omega t + \epsilon)$, where ϵ accounts for the phase difference between the fluid response and the force ($\propto \sin(\omega t)$), this phase is analogous to Θ the lag angle where the satellite is not synchronized. The work is given by:

$$\Delta E_{orb} = \oint_{orbit} \mathbf{F}_r \cdot d\mathbf{r} = \oint_{orbit} F_r \frac{dr}{dt} dt, \quad (1.2.13)$$

where F_r is the tidal radial force. Since the radial velocity of the fluid on the Moon is of the order $\dot{r} = eR_{Moon}\omega \sin(\omega t)$ and $F_r \approx eGM_{\oplus}\delta M_{Moon}R_{Moon}a^{-3} \cos(\omega t + \epsilon)$ the work

⁶Much larger than the rotational angular momentum.

is:

$$\Delta E_{orb} \approx e^2 \frac{GM_{\oplus} \delta M_{Moon} R_{Moon}}{a^2} R_{Moon} \omega \oint_{orbit} \sin(\omega t) \cos(\omega t + \epsilon) dt, \quad (1.2.14)$$

here we have introduced a factor e in both the force and the velocity to account for the part that actually varies when e is non-zero (there is always a constant part that does not change with time).

The integral results in a factor of $\sin \epsilon / (2\omega)$. The tide raises a bulge of height h on the Moon and mass:

$$\delta M_{Moon} = \left(\frac{h}{R_{Moon}} \right) M_{Moon}, \quad (1.2.15)$$

and therefore:

$$\Delta E_{orb} = e^2 \frac{G M_{\oplus} M_{Moon} h}{2 a^2} R_{Moon} \sin \epsilon \quad (1.2.16)$$

Since the height of the tidal bulge is:

$$h = R_{Moon} \frac{M_{\oplus}}{M_{Moon}} \left(\frac{R_{Moon}}{a} \right)^3. \quad (1.2.17)$$

the work done is:

$$\Delta E_{orb} = e^2 \frac{GM_{\oplus}^2 R_{Moon}^5}{2 a^6} \frac{1}{Q}, \quad (1.2.18)$$

where we have adopted $\sin \epsilon = Q_{Moon}^{-1}$.

The average rate of energy loss, is the work (eq. 1.2.18) divided by the orbital period ($\sim \omega^{-1}$) so that:

$$\frac{dE_{orb}}{dt} = -e^2 \frac{GM_{\oplus}^2 R_{Moon}^5 \omega}{2 a^6 Q}. \quad (1.2.19)$$

Replacing eq. (1.2.19) and (1.2.12) in eq. (1.2.11) we finally obtain (for $e \ll 1$):

$$\frac{1}{e} \frac{de}{dt} = -\frac{1}{2} \left(\frac{M_{\oplus}}{M_{Moon}} \right) \left(\frac{R_{Moon}}{a} \right)^5 \frac{\omega}{Q_{Moon}}. \quad (1.2.20)$$

The actual derivation of \dot{e} , for small eccentricities is (Hut 1981):

$$\frac{1}{e} \frac{de}{dt} = -\frac{27k_{2Moon}}{Q_{Moon}} \left(\frac{M_{\oplus}}{M_{Moon}} \right) \left(\frac{R_{Moon}}{a} \right)^5 \omega, \quad (1.2.21)$$

The circularization time-scale is just the inverse of equation (1.2.21) and therefore, $\tau_{circ} = 2 \times 10^{10}$ years. The values of k_{2Moon} and Q_{Moon} are from Yoder (1995).

1.2.2 The equilibrium tide vs dynamical tide

The equilibrium tide (Goldreich and Soter 1966) is based on a model in which a spherical body continually adjusts to maintain a state of quasi-hydrostatic equilibrium in the varying gravitational potential of its orbital companion. Internal friction within the body induces dissipation of energy and a phase lag, which gives rise to a net tidal torque that transports angular momentum between the spin of the body and its companion and their orbits.

In the case of gas giant planets (Goldreich and Nicholson 1977), turbulent dissipation of equilibrium tides dissipates energy. The kinetic energy of large scale flows cascades down to smaller and smaller scales until it is dissipated into heat. When turbulence exists, the time scale for the dissipation is of the order $\tau_{conv} = R^2/\nu_t$, where ν_t is the effective turbulent viscosity. In Jupiter, convection is the cause of turbulence. Goldreich and Nicholson (1977) proposed that only the eddies which have a turnover lifetime of less than the tidal period $2\pi/\omega_{tide}$ exchange momentum with the mean flow on that timescale. They conclude that, over the bulk of the planet, the mass average turbulent viscosity is of the order $\langle \nu_t \rangle \sim 10^3 \text{ cm}^2\text{s}^{-1}$, and therefore the viscous time scale exceeds the age of the Universe. Hubbard (1974) estimated Q in the equilibrium tide of Jupiter:

$$Q_J = \frac{GM}{2\omega R} \frac{1}{\langle \nu_t \rangle}, \quad (1.2.22)$$

which predicts $Q_J \sim 10^{13}$, eight orders of magnitude larger than the observed $Q_J \sim 4 \times 10^4$ (Lainey et al. 2009).

The dynamical tide is present when the varying tidal potential of the companion resonantly excites radial and non-radial oscillations in the body. Inside gravitating rotating fluids, there are mainly three modes of oscillations. Pressure-restored (acoustic) ‘p-modes’, whose characteristic frequency (of the lowest order mode) is c_s/R , where c_s is the characteristic sound speed and R the radius of the body. Buoyancy restored modes or ‘g-modes’, are those whose characteristic frequency is the *Brunt – Väisälä* frequency

(Unno et al. 1989):

$$N = \left[g \left(\frac{1}{\Gamma_1} \frac{d \ln p}{dr} - \frac{d \ln \rho}{dr} \right) \right]^{1/2}, \quad (1.2.23)$$

where Γ_1 is the adiabatic index, g acceleration due to gravity, p the pressure, ρ the density and r the distance from the center. The last type are Coriolis-restored modes or ‘inertial-modes’, whose frequencies are in the range of $[0, 2\Omega_{rot}]$, where Ω_{rot} is the frequency of rotation.

In the Sun the p-modes have a characteristic period of $P_{p-mode} \sim 5$ minutes near the surface, g-modes have $P_{g-mode} \sim 1$ hour, and inertial-modes $P_{inertial-mode} \sim 25$ days.

We are interested in the dissipation by the dynamical tide in Jupiter and hot-Jupiters. Tides are raised in Jupiters by its moons, the main tidally disturbing bodies being the Galilean moons (due their large masses compared to any other Jovian moons). In the rotating frame of Jupiter (not synchronized with the moons), the tide has a frequency of $\omega_{tide} = \Omega_{rot} - \omega_{orb} \sim \Omega_{rot}$, and therefore normal modes in the frequency range (periods) of the order Ω_{rot} (10 hours) are candidates to be excited near resonance. Jupiter is mainly convective, meaning $N \approx 0$, and so g-modes are not possible. The lower order p-modes have periods of 30 minutes (with high order p-modes having shorter periods), whis is far too short to be excited. However the frequencies of inertial modes are in the range of the rotational frequency, and so they are a strong candidate for tidal dissipation in the dynamical tide. The oscillations are dissipated by the means of turbulent convection. Even if the estimated turbulent viscosity (Goldreich and Nicholson 1977) is very small, resonant excitation of inertial modes can dissipate enough energy over the age of the system, as the energies of the oscillations scale as the square of the amplitude. The inertial mode spectrum is dense in the frequency range of $[0, 2\Omega_{rot}]$. In the case of hot-Jupiters, it is likely that they are synchronized with their orbits⁷, i.e., $\Omega_{rot} \approx \omega_{orb}$. However, as we mentioned earlier, when the orbit is not circular, there exist a radial tide

⁷Jupiter and hot-Jupiters are likely to be similar, except for a radiative envelope and a larger radius due to both irradiation and tidal heating (Guillot 2005). Therefore, from the observations we can conclude that $Q_{hot-J} \sim Q_J$, small enough for them to become synchronized.

with a frequency comparable to ω_{orb} , and therefore inertial modes are also candidates for eccentricity damping.

In the case of the existence of a radiative layer, more likely to be present in exoplanets orbiting their host stars at distances of $a \lesssim 0.05$ AU, a tidal perturbation of a period of days can also induce resonant g-mode oscillations of high order ($N \sim g/c_s \sim 0.03$ s⁻¹), which can carry both energy and angular momentum (Cowling 1941). The g-mode oscillations can be dissipated by radiative damping, i.e., they travel adiabatically to the stellar surface where both the wave and angular momentum carried by it are dissipated and transferred respectively.

Since extrasolar planets with $a < 0.07AU$ ($P < 6$ days) have $e \approx 0$, and in outer regions they exhibit a scatter in their eccentricities (Figure 1.1), we can assume that the circularization timescale is similar as the age of the host star (roughly few Gyrs. for the planet-host's stars). And since the mass-radius relation around Jupiter's mass is almost a constant ($R \propto M^0$), exoplanetary radius does not change that much with mass (Guillot 2005). Therefore radial velocity measurements and an estimation of the stellar mass can lead us to infer Q_p . Moreover, observing the shaded regions of Figure 1 in Wu (2003) one can see that the observed upper envelope of planet eccentricity as a function of a can be explained by a tidal quality factor $Q_p \approx 3 \times 10^5$ if these are gaseous planets similar to Jupiter in their ages and sizes. The circularization timescale is:

$$\frac{1}{\tau} = \frac{1}{e} \frac{de}{dt} = -\frac{27k_2}{2Q_p} \left(\frac{M_*}{M_p}\right) \left(\frac{R_p}{a}\right)^5 \omega,$$

where k_2 , Q_p , and R_p are the tidal Love number, tidal Q – value and radius of a planet, orbiting a star of mass M_* with semi-major axis a and orbital frequency ω .

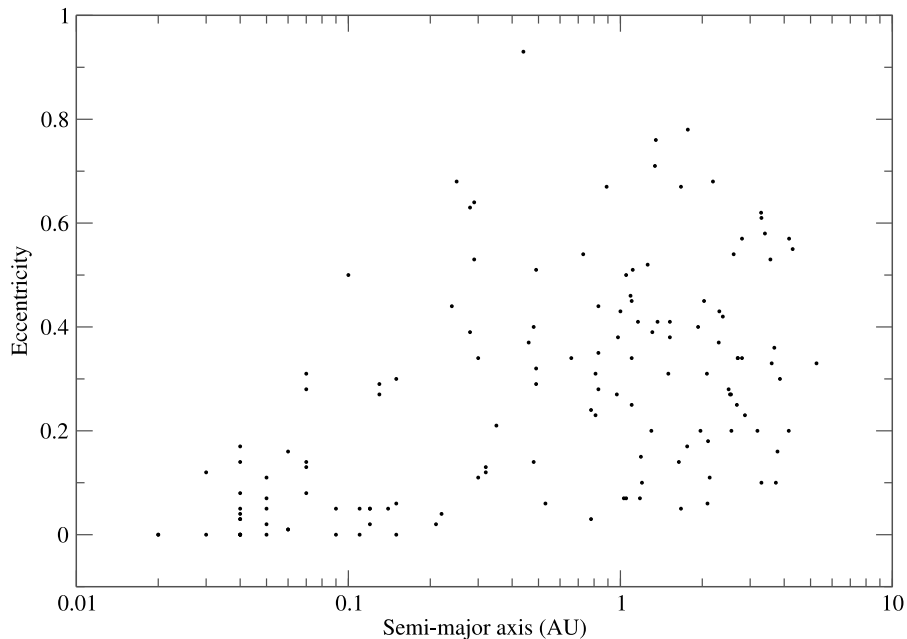


Figure 1.1 Eccentricity vs semi-major axis for all known extrasolar planets (up-to-date). Source of data taken from the extrasolar planets encyclopedia (<http://www.obspm.fr/encycl/encycl.html>).

1.2.3 Recent estimations of Q due to dissipation in the dynamical tide

As we have shown, dissipation on the equilibrium tide can not account for the observational constraint to Q_p , therefore most of the research of the last 3 decades has been focused on the dynamical tide. Here we mention two “recent” attempts to estimate Q in Jupiter.

Ogilvie and Lin (2004) studied, using a numerical code, the forced excitation of inertial and g free waves inside rotating planets whose interiors include a solid core, a convection zone and a radiative atmosphere. Their results are reasonable for the case of Jupiter and Saturn, with $Q_p \approx 10^5$ when using a polytrope of index $n = 1$, a solid core of about 10% of

the planet, and a convective and small radiative regions that accounts for the remaining 90 %. In that model the dissipation is due to turbulent viscosity in the convective region, and via the emission of Hough (1897) waves at the convective-radiative boundary. The viscosity has been greatly enlarged (roughly 10 orders of magnitude greater) because the lack of numerical resolution at realistic microscopic viscosities (Guillot et al. 2004). Q_p values in their models seem to be independent of viscosity, questionable to the physical sense. We can also speculate that different equations of state may produce different tidal responses (which depends on the density and its fluctuations), since the radial parts of the outward propagating waves may be reflected depending on their frequencies and the latitude at which they arrive at the outer interface between the inertial modes in the convective zone and g-modes in the atmosphere (similar to Snell’s internal reflection in optics).

In a different approach Wu (2005a) and Wu (2005b) studied tidal dissipation of inertial modes (standing waves) resonantly excited by the harmonic tidal potential. Wu (2005a) performed a semi-analytical analysis of inertial modes in rotating neutrally-buoyant spheres, where the only restoring force is Coriolis. For a general density profile approximate solutions to the inertial modes, “accurate to second order in wave vector”, are obtained. Later Wu (2005b) couple the inertial modes to the disturbing tidal potential of an external body (i.e., a satellite or a star), using mixing length theory to study the dissipation of these modes by turbulent dissipation (since the results were analytical, handling of low turbulent viscosity was possible). Because these studies involved only inertial modes, the results are applicable to bodies that are fully convective like Jupiter (as long as the core is very small compared to the wavelength of the modes). Depending on the actual (and somewhat unknown) equation of state, Wu (2005b) obtained⁸ $Q_J \approx 10^7 - 10^9$, a factor $10^2 - 10^4$ above the actual Q_J . In this model, Q_J depends on

⁸Oscillatory g-modes are not possible in convective spheres, although they may be important for tidal dissipation in the convective-radiative boundary.

viscosity and tidal frequency, as one may expect. It seems improvement to this theory is needed to confirm that inertial modes are the dominant tidal dissipation mechanism.

Regardless of the approach, these are hints that the dynamical tide may be responsible for the observed Q_p in solar and extrasolar planets. Therefore, it is important to develop a theory that involves as much realistic planetary physics as possible, in order to understand how exoplanets evolve dynamically, and perhaps how tidal dissipation of this kind in *stars* contribute to circularization and braking mechanism for inward planetary migration.

1.3 Structure of a Giant Planet

In order to build an interior model of a giant planet, it is imperative to know the equation of state (EOS) of matter at high pressures and low temperatures.

Jupiter is made of mostly of hydrogen and helium, reaching pressures above 1 Mbar and temperatures that range from hundreds of K in the surface to 30,000 K in the center. The equation of state has been investigated by many different authors. The EOS of Saumon et al. (1995) (usually known as SCVH) deals with plasmas of hydrogen and helium separately at high densities. The technique used was ‘*free-energy minimization*’ where the interaction among atoms and molecules is made through a pair potential, keeping the identities of the particles involved. Any mixtures of hydrogen and helium were treated as additive and weighted contributions to the free-energy, neglecting the interaction potential that otherwise would complicate the calculations.

Saumon et al. (1995) also show that above certain densities, the mean distance between atoms becomes comparable to the Bohr radius, and therefore the electrons are forced to unbound states making the fluid a pressure-ionized plasma. Their calculations showed that this pressure-ionization of hydrogen (also known as ‘metallic hydrogen’) may happen sharply, through a discontinuous first-order phase transition⁹, also called

⁹Meaning that all thermodynamic quantities are discontinuous except for the pressure, the temperature and chemical potentials.

“plasma phase transition” or PPT. There is no current experimental evidence for or against this transition, and therefore (Saumon et al. 1995) also produce models that consider continuous phase transitions through interpolation (smoothing-out) of all the previously discontinuous variables.

Guillot (1999) produced a ‘3-layer’ Jupiter and Saturn model. In this model the interiors of the planets were divided into an inner solid core region, an inner-intermediate metallic hydrogen region and an outer molecular hydrogen region. Guillot (1999) improved Saumon et al. (1995) EOS by adding ‘ices’ (CH_4 , NH_3 and H_2O) and ‘rocks’ (Fe, Ni, MgO and SiO_2) to the region of the EOS that considers the core.

Although in many other EOS (Saumon et al. 1995; Stevenson and Salpeter 1977) giant planet interiors are convectively unstable¹⁰, uncertainties in hydrogen, helium, methane, water and ammonia Rosseland opacities may allow for the existence of outer radiative layers (Guillot et al. 1994).

In order to test the interior models of Jupiter and Saturn, they had to match accurately known values, e.g.; the equatorial radius R_{eq} , at the known rotational frequency Ω_p and mass M_p , and the quadrupolar moment of inertia J_2 . Less accurately known values of J_2 and the average helium mass fraction \bar{Y} can also be used to constrain the structure of these planets.

In the case of hot-Jupiters ($a \leq 0.1$ AU), irradiation from the host star is 10^4 times larger than their intrinsic cooling energy flux, and therefore a radiative zone is likely to be present controlling the cooling of the planet (Guillot et al. 1996). This radiative region can extend as far as 5% in radius and 0.3% in mass (Guillot and Showman 2002). Guillot et al. (1996) calculate the effect of cooling through a radiative atmosphere. In order to do that the (molecular) opacity setups for exoplanets were built in a similar way as “AMES-cond” and “AMES-dusty” models atmospheres of Allard et al. (2001). These opacities refers

¹⁰Using the Schwarzschild criterion for convection, which is equivalent to a *Brunt – Väisälä* frequency $N < 0$.

to two limiting cases, when dust forms in the atmosphere, at locations determined by the chemical equilibrium equations, but has been entirely removed from the atmosphere by efficient gravitational settling¹¹, and when settling is ignored altogether leaving dust present on the atmosphere and therefore contributing to the opacity.

1.4 Inertial Modes

Inertial modes are oscillations where the Coriolis force is the main restoring force, and therefore they only occur in rotating fluids. In the Earth we observe them in the atmosphere as Rossby waves (Greenspan 1980) and geostrophic winds (jets), and in the oceans as geostrophic currents. In that context these modes are usually confined to spherical shells. They have not been confirmed in the astrophysical context.

Work on inertial modes in rotating spheres (or spheroids) can be traced back to Poincaré (1885), who obtained the differential equations for the oscillations of a rotating and gravitating inviscid fluid, and later Bryan (1889), who studied Poincaré's oscillations in a uniform-density spheroid of finite ellipticity (an *ellipsoid*). Bryan (1889) used a coordinate transformation under which the differential equation that governs the oscillations becomes separable. The eigensolutions were exactly described by the associated Legendre polynomials, and the eigenfrequencies in the rotating frame were constrained between zero and twice the angular frequency of the spheroid.

In the astrophysical context, Papaloizou and Pringle (1978) studied g- and r-modes (pure toroidal, odd-parity, retrograde inertial modes) in a rotating spherical star and their applicability to the short period oscillations of cataclysmic variables. They used the variational method and the expansion of the eigenfunction in a well chosen basis in an equipotential coordinate system.

Lockitch and Friedman (1999) studied r-modes in isentropic stars in the absence of

¹¹Therefore not contributing to the overall opacity

viscosity and without a solid core for arbitrary polytropic density profile. Their aim was to study the spin evolution of rapidly rotating neutron stars. They used spectral methods to find the eigenfunctions. In spherical isentropic stars, the gravitational restoring forces that give rise to g-modes vanish. The Coriolis force term then produces the pure axial r-modes studied by Papaloizou and Pringle (1978), and mixed axial-polar modes (generalized r-modes), known as inertial modes. They used inertial mode solutions in the sphere where the angular part is an expansion in a basis of spherical harmonics. Stars of Solar mass (or lighter), and giant planets are likely to be convective except for the external atmosphere. Inertial modes, must be always present in these type of objects.

Lee et al. (1992a) investigated inertial modes in Jupiter using different interior models, in particular models that include the molecular-metallic hydrogen phase transition. Using the spherical coordinate system they expanded the angular part of the solutions in terms of the spherical harmonics $Y_l^m(\theta, \phi)$. Whereas the treatment of the boundary conditions around the phase transition was novel, their approach was limited by lack of resolution, since they have used no more than three spherical harmonics.

Later Dintrans and Ouyed (2001), using modern numerical tools, demonstrate the limitations of Lee et al. (1992a) after the inclusion of as many spherical harmonics as needed before spectral convergence is achieved. However they only tested a simple polytropic interior model of index $n = 1$. The inclusion of a phase transition remains as a puzzle.

Ogilvie and Lin (2004) studied tidal dissipation in rotating giant planets that include a solid core, a large convective region harboring inertial modes, and a radiative zone, where Hough modes (Coriolis modified g-modes) are possible. They modeled inertio-gravity waves forced by the harmonic tidal potential. Their aim was to explain the observed circularization of the orbits of short-period extrasolar planets and the current state of the Galilean satellites. The numerical solutions for the 2-D problem were obtained by two independent methods. A Chebyshev pseudo spectral approach (similar to the

one we implement later in this Thesis), that provides highly accurate eigenfunctions, and direct integration of the differential equations, using a fifth-order Runge-Kutta method.

In all of the previous works finding the periods and solutions for the eigenfunctions has been a very difficult task, since the partial differential equation governing them is non-linear, and therefore it is very difficult to use separation of variables. The traditional spherical description of the solution (a linear combination of spherical harmonics) is no longer helpful as the solution is composed of many (maybe infinite) spherical harmonics (Schenk et al. 2002). In general, for the traditional 3-D axisymmetric problem, we can assume that the solution has terms proportional to $e^{im\phi}$; however, the set of eigenvectors generally couple a considerable number of them.

Wu (2005a) solved the same problem as Ogilvie and Lin (2004), although the author studied pure inertial modes without the inclusion of a solid core and a radiative layer. Wu's approach is based on the same coordinate transformation that Bryan (1889) used for constant density ellipsoids. However, the author found that by using a power law density structure of the form $\rho = (1 - r^2)^\beta$, the differential equation is separable. Direct integration of the inviscid ODEs produced eigenfunctions and frequencies.

1.5 Goal of This Thesis

In chapter 2 we present the derivation of the partial differential equation that have, in combination with the boundary conditions, inertial mode solutions. In order to do that, we follow Wu (2005a) description, highlighting some of the assumptions that simplify the equations, and explain why we make them. Also crucial for the derivations is the assumption of an ellipsoidal coordinate system, which, combined with constant and power-law density profiles allows to use separation of variables, and therefore transform the numerically complicated 2-D PDE into an ODE.

In chapter 3 we present the spectral and pseudo-spectral methods that will be used to

solve PDEs numerically, and also show how they are related. After using an ellipsoidal coordinate system and expanding the unknown solution in terms of Chebyshev polynomials, we re-calculate numerically the inertial modes obtained by Wu (2005a). We conclude that, using the pseudo-spectral method simplifies the calculations, and saves great amount of computing time.

Next, in chapter 4, we explore the possibility that inertial modes inside Saturn may be detected indirectly using its rings as a seismograph. We follow Marley and Porco (1993) idea of detecting f-modes in the same way. The key element is that any normal mode inside Saturn produces torques harmonically at different locations on the rings. Inertial modes perturb the external gravitational potential, and can resonantly excite density and bending waves that can and have been observed by satellite missions to the outer planet. These type of waves on Saturn rings are associated to Lindblad and vertical resonances of the particles respectively. As mentioned in the introduction, inertial modes have not been detected outside the Earth, and since their eigenfunctions depend on the density gradient of the planet, they can be use to prove Saturn’s interior.

In chapter 5 we go back to our original task of calculating Q for general density profiles inside fully convective rotating planets. We start by using the pseudo-spectral method to calculate the inertial modes when a power-law density profile is used. We obtain the same results as Wu (2005a) did, and also, the same results as the spectral method produced after a time-consuming analytic calculation. After this “test” phase produced encouraging results, we proceed to calculate inertial modes in general density profiles. We use polytropes and find that, as Wu (2005a) estimated, the eigenfunction of a polytrope of similar index as a power-law, does not variates considerable, and therefore, produces similar tidal overlap integrals, and hence similar tidal quality factors Q . At least for smooth-density profiles the combination of the ellipsoidal coordinate system, and the expansion of the eigenfunction in terms of Chebyshev polynomials, produced highly accurate eigenfunctions, whose spectral coefficients converge very fast.

Things get blurry when the density profile have discontinuities or jumps, for example when a hard inner core may exist or when a phase transition, like the one that separates molecular hydrogen from metallic hydrogen. In chapter 6 we attempt to calculate eigenfunctions when a jump in density of either 1st or 2nd order occurs inside Jupiter at about 80 % of its radius. As Wu (2005b) estimated, it is expected that, when a density jump is present, the inertial mode couples more efficiently to the tidal potential, making possible to reduce Q three to four order of magnitudes from results of smooth density models. Our preliminary results showed lack of convergence, when we adopted densities from internal structure tables from Guillot (1999). Since it was not clear if the lack of convergence was due to a physical non-standing wave-like response of the mode to the jump, or to lack of spectral resolution, or numerical problems raised from the inaccuracies of the density tables, we used a toy model in which an analytical density profile included a parametrized hyperbolic tangent function that can be used to study the effect of the with and height of the jump in the actual convergence of the spectral coefficients. Even in that case the results were not that clear. We turned to a 1-d toy model, in which we explored how sound waves are sensitive to discontinuities of the same kind, using the same techniques we used in the 2-d inertial mode problem. Then we realized that it was spectral resolution the main problem, implying that, the full width at half maximum (FWHM) of the jump was inversely proportional to the truncation of the Chebyshev series used.

Finally in chapter 7 we address a criticism of Goodman and Lackner (2009) respect to the calculations made by Wu (2005a) in which the anelastic approximation was used. This approximation discards the terms in the inertial mode equation, proportional to the sound speed, since it gives rise to pressure waves, higher than inertial modes in terms of frequency, and also unimportant for resonant excitation due tidal potentials that variates from 5 hours to days. Goodman and Lackner (2009) points out that by discarding the sound speed term, the tidal overlap integral has been overestimated, and

that its introduction would produce perfect cancellation. They also mentioned that the long-wavelength nature of the tidal perturbation can only produce long-wavelength responses from the rotating the fluid. We produce numerical results that confirms the validity of the approximation, and explain why short-wavelength responses are possible.

Chapter 2

Equation of Motion that Govern Inertial Modes

We study inertial modes in a neutrally buoyant, uniformly rotating sphere. Much of the notation and derivations are similar to those in (Wu 2005a), but we include them here for completeness.

2.1 Equation of Motion in Vector form

Let the angular velocity Ω point in the z direction. When we introduce tidal perturbations later in this thesis, they will be assumed to be symmetric with respect to the z -axis.

We define the following variables for the background: pressure p , density ρ and gravitational potential Φ_0 . The adiabatic index $\Gamma_1 = \partial \ln p / \partial \ln \rho|_s$ (s being entropy) is related to the speed of sound by $\Gamma_1 = c_s^2 \rho / p$.

We also define the following perturbation quantities: the displacement vector $\boldsymbol{\xi}$, Eulerian perturbations to pressure, density and gravitational potential, p' , ρ' and Φ' respectively, and then Lagrangian counterparts, δp , $\delta \rho$, $\delta \Phi$.

Euler's equation for inviscid fluid motion reads,

$$\frac{d\mathbf{u}}{dt} = -\frac{\nabla P}{\rho} - \nabla\Phi, \quad (2.1.1)$$

where $d\mathbf{u}/dt = \frac{\partial\mathbf{u}}{\partial t} + \mathbf{u} \cdot \nabla\mathbf{u}$ is the time derivative in the inertial frame. To rewrite the left-hand-side in the rotating frame, we recognize that velocities in the two frames are related by

$$\mathbf{u} = \mathbf{v} + \boldsymbol{\Omega} \times \mathbf{r}, \quad (2.1.2)$$

The velocity in the rotating frame is related to the displacement $\boldsymbol{\xi}$ by $\mathbf{v} = \partial\boldsymbol{\xi}/\partial t = \dot{\boldsymbol{\xi}}$. Furthermore, any vector in the rotating frame is advected by rotation so that

$$\frac{d}{dt}_{\text{rotate}} = \frac{d}{dt}_{\text{inertial}} + \boldsymbol{\Omega} \times . \quad (2.1.3)$$

Combining these equations we obtain the equation of motion in the rotating frame

$$\frac{d\mathbf{v}}{dt} + 2\boldsymbol{\Omega} \times \mathbf{v} - \boldsymbol{\Omega} \times (\boldsymbol{\Omega} \times \mathbf{r}) = -\frac{\nabla P}{\rho} - \nabla\Phi. \quad (2.1.4)$$

This form contains two inertial forces: the second term in the left hand side is the Coriolis force, while the third term is the centrifugal force.

The centrifugal force contributes to the hydrostatic equilibrium of giant planets. However, we consistently ignore it in our treatment, both for the sake of simplicity and because we believe it causes a negligible perturbation. Jupiter has a break-up spin period (upper limit) of

$$\Omega_{\text{breakup}} = \sqrt{\frac{GM_J}{R_J^3}} = 2.8\text{hrs}, \quad (2.1.5)$$

so with a spin period of 9.8 hours, effect of the centrifugal force is $\sim (\Omega/\Omega_{\text{breakup}})^2 \sim 8\%$. For extra-solar giant planets, it is reasonable to assume that they have been tidally synchronized by their host stars and are spinning with a period of ~ 3 days. As a result, the magnitude of effect of the centrifugal force is $\sim 10^{-3}$. Similarly, we also ignore perturbations to the centrifugal force due to displacement.

In addition to the Euler equation, we also have the equation of mass conservation and Poisson's equation:

$$\frac{\partial \rho}{\partial t} + \nabla \cdot (\rho \mathbf{v}) = 0, \quad (2.1.6)$$

$$\nabla^2 \Phi = 4\pi G \rho. \quad (2.1.7)$$

Since the planet is fully convective and therefore largely neutrally stratified, its background density and pressure profiles are related through

$$\frac{d\rho}{dr} = \frac{\rho}{\Gamma_1 p} \frac{dp}{dr}. \quad (2.1.8)$$

We linearly perturb the above equations to obtain the equations of motion that govern inertial modes,

$$\rho \ddot{\boldsymbol{\xi}} + 2\rho \boldsymbol{\Omega} \times \dot{\boldsymbol{\xi}} = -\nabla p' + \frac{\nabla p}{\rho} \rho' - \rho \nabla \Phi', \quad (2.1.9)$$

$$\rho' + \nabla \cdot (\rho \boldsymbol{\xi}) = 0, \quad (2.1.10)$$

$$\nabla^2 \Phi' = 4\pi G \rho'. \quad (2.1.11)$$

We proceed to simplify this set of equations. First, we adopt the Cowling approximation, $\Phi' = 0$. We also ignore any external potential forcing such as the tidal potential as we are interested first in free oscillations. Second, we adopt the assumption that the perturbation is adiabatic,

$$\frac{\delta p}{p} = \Gamma_1 \frac{\delta \rho}{\rho} \quad (2.1.12)$$

This is valid for regions inside in which the planet that has thermal diffusion time is much longer than the characteristics timescale for the perturbation (i.e., mode period).

Since Lagrangian and Eulerian perturbations are related as

$$\delta X = X' + \boldsymbol{\xi} \cdot \nabla X, \quad (2.1.13)$$

combining this with equations 2.1.12 and 2.1.8 one obtains

$$\frac{p'}{p} = \Gamma_1 \frac{\rho'}{\rho}. \quad (2.1.14)$$

This allows us to introduce a new scalar

$$\psi = \frac{1}{\omega^2} \left(\frac{p'}{\rho} + \Phi' \right) = \frac{1}{\omega^2} \left(c_s^2 \frac{\rho'}{\rho} + \Phi' \right) = \frac{c_s^2}{\omega^2} \frac{\rho'}{\rho}, \quad (2.1.15)$$

and simplify equation 2.1.9 into

$$\rho \ddot{\boldsymbol{\xi}} + 2\rho \boldsymbol{\Omega} \times \dot{\boldsymbol{\xi}} = -\nabla \left(\frac{p'}{\rho} \right) - \nabla \Phi' = -\nabla \omega^2 \psi. \quad (2.1.16)$$

Here, ω is the mode frequency in the rotating frame. Following Wu (2005a), we adopt for all variables the following dependence on time (t) and on the azimuthal angle (ϕ): $X \propto \exp[i(m\phi - \omega t)]$. Modes with denotation (m, ω) and $(-m, -\omega)$ are physically the same mode, so we restrict ourselves to $\omega \geq 0$, with $m > 0$ representing a prograde mode, and $m < 0$ a retrograde one. We define the following dimensionless variables

$$\mu = \frac{\omega}{2\Omega}, \quad q = \frac{1}{\mu}. \quad (2.1.17)$$

From the dispersion relation (e.g. Unno et al. 1989) one can show that $0 < \mu \leq 1$ for inertial modes.

Following Wu (2005b), we manipulate equation 2.1.16 to obtain the following relationship between $\boldsymbol{\xi}$ and ψ ,

$$\boldsymbol{\xi} = \frac{1}{1 - q^2} (1 - iq \mathbf{e}_z \times - q^2 \mathbf{e}_z \mathbf{e}_z \cdot) \nabla \psi. \quad (2.1.18)$$

In the meantime, equation (2.1.10) can be manipulated to yield

$$\nabla \cdot \boldsymbol{\xi} + \frac{\omega^2}{c_s^2} \psi = \frac{\mathbf{e}_r \cdot \boldsymbol{\xi}}{H} = \frac{g}{c_s^2} (\mathbf{e}_r \cdot \boldsymbol{\xi}). \quad (2.1.19)$$

Combining these above two equations yields a second-order partial differential equation for ψ

$$\nabla^2 \psi - q^2 \frac{\partial^2 \psi}{\partial z^2} = \frac{1}{H} \left(\frac{\partial \psi}{\partial r} - q^2 \cos \theta \frac{\partial \psi}{\partial z} - \frac{mq}{r} \psi \right) - (1 - q^2) \frac{\omega^2}{c_s^2} \psi. \quad (2.1.20)$$

Here, $H \equiv -dr/d \ln \rho$ is the density scale height and $H = c_s^2/g$ (eq. 2.1.8), with g being the local gravitational acceleration. θ is the zenith angle and $\cos \theta = z/r$ with z being the

height along the rotational axis. Let ϖ be the cylindrical radius. The partial derivatives here are to be understood as $\partial/\partial r = \partial/\partial r|_{\theta}$, $\partial/\partial \theta = \partial/\partial \theta|_r$, $\partial/\partial z = \partial/\partial z|_{\varpi}$, and $\partial/\partial \varpi = \partial/\partial \varpi|_z$.

The last term in equation (2.1.20) is the compressional term. It represents the main restoring force for pressure waves. In comparison to the Coriolis force term, it is negligible for inertial waves as these waves are much lower in frequency than pressure waves. We retain this term in most of the numerical analysis (as it does not cause extra complications) but show in §7 that it does not indeed matter much for the results.

2.2 Equation of Motion in Ellipsoidal Coordinates

In general, the above partial differential equation is not separable in any coordinates and only fully numerical solutions could be sought. However, Bryan (1889) showed that, for the case of a constant density sphere ($H = \infty$, $c_s^2 = \infty$, so that the right-hand side of eq. 2.1.20 vanishes), the left-hand side of equation (2.1.20) is separable.

His procedure involves adopting the ellipsoidal coordinates (x_1, x_2, ϕ) , a hybrid between cylindrical and spherical coordinates, which are related to the Cartesian coordinates as

$$\begin{aligned} x &= \left[\frac{(1 - x_1^2)(1 - x_2^2)}{1 - \mu^2} \right]^{\frac{1}{2}} \cos \phi, \\ y &= \left[\frac{(1 - x_1^2)(1 - x_2^2)}{1 - \mu^2} \right]^{\frac{1}{2}} \sin \phi, \\ z &= \frac{x_1 x_2}{\mu}, \end{aligned} \tag{2.2.1}$$

with $x_1 \in [\mu, 1]$, $x_2 \in [-\mu, \mu]$, and ϕ is the usual azimuthal angle with $\phi \in [0, 2\pi]$. From now on, we normalize all lengths by the planetary radius R unless otherwise noted. The

cylindrical and spherical radii are given by, respectively,

$$\begin{aligned}\varpi^2 &= x^2 + y^2 = \frac{(1-x_1^2)(1-x_2^2)}{(1-\mu^2)}, \\ r^2 &= x^2 + y^2 + z^2 = 1 - \frac{(x_1^2 - \mu^2)(\mu^2 - x_2^2)}{(1-\mu^2)\mu^2}.\end{aligned}\quad (2.2.2)$$

Partial differentiation with respect to ϖ , z and r can be expressed in the new coordinates as,

$$\left. \frac{\partial}{\partial \varpi} \right|_z = \left. \frac{\partial x_1}{\partial \varpi} \right|_z \left. \frac{\partial}{\partial x_1} \right|_{x_2} + \left. \frac{\partial x_2}{\partial \varpi} \right|_z \left. \frac{\partial}{\partial x_2} \right|_{x_1} = -\frac{(1-\mu^2)\varpi}{x_1^2 - x_2^2} \left(x_1 \frac{\partial}{\partial x_1} - x_2 \frac{\partial}{\partial x_2} \right) \quad (2.2.3)$$

$$\left. \frac{\partial}{\partial z} \right|_{\varpi} = \left. \frac{\partial x_1}{\partial z} \right|_{\varpi} \left. \frac{\partial}{\partial x_1} \right|_{x_2} + \left. \frac{\partial x_2}{\partial z} \right|_{\varpi} \left. \frac{\partial}{\partial x_2} \right|_{x_1} = \frac{\mu}{x_1^2 - x_2^2} \left[x_2(x_1^2 - 1) \frac{\partial}{\partial x_1} - x_1(x_2^2 - 1) \frac{\partial}{\partial x_2} \right], \quad (2.2.4)$$

$$\left. \frac{\partial}{\partial r} \right|_{\theta} = \left. \frac{\partial r}{\partial z} \right|_{\theta} \left. \frac{\partial}{\partial z} \right|_{\varpi} + \left. \frac{\partial r}{\partial \varpi} \right|_{\theta} \left. \frac{\partial}{\partial \varpi} \right|_z = -\frac{(1-x_1^2)x_1}{(x_1^2 - x_2^2)r} \frac{\partial}{\partial x_1} + \frac{(1-x_2^2)x_2}{(x_1^2 - x_2^2)r} \frac{\partial}{\partial x_2}. \quad (2.2.5)$$

Fig. 2.1 shows graphically how the ellipsoidal coordinates and the spherical coordinates are related to each other.

In this set of coordinates, the partial differential equation (eq. (2.1.20)) is turned into two ordinary differential equations, or

$$\begin{aligned}\left(\nabla^2 - q^2 \frac{\partial^2}{\partial z^2} \right) \psi &= \frac{1-\mu^2}{x_1^2 - x_2^2} \left\{ \left[(1-x_1^2) \frac{\partial^2}{\partial x_1^2} - 2x_1 \frac{\partial}{\partial x_1} - \frac{m^2}{1-x_1^2} \right] \right. \\ &\left. - \left[(1-x_2^2) \frac{\partial^2}{\partial x_2^2} - 2x_2 \frac{\partial}{\partial x_2} - \frac{m^2}{1-x_2^2} \right] \right\} \psi = 0.\end{aligned}\quad (2.2.6)$$

The corresponding solution is

$$\psi = \psi_1(x_1)\psi_2(x_2), \quad (2.2.7)$$

with ψ_i being the Legendre polynomial.

Realistic planets do not have uniform density profiles. In this respect, an interesting advance is reported in Wu (2005b) where it is shown that even for a density profile of the following power-law form

$$\rho \propto (1-r^2)^\beta, \quad (2.2.8)$$

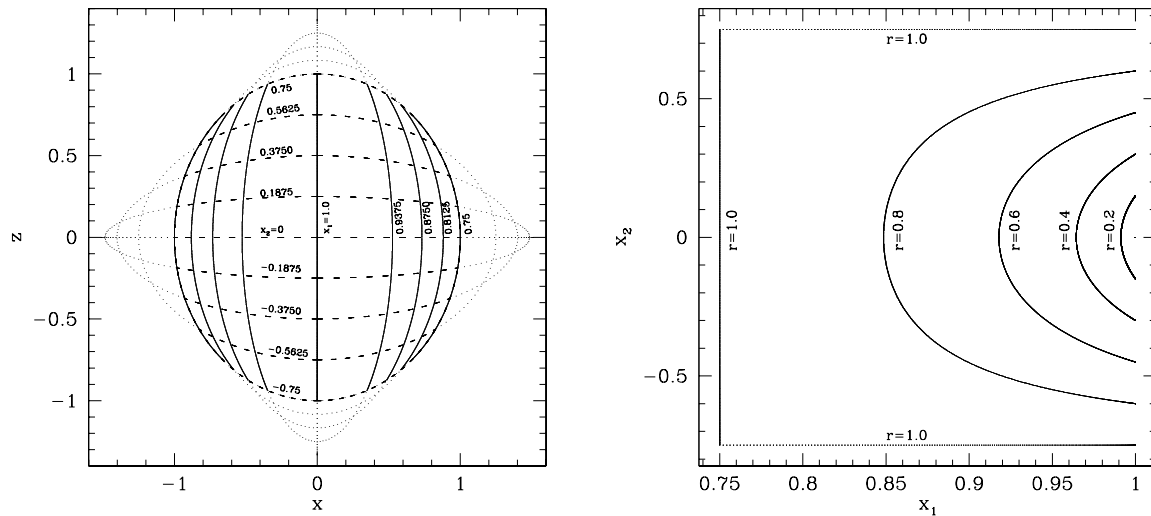


Figure 2.1 This figure is adopted from Wu (2005a) and shows how the ellipsoidal coordinates are mapped onto a meridional plane (left panel), as well as how a meridional plane is mapped onto the ellipsoidal coordinates (right panel) when $\mu = 0.75$. The ellipsoidal coordinates are a hybrid between cylindrical and spherical coordinates and are naturally suited for studying motion affected by the Coriolis force. On the spherical surface ($r = 1$), either x_1 or $|x_2|$ (or both) equals μ . This makes it particularly simple to write down boundary conditions at the surface. The region near the surface where $\cos \theta \sim \pm\mu$ (and $x_1 \sim \mu$, $x_2 \sim \pm\mu$) experiences a more densely packed equidistant x_1, x_2 curves. We call this region the ‘singularity belt’. Inertial modes acquire the largest amplitudes and the largest gradients in this region. Adoption of ellipsoidal coordinates naturally affords us the resolution to study this region in more detail.

where β is any dimensionless real number, if one could ignore the compressional term, equation (2.1.20) is still separable in the ellipsoidal coordinates. The resulting equation is

$$(\mathcal{E}_1 - \mathcal{E}_2)\psi = 0, \quad (2.2.9)$$

where the differential operator \mathcal{E}_i is defined as

$$\mathcal{E}_i = \left[\mathcal{D}_i + \frac{2\beta x_i(1 - x_i^2)}{x_i^2 - \mu^2} \frac{\partial}{\partial x_i} + \frac{2\mu\beta m}{x_i^2 - \mu^2} \right], \quad (2.2.10)$$

which contains also a differential operator \mathcal{D}_i where

$$\mathcal{D}_i = \frac{\partial}{\partial x_i} \left[(1 - x_i^2) \frac{\partial}{\partial x_i} \right] - \frac{m^2}{1 - x_i^2}. \quad (2.2.11)$$

This latter operator appears in the equation of motion in the case when density is uniform, $(\mathcal{D}_1 - \mathcal{D}_2)\psi = 0$ (Bryan 1889).

The solution to equation (2.2.9) is

$$\psi = \psi_1(x_1)\psi_2(x_2), \quad (2.2.12)$$

with ψ_i being a polynomial in x_i . The power-law density profile is much closer to that in realistic planets. Solutions thus obtained provide useful insights into the real case.

For arbitrary density laws, equation (2.1.20) can be organized into the following useful form (Wu 2005a),

$$\begin{aligned} & (\mathcal{E}_1 - \mathcal{E}_2)\psi - 2 \frac{d \ln X}{d \ln t} \left[\frac{(1 - x_1^2)x_1}{(x_1^2 - \mu^2)} \frac{\partial}{\partial x_1} \right. \\ & \left. + \frac{(1 - x_2^2)x_2}{(\mu^2 - x_2^2)} \frac{\partial}{\partial x_2} + \frac{m\mu(x_1^2 - x_2^2)}{t} \right] \psi - \frac{4\Omega^2 R^2}{c_s^2} (x_1^2 - x_2^2)\psi = 0. \end{aligned} \quad (2.2.13)$$

Where, $X = \rho_{\text{surf}}/\rho$, ρ_{surf} is the power-law density profile, ρ is the density profile of the planet, and $t = (x_1^2 - \mu^2)(\mu^2 - x_2^2) = \mu^2(1 - \mu^2)(1 - r^2)$. In this equation, the second term (with coefficient $d \ln X/d \ln t$) takes care of density departure from the power-law form, and the compressional term is of order $(\Omega/\Omega_{\text{breakup}})^2 \ll 1$ except very near the surface. These two terms couple the dependency in the x_1 direction with that in the x_2 direction. They are the origin of algebraic difficulties.

For a density profile that deviates slightly from a power law (as that inside Jupiter), Wu (2005a) found that equation (2.2.13) can be manipulated into a new form that minimizes the role of the non-separable part. For instance, introducing a fiducial density $\rho_{surf} = (1 - r^2)^\beta$, with the power-law index taken that to be that for the true density ρ near the surface, and defining

$$X = \frac{\rho_{surf}}{\rho}, \quad (2.2.14)$$

as well as a new variable ψ_0 where

$$\psi = \sqrt{\frac{\rho_{surf}}{\rho}} \psi_0, \quad (2.2.15)$$

we can recast equation (2.1.20) into one for the variable ψ_0 ,

$$(\mathcal{E}_1 - \mathcal{E}_2)\psi_0 + (d_1 - d_2)\psi_0 = 0, \quad (2.2.16)$$

where the terms with the operator \mathcal{E}_i represent the separable part, and the terms containing d_i represent the non-separable part,

$$d_i = \frac{1}{\sqrt{X}} \left\{ \frac{\partial}{\partial x_i} \left[(1 - x_i^2) \frac{\partial \sqrt{X}}{\partial x_i} \right] + \left(2\beta - 2 \frac{d \ln X}{d \ln t} \right) \times \right. \\ \left. \frac{x_i(1 - x_i^2)}{x_i^2 - \mu^2} \frac{\partial \sqrt{X}}{\partial x_i} - \frac{2m\mu}{x_i^2 - \mu^2} \frac{d \ln X}{d \ln t} \right\}. \quad (2.2.17)$$

Here, the dimensionless variable $t = (x_1^2 - \mu^2)(\mu^2 - x_2^2) = \mu^2(1 - \mu^2)(1 - r^2)$. For density profiles that vary slowly compared with wavelengths of inertial modes, the non-separable part is much smaller and is roughly $\mathcal{O}(kH)^{-2} \ll 1$ when compared to the separable part. Here k is the wavevector.

Wu (2005b) ignored the non-separable part and went ahead and used the resulting inertial-mode eigenfunctions to obtain estimates for the tidal Q value. She found that for Jupiter, the rate of tidal dissipation due to these inertial modes well exceeds that due to equilibrium tide ($Q \sim 10^{13}$) but still falls a couple order of magnitudes below the observed value of $Q \sim 4 \times 10^4$ (Lainey et al. 2009).

Realistic planets have density profiles that resemble a power-law near the surface, and depart gently from the power-law in the interior. So X is constant in the outer layer (where scale-height is small) and a gently varying function in the deep interior (where scale-height is of order r), $d \ln X / d \ln t \sim R/H \sim 1$. In comparison, the \mathcal{E}_i operator gives rise to a term of order $\mathcal{O}(kR)^2 \gg 1$. This is the reason that in obtaining equation (2.2.13), we scale the density by a power-law one that is akin to the surface density profile. This minimizes the effect of density variations on the inertial-mode eigenfunctions. As a result, it minimizes the cross-talk between spectral terms of different spatial degrees (see later).

Since inertial-modes have WKB envelopes that scale as $\psi \propto 1/\sqrt{\rho}$, it may be useful to further remove this envelope from the differential equation (Wu 2005a) by defining a new variable $\psi_0 = \psi/(1/\sqrt{\rho})$. However, in our spectral and pseudo-spectral codes, this introduces derivatives of density profile which have numerical (formal) singularities both near the centre and near the surface. These could be removed with further algebra but we simply adopt equation (2.2.13) as our starting point.

Even though the equation of motion is not separable in the ellipsoidal coordinates, we choose this coordinate set over the usual spherical coordinates. This choice afforded us great advantages.

Inertial-modes are highly spatially inhomogeneous. In the case of a power-law density profile, we know that a given inertial-mode can be labeled by three quantum numbers, n_1, n_2 and m . Here, n_1 and n_2 are the number of nodal lines in the x_1 and x_2 directions, respectively. In the (x_1, x_2) coordinates, the nodal lines are roughly evenly spaced. However, in the spherical coordinates, the nodal lines are not – they concentrate toward the surface and especially near the critical latitude $|\cos \theta| \sim \mu$.

When the density deviates slightly from the power-law case, we still expect the above description to apply. So when solving for inertial-modes in the ellipsoidal coordinates, we spread out the surface fine ripples into more uniform ripples. When a spectral method is

used, this approach has the advantage that we need fewer spectral terms. So our solution can be more accurate and can be obtained at a lower cost.

Lastly, adopting the ellipsoidal coordinates makes mode typing trivial. We find that even for arbitrary density profiles, mode nodal lines are still largely parallel to constant x_1 or x_2 lines, and it is possible to associate a set of quantum numbers to each mode. This is not possible when using, e.g., spherical coordinates.

We outline the detailed numerical approach in the next chapter.

2.3 Boundary Conditions

Inertial-modes are standing waves inside the cavity of a planet. While in the ϕ direction, they are running waves with $\exp(im\phi - i\omega t)$ dependence, in the meridional plane, they are reflected from the center, the surface, the pole and the equator.

In the ellipsoidal coordinates, the center is situated at $x_1 = 1, x_2 = 0$; the surface is $x_1 = \mu$ and/or $|x_2| = \mu$. The rotation axis has $x_1 = 1$, and equator $x_2 = 0$. The center boundary condition is also exemplified in the one for the polar axis.

2.3.1 Surface

At the planetary surface ($r = 1$), the Lagrangian pressure perturbation has to approach zero. In fact, δp has to approach zero faster than ρ does (Unno et al. 1989). One can simply show this by the following expression for pressure near the surface

$$\begin{aligned} \delta p &= \int_{z+\xi_z}^{\infty} (g + \delta g)(\rho + \delta \rho) dz - \int_z^{\infty} g \rho dz \\ &\approx \frac{\delta g}{g} p + \frac{\delta \rho}{\rho} p + \frac{\xi_z}{z} p. \end{aligned} \quad (2.3.1)$$

Here z is depth and increases downward from the surface. As a result

$$\frac{\delta p}{\rho} \approx \frac{\delta g}{g} \frac{p}{\rho} + \frac{\delta \rho}{\rho} \frac{p}{\rho} + \frac{\xi_z}{z} \frac{p}{\rho} \propto \left(\delta g + \frac{\delta \rho}{\rho} g + \frac{\xi_z}{z} \frac{p}{\rho} \right) z \rightarrow 0, \quad (2.3.2)$$

if all perturbations behave regularly (do not diverge) near the surface.

The equation of mass conservation (eq. 2.1.10), the adiabatic assumption (eq. 2.1.12) and eq. (2.1.19) are used to relate ξ_r to $\delta p/\rho$,

$$\frac{\delta p}{\rho} = \Gamma_1 \frac{\delta \rho p}{\rho \rho} = -\Gamma_1 (\nabla \cdot \boldsymbol{\xi}) \frac{p}{\rho} = \omega^2 \psi - g \xi_r, \quad (2.3.3)$$

where the first term rises from compression and is sub-dominant. In the end, the condition that $\delta p/\rho = 0$ at the surface is equivalent to

$$\xi_r|_{r=R} = \frac{\omega^2}{g} \psi|_{r=R}, \quad (2.3.4)$$

or a dimensionless form where all lengths are scaled by radius R ,

$$\xi_r|_{r=1} = \frac{\omega^2}{g/R} \psi|_{r=R} = 4\mu^2 \left(\frac{\Omega}{\Omega_{\text{breakup}}} \right)^2 \psi|_{r=R}. \quad (2.3.5)$$

In Wu (2005a), a condition that $\xi_r = 0$ at the surface is adopted. Questions arise (Goodman and Lackner 2009) whether her simplified boundary condition may account for the magnitudes of tidal coupling she obtained. This is addressed in §7.

The radial displacement is related to ψ as¹

$$\xi_r = \frac{(1-x_1^2)(1-x_2^2)}{(1-\mu^2)(x_1^2-x_2^2)r} \times \left[x_1 \frac{\partial \psi}{\partial x_1} \frac{\mu^2-x_2^2}{1-x_2^2} - x_2 \frac{\partial \psi}{\partial x_2} \frac{\mu^2-x_1^2}{1-x_1^2} + m\mu \frac{x_1^2-x_2^2}{(1-x_1^2)(1-x_2^2)} \psi \right], \quad (2.3.6)$$

when the condition $\xi_r = 0$ is adopted, we have the following condition for ψ at the surface,

$$\begin{aligned} \left. \frac{\partial \psi}{\partial x_1} \right|_{x_1=\mu} &= -\frac{m}{1-\mu^2} \psi|_{x_1=\mu}, \\ \left. \frac{\partial \psi}{\partial x_2} \right|_{|x_2|=\mu} &= -\text{SIGN}[x_2] \frac{m}{1-\mu^2} \psi|_{|x_2|=\mu}. \end{aligned} \quad (2.3.7)$$

¹Note that the original equation (28) in Wu (2005a) is **incorrect**. The correct form is reproduced here.

2.3.2 Equator

At the equator ($x_2 = 0$), even-parity modes ² satisfy

$$\left. \frac{\partial \psi}{\partial x_2} \right|_{x_2=0} = 0, \quad (2.3.8)$$

while odd-parity modes satisfy

$$\psi|_{x_2=0} = 0. \quad (2.3.9)$$

2.3.3 Polar Axis

The boundary condition at the polar axis ($x_1 = 1$) and the center ($x_1 = 1, x_2 = 0$) are obtained by studying the asymptotic behaviour of the equation of motion near each axis. In order to implement these two boundary conditions, it is more accurate to solve equation (2.2.13) for $\psi(x_1, x_2) = (1 - x_1^2)^{|m|/2}(1 - x_2^2)^{|m|/2}g(x_1, x_2)$, and therefore we get:

$$\begin{aligned} & (\mathcal{F}_1 - \mathcal{F}_2)g - 2 \frac{d \ln X}{d \ln t} \left[\frac{(1 - x_1^2)x_1}{(x_1^2 - \mu^2)} \frac{\partial}{\partial x_1} \right. \\ & \left. + \frac{(1 - x_2^2)x_2}{(\mu^2 - x_2^2)} \frac{\partial}{\partial x_2} + \frac{m\mu(x_1^2 - x_2^2)}{t} \right] g - \frac{4\Omega^2 R^2}{c_s^2} (x_1^2 - x_2^2)g = 0, \end{aligned} \quad (2.3.10)$$

where the differential operator \mathcal{F}_i is defined as

$$\mathcal{F}_i = (1 - x_i^2) \frac{\partial^2}{\partial x_i^2} - 2x_i(|m| + 1) \frac{\partial}{\partial x_i} + \frac{2\beta x_i(1 - x_i^2)}{x_i^2 - \mu^2} \frac{\partial}{\partial x_i} + \left[-\frac{2\beta|m|x_i^2}{x_i^2 - \mu^2} + \frac{2\beta m\mu}{x_i^2 - \mu^2} \right]. \quad (2.3.11)$$

In reality, we often do not implement this boundary condition explicitly. Instead, the polynomial expansion we adopted (Chebyshev polynomial of the first kind) naturally excludes the presence of singularities at the polar axis.

²It is straightforward to show that the displacement vector ξ has the same equatorial symmetry as ψ .

Chapter 3

Spectral and Pseudo-spectral Methods

In this chapter, we describe in detail the mathematical approach we adopt in solving equation (2.2.13).

3.1 Rational

We describe briefly the rationale behind our adoption of the pseudo-spectral method.

3.1.1 Which Solver for the Partial Differential Equation?

There are three common methods to find the numerical solutions of partial differential equations: the finite element method, the finite difference method and the spectral method.

Early on in the project, we have decided against methods from the first class. The finite element method consists of chopping the planet (actually the meridional plane) into little triangles and using a low-order polynomials to approximate the eigenfunction in each corner of these triangles. The coefficients of the polynomials are then solved

for in a very sparse matrix which encodes the equations of motion and the boundary conditions. Compared to the spectral method, this method is more suitable for problems in complex domains (like crashing cars) and has in general lower accuracy for the same computation time.

In the finite difference method, derivatives of a function are replaced by its Taylor expansion to a certain degree. Only points lying sufficiently close by can be causally connected.

In contrast, in the spectral method one expands the unknown function into a series of basis functions. This is a *global* expansion. The derivatives of the function are evaluated analytically using the basis functions. They are accurate to N th degree where N is the order of series expansion. As a result, the spectral method is more accurate for a much smaller computational cost.

3.1.2 Which Basis Function?

While eigenfunctions for power-law density profile can be exactly solved for, those for different density profiles are more difficult. In equation (2.2.17), it is possible to see that the latter eigenfunction should deviate from the power-law set (properly scaled) by $\mathcal{O}(kR)^{-2} \ll 1$. The deviations can be considered as perturbations. So we investigated initially whether one can use a sum of un-perturbed (power-law) eigenfunctions to approximate the actual eigenfunctions, i.e.,

$$\psi(x_1, x_2) = \sum_{n_1, n_2} \alpha_{n_1, n_2} \psi_{n_1}(x_1) \psi_{n_2}(x_2), \quad (3.1.1)$$

where $\psi_{n_i}(x_i)$ is the solution to the ordinary differential equation obtained from equation (2.2.9). This idea does not work. Firstly, each $\psi_{n_i}(x_i)$ solution has a different frequency which also determines the shape of the coordinate basis. The new mode may well also have a different eigenfrequency. The choice of our coordinate basis preempts this expansion from being meaningful. Secondly, the operator in equation (2.2.13) is not Hermitian,

meaning that its eigenfunctions do not form a complete basis set. So even if all eigenfunctions have the same frequency, we can not use this expansion to adequately represent any new function.

In usual calculations of stellar oscillations, when non-separability is encountered, it is most common to expand the eigenfunction in the angular direction using the spherical harmonics function (Unno et al. 1989), and in the radial direction using, e.g., the Chebyshev polynomials. However, for inertial modes, it is highly advantageous to remain in the ellipsoidal coordinates (as described in §2.2). Therefore we consider a different type of expansion, namely, expand in both (x_1, x_2) directions using the Chebyshev polynomials.

Our experience in the power-law case shows that it is better to deal with the following $g(x_1, x_2)$ function,

$$\psi(x_1, x_2) = (1 - x_1^2)^{|m|/2}(1 - x_2^2)^{|m|/2}g(x_1, x_2), \quad (3.1.2)$$

than with $\psi(x_1, x_2)$ directly. This removes the apparently divergent term $m^2/(1 - x_i^2)$ from the differential operator in equation (2.2.11). Compared to ψ , g is more smoothly varying near the polar axis ($x_1 \rightarrow 1$). Numerically, anything that varies quickly is harder to resolve and requires a greater computational power.

We then expand this function in the basis of Chebyshev polynomials. In this procedure, since the Chebyshev polynomials are orthogonal in the range $(-1, 1)$, while our (x_1, x_2) coordinates do not occupy the same range, we have to perform the following transformation of variables,

$$\begin{aligned} x_1 &= \frac{(1 + \mu) + (1 - \mu)t_1}{2}, & t_1 &\in [-1, 1], \\ x_2 &= \mu t_2, & t_2 &\in [-1, 1]. \end{aligned} \quad (3.1.3)$$

And the actual expansion is (instead of eq. 3.1.1),

$$g(x_1, x_2) = g(t_1, t_2) = \sum_{N,M} \alpha_{NM} T_N(t_1) T_M(t_2). \quad (3.1.4)$$

where T_i is the Chebyshev polynomials of the first kind (Abramowitz and Stegun 1972).

Why do we choose Chebyshev polynomials? As discussed in Boyd (2001), all basis functions used in spectral methods are one or the other variants of the Fourier series. In our case, our boundary conditions are non-periodic, and our domain of operation is finite. This argues for either Chebyshev or Legendre polynomials. In order to reach rapid convergence with ease of computation, we choose the Chebyshev polynomials, whose spectral coefficients tend to converge exponentially in those PDE where an unknown smooth eigenfunction is expected, much faster than any other eigenfunction expansion based in other known orthogonal functions (Boyd 2001). Boyd (2001) set in stone the following amusing “moral principle”:

- “*When in doubt, use Chebyshev polynomials unless the solution is spatially periodic, in which case an ordinary Fourier series is better.*”
- “*Unless you’re sure another set of basis functions is better, use Chebyshev polynomials.*”
- “*Unless you’re really, really sure that another set of basis functions is better, use Chebyshev polynomials.*”

One trick in applying the spectral method is to choose the correct set of basis functions that automatically satisfy part (or all) of the boundary conditions. If all conditions are satisfied, the algebraic equations only come from minimizing the residuals of the differential equation and the computational cost is reduced.

Chebyshev of the first kind and the second kind satisfy (Boyd 2001; Abramowitz and Stegun 1972) , respectively,

$$T_n(\cos \theta) = \cos(n\theta), \quad U_n(\cos \theta) = \frac{\sin((n+1)\theta)}{\sin \theta}. \quad (3.1.5)$$

Our boundary condition at the polar axis (§2.3.3, $x_1 \rightarrow 1$, $t_1 \rightarrow 1$) is that the eigenfunction is regular. This may be achieved by taking either T_n or U_n . Usually T_n is

chosen. Alternatively speaking, choosing T_n already automatically guarantees that our boundary condition at the polar axis can be satisfied.

In addition, modes that are symmetric with respect to the equator (even parity in x_2 or t_2) can only contain Chebyshev polynomials $T_n(t_2)$ of even order; and ones that are anti-symmetric can only contain $T_n(t_2)$ of odd orders.

Following the expansion in equation (3.1.4), there are two approaches to solve for α_{NM} . One is called the spectral method, which we describe below. And the second method, the pseudo-spectral method, is described in §3.4.

3.2 Preparatory Derivations

The equation of motion is (see §2.2):

$$(\mathcal{E}_1 - \mathcal{E}_2)\psi + C = 0, \quad (3.2.1)$$

and the differential operators are

$$\mathcal{E}_i = \left[\mathcal{D}_i + \frac{2\beta x_i(1-x_i^2)}{x_i^2 - \mu^2} \frac{\partial}{\partial x_i} + \frac{2\mu\beta m}{x_i^2 - \mu^2} \right], \quad (3.2.2)$$

$$\mathcal{D}_i = \frac{\partial}{\partial x_i} \left[(1-x_i^2) \frac{\partial}{\partial x_i} \right] - \frac{m^2}{1-x_i^2}. \quad (3.2.3)$$

The symbol C in equation (3.2.1) is exactly zero for the separable case, or represents the non-separable piece in equation 2.2.13 when it is present. Even if it is zero, we keep it to illuminate the operations we perform on this equation.

Converting from ψ to g removes the algebraic singularity at $x_i = 1$ and transforms the differential equation to

$$(\mathcal{F}_1 - \mathcal{F}_2)g + \frac{C}{(1-x_1^2)^{|m|/2}(1-x_2^2)^{|m|/2}} = 0 \quad (3.2.4)$$

where

$$\begin{aligned} \mathcal{F}_i = & (1-x_i^2) \frac{\partial^2}{\partial x_i^2} - 2x_i(|m|+1) \frac{\partial}{\partial x_i} + \frac{2\beta x_i(1-x_i^2)}{x_i^2 - \mu^2} \frac{\partial}{\partial x_i} \\ & + \left[-|m|(|m|+1) - \frac{2\beta|m|x_i^2}{x_i^2 - \mu^2} + \frac{2\beta m\mu}{x_i^2 - \mu^2} \right]. \end{aligned} \quad (3.2.5)$$

One can ignore the term that scales as $-|m|(|m| + 1)$ as both \mathcal{F}_i contain them and they cancel each other.

We multiply equation (3.2.4) by $(x_1^2 - \mu^2)(x_2^2 - \mu^2)$ to remove the denominator in equation 3.2.5, change variables from x_1, x_2 to t_1, t_2 and obtain

$$(\tilde{\mathcal{F}}_1 - \tilde{\mathcal{F}}_2)g + \frac{C(x_1^2 - \mu^2)(x_2^2 - \mu^2)}{(1 - x_1^2)^{|m|/2}(1 - x_2^2)^{|m|/2}} = 0, \quad (3.2.6)$$

where the operators are no longer symmetric,

$$\begin{aligned} \tilde{\mathcal{F}}_1 &= \frac{1}{4} [(1 + \mu)^2 - 4\mu^2 + 2(1 - \mu^2)t_1 + (1 - \mu)^2 t_1^2] \mu^2 (t_2^2 - 1) \times \\ &\quad \left\{ \frac{[4 - (1 + \mu)^2 - 2(1 - \mu^2)t_1 - (1 - \mu)^2 t_1^2]}{(1 - \mu)^2} \frac{\partial^2}{\partial t_1^2} \right. \\ &\quad \left. - 2 \frac{(|m| + 1)}{(1 - \mu)} [(1 + \mu) + (1 - \mu)t_1] \frac{\partial}{\partial t_1} \right\} \\ &\quad + 2\beta \mu^2 (t_2^2 - 1) \left\{ \frac{1}{4} \frac{[(1 + \mu) + (1 - \mu)t_1]}{(1 - \mu)} [4 - (1 + \mu)^2 \right. \\ &\quad \left. - 2(1 - \mu^2)t_1 - (1 - \mu)^2 t_1^2] \frac{\partial}{\partial t_1} \right. \\ &\quad \left. - \frac{|m|}{4} [(1 + \mu)^2 + 2(1 - \mu^2)t_1 + (1 - \mu)^2 t_1^2] + \mu m \right\} \quad (3.2.7) \end{aligned}$$

and

$$\begin{aligned} \tilde{\mathcal{F}}_2 &= \frac{1}{4} [(1 + \mu)^2 - 4\mu^2 + 2(1 - \mu^2)t_1 + (1 - \mu)^2 t_1^2] \times \\ &\quad \left\{ -(1 - \mu^2 t_2^2)(1 - t_2^2) \frac{\partial^2}{\partial t_2^2} + 2\mu^2 (|m| + 1) t_2 (1 - t_2^2) \frac{\partial}{\partial t_2} \right. \\ &\quad \left. + 2\beta \left[(1 - \mu^2 t_2^2) t_2 \frac{\partial}{\partial t_2} - |m| \mu^2 t_2^2 + \mu m \right] \right\}. \quad (3.2.8) \end{aligned}$$

It is straight-forward to convert the non-separable piece in equation (2.2.13) from (ψ, x_1, x_2) variables to (g, t_1, t_2) variables. We omit this operation here.

The boundary condition at the surface can also be written in (g, t_1, t_2) variables.¹

Equation (2.3.7) becomes,

$$\left. \frac{\partial g}{\partial t_1} \right|_{t_1=-1} = -\frac{(m - |m|\mu)\mu}{2(1 + \mu)} g|_{t_1=-1}, \quad (3.2.9)$$

$$\left. \frac{\partial g}{\partial t_2} \right|_{|t_2|=1} = -\text{SIGN}[t_2] \frac{(m - |m|\mu)\mu}{1 - \mu^2} g|_{|t_2|=1}. \quad (3.2.10)$$

¹Parity conditions at the equator and the polar axis are automatically satisfied when taking the appropriate set of Chebyshev polynomials for expansion.

3.3 Spectral Method

The spectral method (aka, the Galerkin's method, the non-interpolating method) relies on the orthogonality relation between Chebyshev polynomials of different degrees. It turns a partial (or ordinary, though seldom useful) differential equation into a series of linear algebraic equations.

We first describe this for a 1-D problem. Any arbitrary function $\psi(x)$ can be approximated by a polynomial expansion within a certain interval,

$$\psi(x) \approx \psi_N(x) = \sum_{n=0}^N \alpha_n \phi_n(x), \quad (3.3.1)$$

where $\phi_n(x)$ constructs a complete set of orthogonal functions. The spectral coefficients α_n are found by:

$$\alpha_n = \frac{\langle \phi_n, \psi \rangle}{\langle \phi_n, \phi_n \rangle} \quad (3.3.2)$$

with the inner product defined as

$$\langle \phi_n, \psi \rangle \equiv \int_a^b \psi(x) \phi_n(x) \rho(x) dx, \quad (3.3.3)$$

and $\rho(x)$ is the associated weighting function for ϕ_n .

Now consider an ordinary differential equation

$$\mathcal{H}\psi(x) = f(x), \quad (3.3.4)$$

where \mathcal{H} is a differential operator and $f(x)$ is the forcing function. Expand as in equation (3.3.1) for $\psi(x)$. The spectral method transforms equation (3.3.4) into the following set of linear algebra equations,

$$\mathbf{H} \cdot \boldsymbol{\alpha} = \mathbf{f}, \quad (3.3.5)$$

where $\boldsymbol{\alpha} = (\alpha_0, \alpha_1, \alpha_2, \dots, \alpha_N)$, and

$$\begin{aligned} H_{ij} &= \langle \phi_i, \mathcal{H}\phi_j \rangle & i, j &= 0, 1, 2, \dots, N \\ f_i &= \langle \phi_i, f \rangle & i &= 0, 1, 2, \dots, N. \end{aligned} \quad (3.3.6)$$

If the basis functions do not individually satisfy the boundary conditions, it is necessary to replace some of the rows of equation (3.3.5) by equations that express the boundary conditions. In general, \mathbf{H} is a band-diagonal matrix and spectral coefficients α_n of the neighbor degrees are coupled.

This technique can be trivially extended to expansion in N-dimensions.

3.3.1 The Non-separable Case

For our problem at hand, we adopt the following expansion² (eq. 3.1.4)

$$g(t_1, t_2) = \sum_{N=0}^{N_{max}} \sum_{M=0}^{M_{max}} \alpha_{NM} T_N(t_1) T_M(t_2). \quad (3.3.7)$$

We insert this into 3.2.6. Multiply both sides of that equation by

$\sqrt{1-t_1^2} U_{N'}(t_1) \sqrt{1-t_2^2} U_{M'}(t_2)$, and integrate over the range of $t_i \in [-1, 1]$.

The Chebyshev polynomials are orthogonal to each other,

$$\begin{aligned} \int_{-1}^1 \frac{T_i(x) T_j(x)}{\sqrt{1-x^2}} dx &= \frac{\pi}{2} \delta_{ij}, \\ \int_{-1}^1 \sqrt{1-x^2} U_i(x) U_j(x) dx &= \frac{\pi}{2} \delta_{ij}, \end{aligned} \quad (3.3.8)$$

where δ_{ij} is the Kronecker delta. An exception to the above expression occurs at $i = j = 0$ where the integral of $T_i T_j$ produces π . The one concerning U_i is the more useful one.

The integration over t_1, t_2 then allows one to transform equation (3.2.6) into a linear algebraic equations that relate α_{NM} to (potentially) every other $\alpha_{N'M'}$. The corresponding matrix has $(N_{max} + 1) \times (M_{max} + 1)$ rows and equal number of columns. It is sparse and largely band-diagonal. Inverting this matrix yields the coveted coefficients α_{NM} .

For completeness, we report here the linear algebra equation for $N' \geq 3$ and $M' \geq 3$ (the lower order elements satisfy slightly different equations from the general algorithm),

$$\alpha_{N'-2, M'-2} \left\{ \frac{1}{64} \langle [-(2|m| + 1)(N' - 2) - (N' - 2)^2] - [-(2|m| + 2)(M' - 2) \right.$$

²Our later discussions indicates that the expansion in t_2 can be reduced to expanding using only even (or only odd) T_M 's. But we disregard this simplification for the moment.

$$\begin{aligned}
& -(M' - 2)^2] \rangle + \frac{2\beta}{64} \langle [-((N' - 2) + |m|)] - [-((M' - 2) + |m|)] \rangle \Big\} \\
& + \alpha_{N'-2, M'} \left\{ \frac{1}{8} \left\langle [-(2|m| + 1)(N' - 2) - (N' - 2)^2] \left(\frac{1}{8} - \frac{\mu^2}{2} \right) \right. \right. \\
& \quad \left. \left. - \frac{1}{8} [-3(2|m| + 1)M' - M'^2] + 4\mu^2 [(2|m| + 1)M' + M'^2] \right\rangle \right. \\
& \quad \left. + \frac{2\beta}{8} \left\langle [-((N' - 2) + |m|)] \left(\frac{1}{8} - \frac{\mu^2}{2} \right) - \frac{1}{8} [(M' - |m|) + 4m\mu] \right\rangle \right\} \\
& + \alpha_{N'-2, M'+2} \left\{ -\frac{1}{8} \left\langle [-(2|m| + 1)(N' - 2) - (N' - 2)^2] \left(\frac{1}{8} - \frac{\mu^2}{2} \right) \right. \right. \\
& \quad \left. \left. + \frac{1}{8} [-3(2|m| + 1)(M' + 2) + (M' + 2)^2] + 4\mu^2 [(2|m| + 1)(M' + 2) \right. \right. \\
& \quad \left. \left. - (M' + 2)^2] \right\rangle - \frac{2\beta}{8} \left\langle [-((N' - 2) + |m|)] \left(\frac{1}{8} - \frac{\mu^2}{2} \right) \right. \right. \\
& \quad \left. \left. + \frac{1}{8} [(M' + 2) + |m|] - 4m\mu \right\rangle \right\} \\
& + \alpha_{N'-2, M'+4} \left\{ -\frac{1}{64} \left\langle [-(2|m| + 1)(N' - 2) - (N' - 2)^2] + [-(2|m| + 1)(M' + 4) \right. \right. \\
& \quad \left. \left. + (M' + 4)^2] \right\rangle - \frac{2\beta}{64} \left\langle [-((N' - 2) + |m|)] + [|m| - (M' + 4)] \right\rangle \right\} \\
& + \alpha_{N', M'-2} \left\{ \frac{1}{8} \left\langle \frac{1}{8} [-3(2|m| + 1)N' - N'^2] + 4\mu^2 [(2|m| + 1)N' + N'^2] \right. \right. \\
& \quad \left. \left. - [-(2|m| + 1)(M' - 2) - (M' - 2)^2] \left(\frac{1}{8} - \frac{\mu^2}{2} \right) \right\rangle \right. \\
& \quad \left. + \frac{2\beta}{8} \left\langle \frac{1}{8} [N' - |m|] + 4m\mu - \left(\frac{1}{8} - \frac{\mu^2}{2} \right) [-(M' - 2) + |m|] \right\rangle \right\} \\
& + \alpha_{N', M'} \left\{ \frac{1}{8} \left(\frac{1}{8} - \frac{\mu^2}{2} \right) \left\langle [-3(2|m| + 1)N' - N'^2] + 4\mu^2 [(2|m| + 1)N' + N'^2] \right. \right. \\
& \quad \left. \left. - [-3(2|m| + 1)M' - M'^2] + 4\mu^2 [(2|m| + 1)M' + M'^2] \right\rangle \right. \\
& \quad \left. + \frac{2\beta}{8} \left(\frac{1}{8} - \frac{\mu^2}{2} \right) \left\langle [N' - |m|] + 4m\mu - [M' - |m|] + 4m\mu \right\rangle \right\} \\
& + \alpha_{N', M'+2} \left\{ -\frac{1}{8} \left(\frac{1}{8} - \frac{\mu^2}{2} \right) \left\langle [-3(2|m| + 1)N' - N'^2] + 4\mu^2 [(2|m| + 1)N' + N'^2] \right. \right. \\
& \quad \left. \left. + [-3(2|m| + 1)(M' + 2) + (M' + 2)^2] + 4\mu^2 [(2|m| + 1)(M' + 2) \right. \right. \\
& \quad \left. \left. - (M' + 2)^2] \right\rangle - \frac{2\beta}{8} \left(\frac{1}{8} - \frac{\mu^2}{2} \right) \left\langle [N' - |m|] + 4m\mu + [(M' + 2) + |m| \right. \right. \\
& \quad \left. \left. - 4m\mu \right\rangle \right\}
\end{aligned}$$

$$\begin{aligned}
& +\alpha_{N',M'+4} \left\{ -\frac{1}{8} \left\langle \frac{1}{8} ([-3(2|m|+1)N' - N'^2] + 4\mu^2[(2|m|+1)N' + N'^2]) \right. \right. \\
& \quad \left. \left. + \left(\frac{1}{8} - \frac{\mu^2}{2} \right) [-(2|m|+1)(M'+4) + (M'+4)^2] \right\rangle \right. \\
& \quad \left. - \frac{2\beta}{8} \left\langle \frac{1}{8} ([N' - |m|] + 4m\mu) + \left(\frac{1}{8} - \frac{\mu^2}{2} \right) [|m| - (M'+4)] \right\rangle \right\} \\
& +\alpha_{N'+2,M'-2} \left\{ \frac{1}{8} \left\langle \frac{1}{8} ([-3(2|m|+1)(N'+2) + (N'+2)^2] + 4\mu^2[(2|m|+1)(N'+2) \right. \right. \\
& \quad \left. \left. - (N'+2)^2]) + \left(\frac{1}{8} - \frac{\mu^2}{2} \right) [-(2|m|+1)(M'-2) - (M'-2)^2] \right\rangle \right. \\
& \quad \left. + \frac{2\beta}{8} \left\langle \frac{1}{8} ([N'+2] + |m|) - 4m\mu + \left(\frac{1}{8} - \frac{\mu^2}{2} \right) [-(M'-2) + |m|] \right\rangle \right\} \\
& +\alpha_{N'+2,M'} \left\{ \frac{1}{8} \left(\frac{1}{8} - \frac{\mu^2}{2} \right) \left\langle ([-3(2|m|+1)(N'+2) + (N'+2)^2] \right. \right. \\
& \quad \left. \left. + 4\mu^2[(2|m|+1)(N'+2) - (N'+2)^2]) + ([-3(2|m|+1)M' + M'^2] \right. \right. \\
& \quad \left. \left. + 4\mu^2[(2|m|+1)M' - M'^2]) \right\rangle + \frac{2\beta}{8} \left(\frac{1}{8} - \frac{\mu^2}{2} \right) \left\langle ([N'+2] + |m|) \right. \right. \\
& \quad \left. \left. - 4m\mu + ([M' - |m|] + 4m\mu) \right\rangle \right\} \\
& +\alpha_{N'+2,M'+2} \left\{ -\frac{1}{8} \left(\frac{1}{8} - \frac{\mu^2}{2} \right) \left\langle ([-3(2|m|+1)(N'+2) + (N'+2)^2] \right. \right. \\
& \quad \left. \left. + 4\mu^2[(2|m|+1)(N'+2) - (N'+2)^2]) - ([-3(2|m|+1)(M'+2) \right. \right. \\
& \quad \left. \left. + (M'+2)^2] + 4\mu^2[(2|m|+1)(M'+2) - (M'+2)^2]) \right\rangle \right. \\
& \quad \left. - \frac{2\beta}{8} \left(\frac{1}{8} - \frac{\mu^2}{2} \right) \left\langle ([N'+2] + |m|) - 4m\mu - ([M'+2] + |m|) - 4m\mu \right\rangle \right\} \\
& +\alpha_{N'+2,M'+4} \left\{ -\frac{1}{8} \left\langle \frac{1}{8} ([-3(2|m|+1)(N'+2) + (N'+2)^2] + 4\mu^2[(2|m|+1)(N'+2) \right. \right. \\
& \quad \left. \left. - (N'+2)^2]) - \left(\frac{1}{8} - \frac{\mu^2}{2} \right) [-(2|m|+1)(M'+4) + (M'+4)^2] \right\rangle \right. \\
& \quad \left. - \frac{2\beta}{8} \left\langle \frac{1}{8} ([N'+2] + |m|) - 4m\mu - \left(\frac{1}{8} - \frac{\mu^2}{2} \right) [|m| - (M'+4)] \right\rangle \right\} \\
& +\alpha_{N'+4,M'-2} \left\{ \frac{1}{64} \left\langle [-(2|m|+1)(N'+4) + (N'+4)^2] + [-(2|m|+1)(M'-2) \right. \right. \\
& \quad \left. \left. - (M'-2)^2] \right\rangle + \frac{2\beta}{64} \left\langle [|m| - (N'+4)] + [-(M'-2) + |m|] \right\rangle \right\} \\
& +\alpha_{N'+4,M'} \left\{ \frac{1}{8} \left\langle [-(2|m|+1)(N'+4) + (N'+4)^2] \left(\frac{1}{8} - \frac{\mu^2}{2} \right) \right. \right.
\end{aligned}$$

$$\begin{aligned}
& + \frac{1}{8} \left([-3(2|m| + 1)M' - M'^2] + 4\mu^2[(2|m| + 1)M' + M'^2] \right) \rangle \\
& + \frac{2\beta}{8} \left\langle [|m| - (N' + 4)] \left(\frac{1}{8} - \frac{\mu^2}{2} \right) + \frac{1}{8} (|M' - |m|| + 4m\mu) \right\rangle \Bigg\} \\
+ \alpha_{N'+4, M'+2} & \left\{ -\frac{1}{8} \left\langle [-(2|m| + 1)(N' + 4) + (N' + 4)^2] \left(\frac{1}{8} - \frac{\mu^2}{2} \right) \right. \right. \\
& - \frac{1}{8} \left([-3(2|m| + 1)(M' + 2) + (M' + 2)^2] + 4\mu^2[(2|m| + 1)(M' + 2) \right. \\
& \left. \left. - (M' + 2)^2] \right) \right\rangle - \frac{2\beta}{8} \left\langle [|m| - (N' + 4)] \left(\frac{1}{8} - \frac{\mu^2}{2} \right) \right. \\
& \left. \left. - \frac{1}{8} (|(M' + 2) + |m|| - 4m\mu) \right\rangle \right\} \\
+ \alpha_{N'+4, M'+4} & \left\{ -\frac{1}{64} \left\langle [-(2|m| + 1)(N' + 4) + (N' + 4)^2] - [-(2|m| + 1)(M' + 4) \right. \right. \\
& \left. \left. + (M' + 4)^2] \right\rangle - \frac{2\beta}{64} \left\langle [|m| - (N' + 4)] - [|m| - (M' + 4)] \right\rangle \right\}.
\end{aligned}$$

The right-hand side of the same equation is exactly 0 if the density is constant or power-law. When it deviates from these profiles, one decomposes the right-hand side of equation (3.2.6) into different Chebyshev components. The final right-hand side is not analytical and requires numerical integration.

3.3.2 The Separable Case

In the following we attain the relevant algebraic equations, but only for the separable part of equation (2.2.13). This is because in the end we adopted the pseudo-spectral method to solve the full problem. We still solve the separable part using the spectral method, even though it would have been trivial to solve even without the spectral method, as a test of power.

In the separable case, we can decompose the 2-D expansion into the product of two 1-D expansion,

$$g(t_1, t_2) = \left(\sum_{N=0}^{N_{\max}} \zeta_N T_N(t_1) \right) \left(\sum_{M=0}^{M_{\max}} \gamma_M T_M(t_2) \right). \quad (3.3.9)$$

This greatly reduces the number of unknowns in the solution: while expansion 3.3.7 contains $(N_{\max}+1) \times (M_{\max}+1)$ unknown coefficients, there are only $(1+N_{\max})+(M_{\max}+1)$ unknowns in this expansion.

With the following Chebyshev identity transformations (Abramowitz and Stegun 1972),

$$\begin{aligned}
(1-t_i^2)T_n''(t_i) &= t_i T_n'(t_i) - n^2 T_n(t_i), \\
(1-t_i^2)T_n'(t_i) &= -nt_i T_n(t_i) + nT_{n-1}(t_i), \\
2t_i T_n(t_i) &= T_{n-1}(t_i) + T_{n+1}(t_i), \\
2t_i U_n(t_i) &= U_{n-1}(t_i) + U_{n+1}(t_i), \\
T_n'(t_i) &= nU_{n-1}(t_i), \\
2T_n(t_i) &= U_n(t_i) - U_{n-2}(t_i), \\
U_{-1}(t_i) &= 0,
\end{aligned} \tag{3.3.10}$$

we have,

$$\begin{aligned}
\tilde{\mathcal{F}}_1 g(t_1, t_2) = & \frac{1}{32} \left[\sum_{N=0}^{N_{max}} U_{N+2}(t_1) (\zeta_N A_N + \zeta_{N+1} B_N + \zeta_{N+2} C_N + \zeta_{N+3} D_N \right. \\
& \left. + \zeta_{N+4} E_N + \zeta_{N+5} F_N + \zeta_{N+6} G_N) + \text{low - degree terms} \right] \times \\
& \frac{\mu^2}{8} \left[\sum_{M=0}^{M_{max}} U_{M+2}(t_2) (\gamma_M - 3\gamma_{M+2} + 3\gamma_{M+4} - \gamma_{M+6}) + U_2(t_2) \gamma_0 \right. \\
& \left. + U_1(t_2) (-2\gamma_1 + 3\gamma_3 - \gamma_5) + U_0(t_2) (-6\gamma_0 + 4\gamma_2 - \gamma_4) \right]
\end{aligned} \tag{3.3.11}$$

where the functions in capital letters are:

$$\begin{aligned}
A_N &= (1-\mu)^2 [-N(1+2\beta+N) - 2(\beta+N)|m|] \\
B_N &= 4(1-\mu^2) [-(N+1)(3\beta+2(N+1)+1) - (2\beta+3(N+1))|m|] \\
C_N &= \mu^2(N+2) [-13(N+2) - 30\beta+17] + \mu(N+2) [-38(N+2) - 36\beta-2]
\end{aligned}$$

$$\begin{aligned}
& +(N+2)[-13(N+2)+2\beta-15]+32\beta m\mu \\
& -2|m|[\beta(5\mu^2+6\mu+5)+(-\mu^2+18\mu+15)(N+2)] \\
D_N &= 8(1+\mu)(N+3)[(\beta-1)(3+5\mu)-(5+3\mu)|m|] \\
& -2[\beta(5\mu^2+6\mu+5)+(-\mu^2+18\mu+15)(N+3)]|m| \\
E_N &= (N+4)[-(15+17\mu)(1-\mu)+(N+4)(13\mu^2+38\mu+13)] \\
& -2\beta[16m\mu+(15\mu^2+18\mu-1)(N+4)] \\
& +2|m|[\beta(5\mu^2+6\mu+5)+(\mu^2-18\mu-15)(N+4)] \\
F_N &= -4(1-\mu^2)[(N+5)(3\beta-2(N+5)+1)+(-2\beta+3(N+5))|m|] \\
G_N &= -(1-\mu)^2[(N+6)(1+2\beta-(N+6))-2(\beta-(N+6))|m|], \tag{3.3.12}
\end{aligned}$$

and the low-degree terms are

$$\begin{aligned}
& U_0(t_1) \{4\beta[16m\mu-(5\mu^2+6\mu+5)|m|] \zeta_0 \\
& +4(1+\mu)\{\beta[9+7\mu-2|m|(1-\mu)]-(1+|m|)(7+9\mu)\} \zeta_1 \\
& +4[(1+7\mu)(5+3\mu)-2\beta(7\mu^2+4m\mu+10\mu-1) \\
& +2|m|(\mu^2-10\mu-7+\beta(1+\mu)^2)] \zeta_2 \\
& +4(1-\mu^2)[-9\beta+(2\beta-9)|m|+15] \zeta_3 \\
& + (1-\mu)^2[-8\beta+2|m|(\beta-4)+12] \zeta_4 \} \\
& +U_1(t_1) \{-16\beta|m|(1-\mu^2)\zeta_0 \\
& +2\{2[\mu^2-10\mu-7+\beta(-7\mu^2-10\mu+1+8m\mu) \\
& -(-\mu^2+10\mu+7+\beta(3\mu^2+2\mu+3))|m|]\} \zeta_1 \\
& +16(1+\mu)[(\beta-1)(3+5\mu)-(5+3\mu)|m|] \zeta_2 \\
& +[24(7\mu^2+14\mu+3)-2\beta(45\mu^2+54\mu-3+16m\mu) \\
& +6|m|(\mu^2-18\mu-15)+2|m|\beta(5\mu^2+6\mu+5)] \zeta_3 \\
& +4(1-\mu^2)[-12\beta+2|m|(\beta-6)+28] \zeta_4 \\
& + (1-\mu)^2[2|m|(\beta-5)-10(\beta-2)] \zeta_5 \}
\end{aligned}$$

$$+U_2(t_1) [-2\beta|m|(1-\mu)^2\zeta_0]. \quad (3.3.13)$$

In a similar way, we have

$$\begin{aligned} \tilde{\mathcal{F}}_2 g(t_1, t_2) = & \frac{(1-\mu^2)}{32} \left[\sum_{N=0}^{N_{max}} U_{N+2}(t_1) \{ \zeta_N(1-\mu) + \zeta_{N+1}4(1+\mu) + \zeta_{N+2}(5+11\mu) \right. \\ & + \zeta_{N+4}(-5-11\mu) + \zeta_{N+5}(-4(1+\mu)) \\ & \left. + \zeta_{N+6}(-1(1-\mu)) \right\} \\ & + U_2(t_1)\alpha_0(1-\mu) + U_1(t_1) \{ \zeta_0 8(1+\mu) + \zeta_1(6+10\mu) \\ & + \zeta_3(-5-11\mu) + \zeta_4(-4(1+\mu)) \\ & + \zeta_5(-1(1-\mu)) \} \\ & + U_0(t_1) \{ \zeta_0(10+22\mu) + \zeta_1 4(1+\mu) + \zeta_2(-4(1+3\mu)) \\ & + \zeta_3(-4(1+\mu)) + \zeta_4(-1(1-\mu)) \} \Big] \times \\ & \frac{1}{8} \left[\sum_{M=0}^{M_{max}} U_{M+2}(t_2) \{ \gamma_M H_M + \gamma_{M+2} I_M + \gamma_{M+4} J_M \right. \\ & \left. + \gamma_{M+6} K_M \right\} + U_2(t_2) \{ \gamma_0 [-2\beta\mu^2|m|] \} \\ & + U_1(t_2) \{ \gamma_1 [\mu^2(4|m|+4) + 2\beta(4-\mu^2(2+2|m|)+4\mu m)] \\ & + \gamma_3 [-48 + \mu^2(24+6|m|) + 2\beta(12-\mu^2(9-|m|)-4\mu m)] \\ & + \gamma_5 [\mu^2(20-10|m|) + 2\beta(\mu^2(|m|-5))] \} \\ & + U_0(t_2) \{ \gamma_0 [2\beta(-2|m|\mu^2+8\mu m)] \\ & + \gamma_2 [-24 + \mu^2(12+8|m|) + 2\beta(8-4\mu^2-4\mu m)] \\ & \left. + \gamma_4 [\mu^2(12-8|m|) + 2\beta(-\mu^2(4-|m|))] \right\} \end{aligned} \quad (3.3.14)$$

where the functions in capital letters are:

$$\begin{aligned}
H_M &= [\mu^2 (M(1 - M) - 2(|m| + 1)M + \lambda^2) + 2\beta (-\mu^2(M + |m|))] \\
I_M &= [4(M + 2)(M + 1) + \mu^2 ((M + 2)(1 - M) + 2(|m| + 1)(M + 2) - 3\lambda^2) \\
&\quad + 2\beta (4(M + 2) - \mu^2 (3(M + 2) + |m|) + 4\mu m)] \\
J_M &= [-4(M + 4)(M + 5) + \mu^2 ((M + 4)(7 + M) + 2(|m| + 1)(M + 4) + 3\lambda^2) \\
&\quad + 2\beta (4(M + 4) - \mu^2 (3(M + 4) - |m|) - 4\mu m)] \\
K_M &= [\mu^2 ((M + 6)(7 + M) - 2(|m| + 1)(M + 6) - \lambda^2) \\
&\quad + 2\beta (-\mu^2 ((M + 6) - |m|))] \tag{3.3.15}
\end{aligned}$$

Since both the $\tilde{\mathcal{F}}_1 g$ and the $\tilde{\mathcal{F}}_2 g$ terms have the form $G_1(t_1, \zeta_N) \times G_2(t_2, \gamma_M)$, one can equate the parts that contain t_1 and t_2 respectively. Obviously the coefficients ζ_N and γ_M are not coupled. This separation produces two equations, one concerning t_1 , the other t_2 .

We multiply both sides of these resultant equations by $\sqrt{1 - t_1^2} U_{N'}(t_1)$ (or $\sqrt{1 - t_2^2} U_{M'}(t_2)$ where suitable). Integrate over the domains of interest ($t_i \in [-1, 1]$) keeping in mind equation (3.3.8), we arrive at two sets of linear algebra equations that dictate how ζ_N (or γ_M) is related to other $\zeta_{N'}$ (or $\gamma_{M'}$). Each set corresponds to a band-diagonal matrix which is to be inverted to obtain solutions for the expansion coefficients. We set to zero all coefficients that correspond to polynomial degrees higher than our truncation, i.e.g, $\zeta_N(N > N_{\max}) = 0$ and $\gamma_M(M > M_{\max}) = 0$. The total number of linear equations is $(N_{\max} + 1) + (M_{\max} + 1)$.

A few notes are in order.

The coupling among the spectral coefficients γ in equations 3.3.11 & 3.3.14 is such that, coefficient γ_M is only coupled to $\gamma_{M+2}, \gamma_{M+4}, \gamma_{M+6}, \dots$, i.e., other coefficients of the same parity. The same is not true for ζ_N . This parity loyalty also appears in the boundary condition at the equator (eqs. 3.2.9 or 3.2.10). Only $T_M(t_2)$ functions that are either even (M is even) or odd (M) can be included in the expansion for a given inertial-mode.

Therefore for two 1-D expansions each up to the degree N_{\max} and M_{\max} , there are in total of $(N_{\max} + 1) + (M_{\max}/2 + 1)$ unknown coefficients. Similarly for the number of equations.

Given that the original equation is homogeneous, we are allowed to set one of the coefficients for each summation series to be unity to fix the normalization. We let this be $\zeta_0 = \gamma_0 = 1$. However, there is one more unknown, μ , which is to be determined in relation to all the polynomial coefficients. The total number of unknowns is $N_{\max} + M_{\max}/2 + 1$.

To solve for these variables, we need an equal number of linear algebraic equations.

The two boundary conditions at the surface (eqs. 3.2.9 -3.2.10) can be split into $g_1(t_1)g_2(t_2)$, with spectral coefficients for g_1 and g_2 satisfying:

$$-\sum_{N=0}^{N_{\max}} \zeta_N (-1)^N N^2 \sum_{M=0}^{M_{\max}} \gamma_M T_M(t_2) = -\frac{(m - |m|\mu)\mu}{2(1 + \mu)} \sum_{N=0}^{N_{\max}} \zeta_N (-1)^N \sum_{M=0}^{M_{\max}} \gamma_M T_M(t_2), \quad (3.3.16)$$

$$\sum_{N=0}^{N_{\max}} \zeta_N T_N(t_1) \sum_{M=0}^{M_{\max}} \gamma_M M^2 = -\frac{(m - |m|\mu)\mu}{1 - \mu^2} \sum_{N=0}^{N_{\max}} \zeta_N T_N(t_1) \sum_{M=0}^{M_{\max}} \gamma_M, \quad (3.3.17)$$

where we have picked the boundary condition $t_2 = 1$ in eq. (3.2.10). These yield two independent equations for the spectral coefficients.

The remaining equations that are required, of number $N_{\max} + M_{\max}/2 - 1$ would have to come from the equation of motion. This is fewer than the number we could possibly use, $(N_{\max} + 1) + (M_{\max}/2 + 1)$. One therefore has to pick a more pertinent subset from the full set. Our procedure is to discard the ones that concerns the highest degree ones.

In the case of separable PDE, the solution for g_1 and g_2 are pure polynomials. This means that when using the Chebyshev expansion, all Chebyshev higher than a certain degree (ℓ_{\max}) should be identically zero. This maximum degree is

$$\ell_{\max} = 2(n_1 + n_2) + |m|. \quad (3.3.18)$$

This is confirmed in our results (Fig. 3.1) and gives us valuable insights when computing eigenfunctions in the non-separable case.

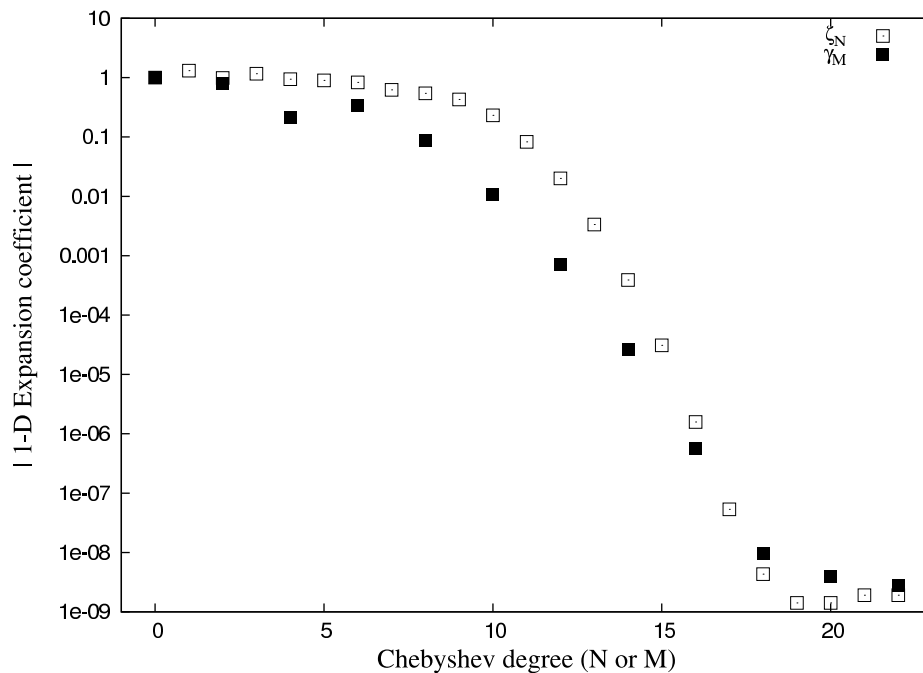


Figure 3.1 The 1-D spectral coefficients (eq. 3.3.9) ζ_N and γ_M for the mode $n_1 = 7$, $n_2 = 2$, $m = 2$, $\mu = 0.3434800519$ in a power-law model with $\beta = 1.5$, plotted here against the degrees of the Chebyshev polynomials. This mode has even-parity. All spectral coefficients with degrees greater than $\ell_{\max} = 2(n_1 + n_2) + |m|$ approaches numerical zero. So the Chebyshev expansion is exact if one truncates above a certain degree.

As a show of capability, we use the above results to obtain eigenfunctions in power-law density spheres (see Fig. 3.1). As said before, this is a total over-kill as the eigenfunction can be (semi-)analytically obtained from the associated ordinary equations, using, e.g., shooting method (see §4.2). However, we show that the spectral method gives identical results as ODE solver and the algebra is reliable.

3.3.3 A Test Run

When the density has a profile $\rho = (1 - r^2)^\beta$, inertial-modes satisfy equations that can be separated into the two ellipsoidal coordinates. We apply our spectral code to this case and compare results against the semi-analytical ones in Wu (2005a).

In order to find μ we need two boundary conditions, both extracted from surface conditions³.

3.4 Pseudo-spectral Method

The section above shows that, even for the simplest case of separable equation, the algebra is time-consuming. For the non-separable case where the 2-D expansion can not be simplified to a product of two 1-D expansions, the algebra is prohibitively complicated. This is exacerbated by the non-separable part in the mode equation – their inner products with the Chebyshev polynomials have to be obtained numerically, for every frequency μ . The computational cost is prohibitively expensive.

This can be circumvented by using the pseudo-spectral method. Instead of keeping count of how the Chebyshev coefficients affect each other, one simply evaluates the left-hand side and the right-hand side of the PDE (eq. 3.2.6) at specific grid points inside the planet and requires that they equal each other. This procedure is also performed for the relevant boundary conditions. In the end, one obtains a new set of linear algebra equations that relate the expansion coefficients to each other. Inverting this set of equations yields α_{NM} .

3.4.1 Principles of the pseudo-spectral method

We first introduce the concepts of Lagrange interpolation and Gaussian quadrature.

³Parity at the equator is automatically satisfied when setting M and M' values as either even or odd. And the expansion on ψ automatically satisfies being finite at the polar axis.

Table 3.1. Eigenfrequencies^a of $|m| = 2$ inertial-modes for two different power-law density profiles, showing excellent agreement with that listed in Wu (2005a).

$(\ell - m)$	parity	$\beta = 1.0$	$\beta = 1.0(\text{Wu})$	$\beta = 2.0$	$\beta = 2.0(\text{Wu})$
1 ^b	o	-0.6667	-0.6667	-0.6667	-0.6667
2	e	-1.1224	-1.1224	-1.0825	-0.8628 ^c
	e	0.4860	0.4860	0.6158	0.6159
3	o	-1.3822	-1.3822	-1.3317	-1.3317
	o	-0.5082	-0.5082	-0.5270	-0.5270
	o	0.9761	0.9761	1.0801	1.0798
4	e	-1.5415	-1.5415	-1.4910	-1.4909
	e	-0.8671	-0.8671	-0.8628	-0.8628
	e	0.2364	0.2364	0.3199	0.3199
	e	1.2408	1.2408	1.3150	1.3150
5	o	-1.6460	-1.6460	-1.5988	-1.5988
	o	-1.1133	-1.1133	-1.0954	-1.0954
	o	-0.4108	-0.4108	-0.4367	-0.4367
	o	0.6673	0.6673	0.7554	0.7554
	o	1.4122	1.4122	1.4654	1.4654

^aEigenfrequencies are presented as $2\mu m/|m| = \text{SIGN}[m]\omega/\Omega$. with positive values denoting pro-grade modes, and negative ones retrograde modes. The integer ℓ (defined in Wu 2005a) indicates the total number of nodal lines in a mode.

^bThis row shows pure r-modes. Both the frequency and the eigenfunction of these modes do not depend on the equation of state, to the lowest order in Ω .

^cThis is likely a typographical error in Wu (2005a).

Table 3.2. Eigenfrequencies^a of $|m| = 2$ inertial-modes for two different power-law density profiles and comparisons with polytropes.

$(\ell - m)$	parity	$\beta = 1.0$	$\beta = 2.0$	$p = k\rho^{2b}$	(L&F99) ^c
1	o	-0.6667	-0.6667	-0.6667	-0.6667
2	e	-1.1224	-1.0825	-1.1000	-1.1000
	e	0.4860	0.6158	0.5566	0.5566
3	o	-1.3822	-1.3317	-1.3578	-1.3578
	o	-0.5082	-0.5270	-0.5173	-0.5173
	o	0.9761	1.0798	1.0258	1.0259
4	e	-1.5415	-1.4909	-1.5196	-1.5196
	e	-0.8671	-0.8628	-0.8629	-0.8629
	e	0.2364	0.3199	0.2753	0.2753
	e	1.2408	1.3150	1.2729	1.2729
5	o	-1.6460	-1.5964	-1.6272	-1.6272
	o	-1.1133	-1.0954	-1.1044	-1.1044
	o	-0.4108	-0.4367	-0.4218	-0.4217
	o	0.6673	0.7554	0.7039	0.7039
	o	1.4122	1.4654	1.4338	1.4339

^aEigenfrequencies for selected power-law density structure, presented as $2\mu m/|m| = \text{sign}(m)\omega/\Omega$ where positive values denote pro-grade modes and negative denote retrograde ones. A spectral method is used to compute the mode s. As Wu (2005a) defined, $l = 2(n_1 + n_2) + |m| - \delta$, where $\delta = 0$ for even parity modes (even $l - |m|$) and 1 for odd parity. Here n_1 and n_2 are the number of nodes in the range $\mu < x_1 < 1$ and $0 < x_2 < \mu$ respectively.

^bWe also present results for a polytrope of index $n = 1.0$ using a pseudospectral method presented in §5.

^cPolytrope $n = 1.0$ frequencies calculated by Lockitch and Friedman (1999).

If we know the values of a function $\psi(x)$ on a list of grid points x_i , we can obtain the value for ψ everywhere else by an N -order interpolation. The so-called Lagrange interpolation formula provides a formal way to proceed:

$$\psi(x) \approx \psi_N(x) = \sum_{i=0}^N \psi(x_i) C_i(x), \quad (3.4.1)$$

where the ‘Cardinal’ function $C_i(x)$ is

$$C_i(x) = \prod_{j=0, j \neq i}^N \frac{x - x_j}{x_i - x_j}. \quad (3.4.2)$$

Obviously $C_i(x_j) = \delta_{ij}$. This expansion is exact if $\psi(x)$ is a polynomial with no more than degree N .

Such an interpolation routine provides a natural way to integrate the function $\psi(x)$,

$$\int_a^b \psi(x) dx \approx \sum_0^N w_i \psi(x_i), \quad (3.4.3)$$

where the weight function

$$w_i = \int_a^b C_i(x) dx, \quad (3.4.4)$$

and $x \in [a, b]$. The weight function can be easily tabulated in advance if the grid points are known.

The above is still rather formal but here comes the interesting development. If we have a family of orthogonal functions on $x \in [a, b]$ and with weight function $\rho(x)$ (see, e.g., eq. 3.3.8), and we choose the grid x_i to be a special set of collocation points (see below), one can show that

$$\int_a^b \psi(x) \rho(x) dx = \sum_0^N w_i \psi(x_i), \quad (3.4.5)$$

is *exact* for all $\psi(x)$ that are polynomials with degree $\leq 2N + 1$ (Davis 1975). This method of integration is called the Gaussian quadrature (Boyd 2001).

Since w_i can be pre-tabulated, the integration only entails evaluating the function ψ at a few pre-determined points. For the same computation cost, Gauss quadrature

reaches higher degree of accuracy than the simple-minded integration where the grid points are equally spaced. Some of the more commonly encountered examples of Gaussian quadrature include the trapezoidal rule and the mid-point rule for integration.

For instance, the inner product $\langle \phi_n, \psi \rangle$ can be obtained using Gaussian quadratures,

$$\langle \phi_n, \psi \rangle \equiv \int_a^b \phi_n(x) \rho(x) \psi(x) dx \approx \sum_0^N w_i \phi_n(x_i) \psi(x_i), \quad (3.4.6)$$

as long as x_i are the properly selected collocation points.

To ensure the accuracy of the Gauss quadrature, as well as that of the pseudo-spectral method, choosing the optimum collocation points is of utmost importance. We repeat here some results from Boyd (2001).

There are two equivalently effective sets of collocation points. One is called the ‘Gauss-Jacobi’ grid (or the ‘Chebyshev-root’ grid), the other is called the Gauss-Lobatto grid (or the ‘Chebyshev-extrema’ grid). The former consists in taking the collocation points to be the zeros in the $N + 1$ degree polynomial, $T_{N+1}(x)$. For Chebyshev, the $N + 1$ roots are,

$$x_i = -\cos \left[\frac{2(i-1)\pi}{2(N+1)} \right] \quad i = 1, 2, \dots, N+1. \quad (3.4.7)$$

These grid points are roughly spaced by $1/N$ in the interior, and much more closely spaced (by $\mathcal{O}(1/N^2)$) near the border ($x = \pm 1$). Such a spacing overcomes the tendency for the interpolation routine to be wildly inaccurate near the boundary of interpolation.

The Gauss-Lobatto branch places the collocation points to be at the zeros of the derivative of $T_N(x)$, as well as the two endpoints ($x = \pm 1$). The extrema of dT_N/dx coincide with the roots of $U_{N-1}(x)$. Combining $N - 1$ extrema and 2 endpoints, still gives a total of $N + 1$ collocation points:

$$x_i = -\cos \left[\frac{i\pi}{N} \right] \quad i = 0, 1, \dots, N. \quad (3.4.8)$$

Such grids are preferable to the Gauss-Jacobi grids when the boundary conditions at the endpoints are not singular, since then one can furnish the boundary condition instantly

using the boundaries as grid points.

Consider the same ODE as in equation (3.3.4). We again expand ψ using a set of orthogonal polynomials, $\psi = \sum_{n=0}^N \alpha_n \phi_n(x)$. Similar to the spectral method, the pseudo-spectral method consists in recasting the ODE into a set of linear equations,

$$\mathbf{H} \cdot \boldsymbol{\alpha} = \mathbf{f}. \quad (3.4.9)$$

The differences, lie in the definitions of the matrix \mathbf{H} and vector \mathbf{f} ,

$$\begin{aligned} H_{ij} &= [\mathcal{H}\phi_j(x)]|_{x=x_i}, \\ f_i &= f(x)|_{x=x_i}. \end{aligned} \quad (3.4.10)$$

We make a couple of comments here.

In applying the spectral method, if one obtains the inner product not by numerical integration, or orthogonality relations, but using Gaussian quadrature, it is proved (and intuitively deduced) (§4.4 Boyd 2001) that such a spectral method produces identical results to the pseudo-spectral method. This is the reason behind the name ‘pseudo-spectral method’.

To further illustrate this point, multiply equation (3.4.9) by $w_i \phi_n(x_i)$ and sum over i , we find

$$\sum_{i=0}^N \sum_{j=0}^N w_i \phi_n(x_i) [\mathcal{H}\phi_j]_{x=x_i} \alpha_j = \sum_{i=0}^N w_i \phi_n(x_i) f|_{x=x_i}. \quad (3.4.11)$$

This should evoke in one’s memory equation (3.3.5).

The error in the solution when using the pseudo-spectral method (§4.5 Boyd 2001) is bounded by “twice the sum of the absolute values of all the neglected coefficients”. So to reach an accuracy of 10^{-6} in the eigenfunction, one needs to expand the solution to a degree N_{\max} such that coefficients for $N_{\max} + 1$ and above are 10^{-6} smaller than the leading terms. A similar result holds in other cases, such as the truncated Taylor expansion.

3.4.2 Implementation

In solving the 2-D PDE (eq. 3.2.6), we adopt the Gauss-Lobatto collocation grids. These involve the extrema of the highest order Chebyshev polynomials in the expansion (N_{\max} and M_{\max}), as well as the spherical surface ($t_1 = -1$ and $t_2 = 1$). Specifically, we have a set of interior and surface grids. The interior grids are:

$$\begin{aligned} t_{1i} &= -\cos\left(\frac{i\pi}{N_{\max}}\right), & i &= 1, 2, \dots, N_{\max}, \\ t_{2j} &= \cos\left(\frac{j\pi}{M_{\max}}\right), & j &= 1, 2, \dots, M_{\max}/2, \end{aligned} \quad (3.4.12)$$

while the endpoint grids are,

$$t_{2j} = \cos\left(\frac{j\pi}{M_{\max}}\right), \quad j = 0, 1, \dots, M_{\max}/2 \quad (3.4.13)$$

for $t_1 = -1$, and

$$t_{1i} = -\cos\left(\frac{i\pi}{N_{\max}}\right), \quad i = 1, 2, \dots, N_{\max}, \quad (3.4.14)$$

for $t_2 = 1$.

Whenever the grid points step on the surface, we create matrix rows using the boundary conditions (eqs. 3.2.9-3.2.10), while whenever the grid points are in the interior, we obtain matrix elements using equation (3.2.6).

We have to solve for a total of $(N_{\max} + 1) \times (M_{\max}/2 + 1)$ coefficients, as well as the eigenfrequency of the mode. One variable, however, is trivial and sets the overall normalization, which we take to be $\alpha_{00} = 1$. Counting the total number of matrix rows (same as the total number of grid points) produces $(N_{\max} + 1) \times (M_{\max}/2 + 1)$. The system is closed.

The pseudo-spectral method is very versatile. It does not pay attention to whether the PDE is separable or not. It is trivial to incorporate, e.g., the compressional term, an external tidal forcing term, into the equation.

In §5 & §7, we present our results using the pseudo-spectral method. More details concerning the actual numerics are also presented there.

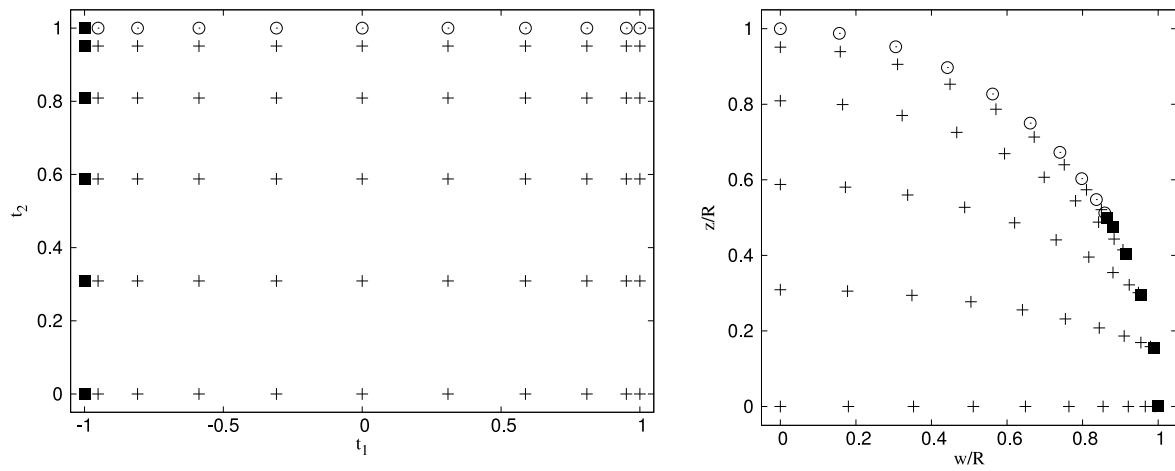


Figure 3.2 An example of the Gauss-Lobatto grid. Here, $N_{max} = M_{max} = 10$. The left-panel shows the equivalent of a quarter meridional plane in the (t_1, t_2) coordinates. Parity of the modes with respect to the equator, as well as our assumed azimuthal dependence, removes the need to show the entire meridional plane. The equator is located at $t_2 = 0$, the rotation axis at $t_1 = 1$, and the surface at $t_1 = -1$ and $t_2 = 1$. Crosses mark interior grid points at which the inertial mode equation (3.2.1) is evaluated, solid squares the location at which the boundary condition at $t_1 = -1$ (eq. 3.2.9) is evaluated, and empty circles locations at which the boundary condition at $t_2 = 1$ (eq. 3.2.10) is evaluated. Right panel: same set of points now portrayed in the meridional cut of a quarter sphere. Here w/R is the normalized polar radius, while z/R is the normalized vertical height.

Chapter 4

Applications: Seismology using Saturn's Rings

4.1 Introduction

The giant planets Jupiter and Saturn are exciting goals for seismic analysis, not just to study what their inner structures are made of, but also in order to reconcile their formation history with the main planetary formation theories: gravitational instability (Boss 1997) and core accretion (Bodenheimer and Pollack 1986). However, despite various observational efforts in the past few decades (Schmider et al. 1991; Deming et al. 1989; Mosser et al. 1993, 1996), no confirmed detection of seismic signals are reported. The hope of using seismic signals to constrain interior models of these planets remains unfulfilled (Mosser 1997).

Voyager I & II (Smith et al. 1981, 1982) have detected a large number of features in Saturn's rings: there are edges (one-side of a gap), gaps (an opening), density waves and bending waves. Some of these have been associated with perturbations by Saturn's many moons (see, e.g. Cuzzi et al. 1981; Holberg et al. 1982), but a large subset remains mysterious (Rosen et al. 1991).

For example, Franklin et al. (1982) pointed out that in the Voyager I data, there are at least two large gaps that do not appear associated with moderate-to-strong satellite resonances. One 200 km gap at $1.434R_S$ (C-ring, $86,700 \pm 700$ km),¹ has an orbital frequency $3/2$ that of Saturn's rotation rate (assumed to have a period of 10h 39.4min). Another 30 km gap at $2.258R_S$ (A-ring, $136,100 \pm 700$ km) is tentatively identified to have $3/4$ of the planet's rotation rate. The authors surmised that these are related to the $\ell = m = 3$ harmonic component of Saturn's gravitational field and suspected the interface modes inside Saturn may be responsible for its non-zero value.² The second gap has later on disappeared in higher resolution Voyager II data (Holberg et al. 1982), while the $3 : 2$ resonance location coincides with the outer edge (as opposed the centre) of the 230 km gap³ and has non-zero optical depth within. Several other similar looking gaps exist in the C-ring.

Hedman et al. (2007) reported structures between $1.178R_S - 1.211R_S$ (D-ring, 71,000 to 73,000 km) that have $m = 2$ rotational symmetry, and an azimuthally periodic pattern at $2.281R_S$ (A-ring, 137,500 km). They identified the former to be a 2:1 Inner Lindblad resonance while the latter a 3:4 Outer Lindblad resonance. This indicates a perturbing period that is comparable to Saturn's rotation period. This could either be caused by internal structure of Saturn, or due to Saturn's magnetic field. The latter may be responsible for many of the features in Jupiter's ring at the so-called 'Lorentz resonances' (Burns et al. 1985). For Saturn, however, the magnetic field is more axisymmetric, and the ring particles are larger (which reduces the charge-to-mass ratio of these grains). Both facts act to suppress the importance of the Lorentz resonances.

Following the first proposal in Marley et al. (1987), Marley and Porco (1993) inves-

¹From now on we measure all distances from Saturn's center and scale all distances by Saturn's radius $R_S = 60,268$ km.

²Permanent non-hydrostatic deformation of Saturn seems unlikely since Saturn is a largely fluid sphere and can not support 'mountains'.

³This, however, may require revisit since the Saturn's rotation period has since been refined. See below.

tigated an intriguing idea. They argued that internal oscillations in Saturn, which is surrounded by a massive, dynamically cold particle disk, could be detected by studying this very ring. They attempted to link the density wave signals in the rings to internal acoustic oscillations. Since the interior of giant planets are convectively unstable, i.e, neutrally buoyant, gravity-modes do not exist. They conclude that the acoustic modes, given enough amplitudes, may produce some of the observed signals both in the D- and the C-rings.

Even earlier, Stevenson (1982) has proposed the hypothesis that Saturn's rings may act as a most sensitive seismograph to detect internal oscillations inside the planet. In particular, he believed that inertial oscillations are more relevant for a fully convective planet like Saturn. However, there has been little progress since largely due to the difficulty in computing inertial mode eigenfrequencies for a given planet structure. This is now becoming possible (Lockitch and Friedman 1999; Lee et al. 1992b,a; Yoshida and Lee 2000; Wu 2005a). We remark that highly accurate eigenfunctions are required in order to calculate reliably the gravitational perturbation associated with an undulating, largely incompressible perturbation (inertial oscillations).

If we can securely associate density wave features with inertial modes, there are a few potential applications. Firstly, inertial modes frequencies are largely independent of sound speed inside the planet, but dependent on the run of density. A successful mode identification therefore reveals the density profile. Secondly, some special inertial modes (r-modes) have frequencies that are largely independent of the density profiles (which only enters to order $(\Omega/\Omega_{\text{breakup}})^2$). Identifying them in the ring would directly measure the internal spin frequency of Saturn. Thirdly, the amplitudes of inertial modes thus inferred results in understanding in turbulent excitation in the convective bulk of the planet.

Inertial modes tend to displace much less mass than acoustic modes of similar radial orders, and their motion is nearly anelastic, implying that they are weakly coupled to

the tidal potential. However, their frequencies (in the rotating frame of the planet) are in the range $0 < \omega < 2\Omega_p$, i.e., they are in the range of Keplerian frequencies of particles on the ring. Therefore we can first explore the locations of the resonances on Saturn's rings and then analyze the strength of their torques versus the available data.

Section 4.2 introduces some basic concepts of wave excitation in disks. In section 4.3 we describe briefly how we obtain solutions for inertial modes and present results on the location and strengths of the resonances. We conclude in §4.4. The calculations of inertial modes in this paper follow closely the approach in Wu (2005a).

Before proceeding, we make two remarks.

The rotation period of Saturn has, surprisingly, been under much debate. Early Voyager measurements of Saturn's long-wavelength (kilo-metric) radio emission suggested a period of 10 hr 39.4 min (Desch and Kaiser 1981), while similar experiment on Cassini produces a period of 10 hr 47.1 min (Giampieri et al. 2006). Using Cassini gravitational data, the rotation period was revised to 10 hr 32.3 min (Anderson and Schubert 2007). The slower radio period obtained earlier is possibly related to magnetosphere slippage relative to the deep interior. An analysis of Saturn's surface jet stream apparently supports the shorter period (Read et al. 2009). At a distance of 100,000 km from Saturn's center, a 7 minutes ($\sim 1.5\%$) uncertainty translates to a distance uncertainty of 1500 km (or $1.5\%R_S$) in the ring (assuming 1 : 1 relation), greater than the ~ 700 km uncertainty from Voyager I data, and much greater than the few hundred meters accuracy in the occultation data from Cassini. We should bear this in mind when later comparing observations against predictions.

In principle, when one calculates resonance locations, one should include corrections due to the non-zero quadrupole moment of Saturn (J_2). However, Saturn's $J_2 \sim 10^{-2}$ and the effect of the quadrupole moment decays outward rapidly. At the surface of Saturn, the value of J_2 is comparable to the fractional uncertainty in Saturn's spin period. So Saturn's J_2 is usually negligible except when one considers apsidal or nodal resonances

(see below).

4.2 Exciting Waves in Disks by inertial Oscillations

4.2.1 Resonances and Waves

We focus here on a perturbation to Saturn's external gravitational potential due to internal oscillations. We follow the formalism initially proposed to study perturbations due external satellites.

In a rotating frame the perturbation can be expressed as:

$$\Phi'(r, \theta, \phi, t) = \Phi'(r, \theta) \exp[i(m\phi - \omega t)], \quad (4.2.1)$$

where (r, θ, ϕ) are spherical coordinates. We adopt the convention that $\omega \geq 0$, while m can be positive, negative or zero⁴. If $m > 0$, the oscillation is a running wave that propagates in the pro-grade direction in the rotating frame, whereas $m < 0$ corresponds to retrograde wave, and $m = 0$ is stationary in the rotating frame. We further define a dimensionless frequency $\mu = \omega/2\Omega_S$ with Ω_S being the spin rate of Saturn. For inertial modes, $\mu \in [0, 1]$.

The pattern speed of this potential perturbation, defined as the angular speed of the frame in which the potential is stationary, is

$$\Omega_{\text{pat}} = \frac{\omega}{m} + \Omega_S = \left(1 + \frac{2\mu}{m}\right) \Omega_S. \quad (4.2.2)$$

The pattern speed is such that pro-grade and retrograde modes in the rotating frame all become pro-grade in the inertial frame, except for some $m = -1$ modes which can remain retrograde in the inertial frame. Moreover when $m = 0$, the pattern speeds in the two frames coincide,

$$\Omega_{\text{pat}} = \omega = 2\mu\Omega_S. \quad (4.2.3)$$

⁴For satellite perturbations, the value m is restricted to $m > 0$.

We now consider the motion of a particle under the time-independent, axisymmetric gravitational field of Saturn, (Murray and Dermott 2000),

$$\Phi_S = -\frac{GM_S}{r} \left[1 - \sum_{n=2}^{\infty} J_n \left(\frac{R_S}{r} \right)^n P_n(\cos \theta) \right], \quad (4.2.4)$$

where P_n is the Legendre polynomials of degree n . Here, we consider only contributions due to the rotational bulge⁵. The $n = 1$ component corresponds to a change in the centre of mass position and can therefore be eliminated from the above expression. The dimensionless multiple moments are expressed as

$$J_n = \frac{1}{M_S R_S^n} \int_0^{R_S} \int_{-1}^{+1} r^n P_n(\cos \theta) \rho(r, \theta) 2\pi r^2 d \cos \theta dr, \quad (4.2.5)$$

with $\rho(r, \theta)$ being the mass density distribution inside Saturn. Assuming that Saturn is symmetric with respect to its equator, $J_{2n+1} = 0$ with $n = 1, 2, \dots$. Saturn's J_2 moment is measured to be $J_2 \sim 1.7 \times 10^{-2}$ (Null et al. 1981).

Let the particle orbit at a distance r from the centre of Saturn. Moving under the axisymmetric potential (equation 4.2.4), it exhibits three frequencies (c.f. Binney and Tremaine 1987), mean motion Ω which is defined as,

$$\Omega^2 \equiv \frac{1}{r} \left(\frac{\partial \Phi_S}{\partial r} \right)_{\cos \theta=0} = \frac{GM_S}{r^3} \left[1 + \frac{3}{2} J_2 \left(\frac{R_S}{r} \right)^2 - \dots \right], \quad (4.2.6)$$

the radial epicyclic frequency κ which is defined as

$$\kappa^2 \equiv \left(r \frac{d\Omega^2}{dr} + 4\Omega^2 \right) = \frac{GM_S}{r^3} \left[1 - \frac{3}{2} J_2 \left(\frac{R_S}{r} \right)^2 - \dots \right], \quad (4.2.7)$$

and the vertical epicyclic frequency which is defined as

$$\nu^2 \equiv \left(\frac{\partial^2 \Phi_S}{\partial z^2} \right)_{\cos \theta=0} = \frac{GM_S}{r^3} \left[1 + \frac{9}{2} J_2 \left(\frac{R_S}{r} \right)^2 - \dots \right]. \quad (4.2.8)$$

These frequencies are such that for a pure Keplerian potential ($J_n = 0$), we obtain $\Omega = \kappa = \nu$. When adopting the epicyclic approximation as is done here, one often

⁵Tidal bulge on Saturn raised by various satellites should produce time-dependent potential perturbations on this ring. However, this should have the same pattern speed in the inertial frame as the potential of the satellites and do not contribute any new perturbing frequencies.

expresses κ as $\Omega - \dot{\varpi}$, and ν as $\Omega - \dot{\Omega}_{\text{asc}}$, where $\dot{\varpi}$ and $\dot{\Omega}_{\text{asc}}$ are the precession rates for the longitude of the pericentre and the longitude of the ascending node, respectively (Murray and Dermott 2000).

If one linearly expands the motion of the above particle around its circular orbit, under a forcing as in equation (4.2.1), one finds that the response diverges whenever⁶

$$\Omega = \Omega_{\text{pat}}, \quad (4.2.9)$$

or

$$m(\Omega - \Omega_{\text{pat}}) = \pm\kappa. \quad (4.2.10)$$

The former is called the co-rotation resonance (CR). If $m > 0$, the latter resonance is usually called the inner (inward of CR) or the outer (outward of CR) Lindblad resonances (ILR and OLR) when the right-hand side takes + or - signs respectively (see, e.g. Goldreich and Tremaine 1982). However, unlike the satellite case where $m > 0$, our m can take any integer values. To fix convention, we rewrite the above expression as

$$|m|(\Omega - \Omega_{\text{pat}}) = \pm\kappa, \quad (4.2.11)$$

this again leads to + sign for ILR and - sign for OLR. For $m = 0$ perturbations, only co-rotation resonances exist.

An analogous definition of the vertical resonances applies if one substitutes κ in the above discussion by ν ,

$$|m|(\Omega - \Omega_{\text{pat}}) = \pm\nu. \quad (4.2.12)$$

The corresponding resonances are called the IVR and OVR respectively, for the inner and outer vertical resonances.

To obtain a simple expression for the locations of LR and VRs, we note that except when $|m| = 1$, the small difference between κ (or ν) and Ω only shifts the exact resonance

⁶We ignore weaker resonances such as $m(\Omega - \Omega_{\text{pat}}) = \pm 2\kappa \dots$

position slightly without affecting resonance dynamics. We ignore this difference and obtain the mean motion at resonances with an inertial mode,

$$\Omega = \Omega_{\text{pat}} \left(\frac{1}{1 \pm 1/|m|} \right) = \frac{1 + 2\mu/m}{1 \pm 1/|m|} \Omega_S, \quad (4.2.13)$$

where '+' sign now stands for OLR/OVR and '-' sign for ILR/IVR.

When $|m| = 1$, the difference between κ and $\dot{\varpi}$ is important: we have an ILR occurring at $\Omega_{\text{pat}} = \pm\dot{\varpi}$ if $m = +1$ and an OLR at the same location for $m = -1$. This resonance is also called the apsidal resonance. We find the location of this resonance to be within $1.1 - 1.9R_S$ only when $m = -1$ and $\mu \sim 1/2 - \epsilon$. When taking these values, Ω_{pat} is very small and can match $\dot{\varpi}$ which is much smaller than Ω_s .

Vertical resonances for $m = -1$ perturbations can also include a nodal resonance by which $\omega_{\text{pat}} = \pm\dot{\Omega}$. These, keeping only J_2 term, occur at identical locations as the apsidal resonances. One example of a nodal bending wave is the Titan $(-1 : 0)$ bending wave at $1.286R_S$ which is a prominent feature in C-ring (Rosen and Lissauer 1988).

We have an ILR occurring at $\Omega_{\text{pat}} = \dot{\varpi}$ if $m = +1$ and an OLR at the same location for $m = -1$. This resonance is also called the apsidal resonance (or nodal resonance in the case of VRs). We find the location of this resonance to be within $1.1 - 1.9R_S$ only when $m = -1$ and $\mu \sim 1/2 - \epsilon$. When taking these values, Ω_{pat} is very small and can match $\dot{\varpi}$ which is much smaller than Ω_s .

Fig. 4.1 shows the resonance location in the disk for an given inertial mode frequency.

The above diverging response at resonances is the source of resonantly excited waves. These waves propagate away from the resonance center in the cases of LR and VR, but remain locally confined in the case of CR.

To establish the direction of wave propagation, we look at the dispersion relation for density waves in the tight-winding (WKB) limit (Lin and Shu 1971; Goldreich and Tremaine 1979; Binney and Tremaine 1987). Let the wave have an azimuthal number m , frequency ω , and wavevector k , e.g., the surface density perturbation $\propto \exp[i(m\phi - \omega t)] \exp[i \int^r k dr]$. The pattern speed of the wave is $\Omega_{\text{pat}} = \omega/m$. Its wavevector and

frequency are related as

$$(m\Omega - \omega)^2 = \kappa^2 - 2\pi G\Sigma|k| + k^2 c_s^2. \quad (4.2.14)$$

Here, Σ is the surface density, G is Newton's constant and c_s is the local sound speed. Strictly speaking this is an expression for fluid disks but we use it here to describe particle disk which has a somewhat more complicated expression. Define a variable $s = m(\Omega - \Omega_{\text{pat}})/\kappa$ so that $s = 0$ at CR and $s = \pm 1$ at LRs, we can solve for wavevector in equation (4.2.14),

$$|k| = \left[1 \pm \sqrt{1 - Q^2(1 - s^2)} \right] \frac{\kappa}{c_s Q}, \quad (4.2.15)$$

where the Toomre $Q = \kappa c_s / (\pi G \Sigma)$ measures stability of the disk to self-gravity (Toomre 1964). For Saturn's ring, one is usually interested in the long wavelength wave as they are easier to resolve in spacecraft observations. This corresponds to taking the '-' sign in the above equation. Density waves have $k = 0$ at $|s| = 1$ (LRs), and they are evanescent (k complex) within a certain distance $|s|^2 > 1 - 1/Q^2$ away from the co-rotation resonance (turning point, or 'Q barrier'). Dense regions in Saturn's rings has $Q \sim 1$ so the evanescent zone is practically non-existent. Waves which are primarily pressure supported can propagate outside of $|s| = 1$ but no such wave exists in particle disks. Self-gravity is pivotal for propagation of density waves in this case.

Within the propagating cavity of density waves, there are either leading waves ($k < 0$) or trailing waves ($k > 0$). Excitation at LR will pick out waves with the right sign that propagates toward the other end of the cavity. If these waves can reach the turning point without being dissipated, they will be reflected backward. Viscosity in Saturn's rings is likely high enough that reflection is not important. To obtain the sign of k , we note that the group velocity is (Binney and Tremaine 1987)

$$v_g \equiv \frac{\partial \omega}{\partial k} = \text{SIGN}[k] \frac{|k| c_s^2 - \pi G \Sigma}{m(\Omega_{\text{pat}} - \Omega)} = \text{SIGN}[k] \frac{\kappa c_s \left(\pm \sqrt{1 - Q^2(1 - s^2)} \right)}{m(\Omega_{\text{pat}} - \Omega) Q}, \quad (4.2.16)$$

For long-wavelength solution (the '-' branch), $\mathbf{v}_g \propto \mathbf{k}$.

Similar formulation exists for spiral bending waves (Shu et al. 1983). The difference is that bending waves propagate inward from IVR and outward from OVR, opposite of what spiral density waves do.

So in summary, waves excited at ILR propagate away from the planet (the source of the perturbation in our problem), those excited at OLR propagate toward the planets. Waves excited at IVR propagate towards the planet and at OVR away from the planet.

At CRs, $s = m(\Omega - \Omega_{\text{pat}})/\kappa = 0$. Equation (4.2.15) yields

$$|k| = \left[1 \pm \sqrt{1 - Q^2} \right] \frac{\kappa}{c_s Q}. \quad (4.2.17)$$

So unless $Q < 1$, $|k|$ is complex and there is no propagating waves radiating from CR. The role of CR typically lies in confining materials into azimuthal islands as opposed to launching waves.

Axisymmetric ($m = 0$) waves are somewhat special. Dispersion relations for waves excited at the $m = 0$ CRs (where $\omega = \Omega$) satisfy ⁷

$$\omega^2 = \kappa^2 - 2\pi G\Sigma|k| + k^2 c_s^2. \quad (4.2.18)$$

Solving for the wavevector gives

$$|k| = \left[1 \pm \sqrt{1 - \frac{1}{Q^2} \left(1 - \frac{\omega^2}{\kappa^2} \right)} \right] \frac{\kappa}{Q c_s}. \quad (4.2.19)$$

Requiring that the wavevector for the long wavelength branch to be positive, we obtain

$$1 - Q^2 \leq \frac{\omega^2}{\kappa^2} \leq 1. \quad (4.2.20)$$

So this wave is evanescent outside its CR ($\omega = \Omega \approx \kappa$) but propagates inward of it for $Q > 1$ disks, or, the group velocity

$$v_g \equiv \frac{\partial \omega}{\partial k} = \text{SIGN}[k] \left[1 - \sqrt{1 - \frac{1}{Q^2} \left(1 - \frac{\omega^2}{\kappa^2} \right)} - \frac{\kappa}{\omega} \right] < 0. \quad (4.2.21)$$

⁷If $Q < 1$, we obtain gravitational instability and $\omega^2 < 0$.

So the wave is a trailing wave ($k > 0$). What is the effect of such a kind of wave is uninvestigated but interesting. There is no torque exerted on the density waves but it can carry energy flux away from the resonant location. Excitation of such a wave was the subject of study in Bate et al. (2002).

Marley and Porco (1993) do not include the $m = 0$ f-modes (with angular dependence $Y_{\ell 0}(\theta, \phi)$ and frequencies of order $\omega \sim \ell\sqrt{G\rho}$) in their excitation calculation presumably because the CR for this mode should fall near the surface or even inward of Saturn, inside of the inner-most ring particles. $m = 0$ inertial modes can have much lower frequencies than f-modes and we should take account of their CRs.

We summarize these discussions in Fig. 4.1 where we plot the resonant location in the rings for an inertial mode with frequency μ and azimuthal number m . Inertial modes are dense inside $0 \leq \mu \leq 1$, this means that we can always find an inertial mode for a given m and μ . However, only the very low order inertial modes can exert appreciable torque on the rings. We proceed to identify these modes.

4.2.2 Resonant Torques

Ring response at resonance determines observability. This response is quantified by a torque that acts on the resonantly excited waves.

For Lindblad type resonances, Goldreich and Tremaine (1979) derived the following expression for the torque under the assumption of linear hydrodynamic response⁸

$$\frac{T^L}{\Sigma} = - \int \int d^2r (\mathbf{r} \times \nabla \Phi_m) = - \frac{m\pi^2}{\mathcal{D}_L} \left[r \frac{d\Phi_m}{dr} + \frac{2m\Omega}{(m\Omega - \omega)} \Phi_m \right]^2 \quad (4.2.22)$$

where Φ_m is the resonant potential. Here, all quantities are to be evaluated at the location of LR: $(m\Omega - \omega) = \pm\kappa$, since most of the torque is exerted there. Using equations (4.2.6)-

⁸Many studies have shown that this formula is independent of the actual ring forces so long as there is some collective or dissipative effects. See Meyer-Vernet and Sicardy (1987) for an elegant explanation.

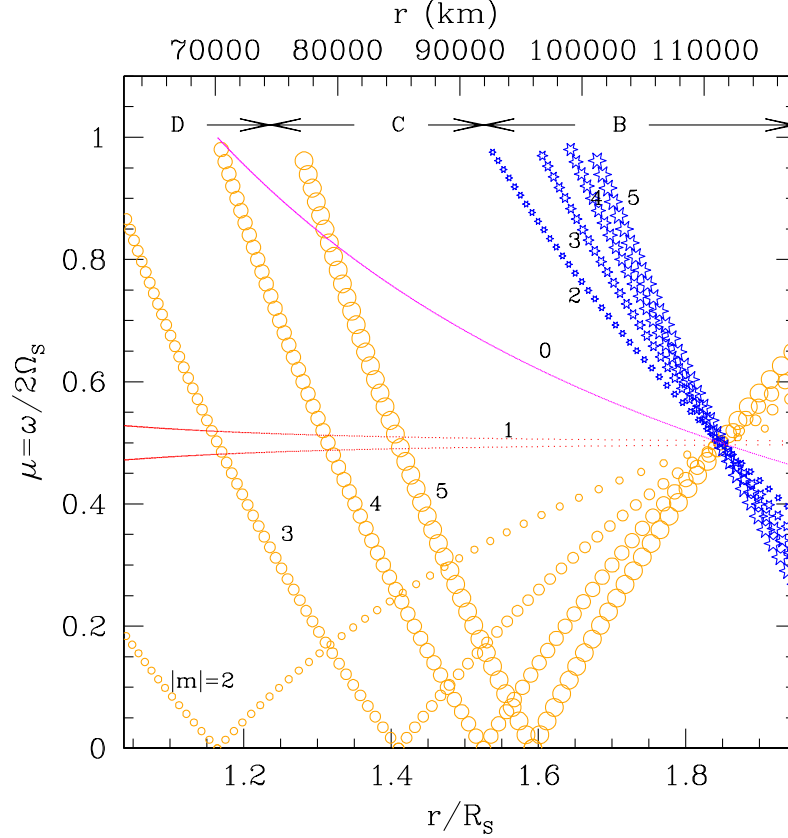


Figure 4.1 We plot here the resonance locations in Saturn's ring, in units of dimensionless distance r/R_S (lower axis) or of distance itself r (in km, upper axis), for inertial modes with frequency $\mu = \omega/2\Omega_S$ in the rotating frame, and an azimuthal number m . The solid line indicates the co-rotation resonance locations for $m = 0$ modes; the dotted line the apsidal resonance and nodal resonance locations for $|m| = 1$ modes, they only occur when mode frequencies $\mu \sim 1/2$. The open circles and open star symbols are LRs and VRs for higher $|m|$ modes, where we use open circles to stand for inner LR or VR, and open star symbols for outer LR or VR. At a distance of $r/R_S \sim 1.85$, the Keplerian motion is synchronous with Saturn's spin. We also demarcate the confines of Saturn's D,C and B rings in the top of the graph. Inertial modes satisfy $0 \leq \mu \leq 1$ and they are dense inside this frequency range. For each value of m , one is destined to find an inertial mode infinitely close to a given frequency μ . However, only the few lowest order inertial modes can exert appreciable torque on the rings. Even so, there are plenty of resonances in the rings, especially in the D and C rings since they are closer to the planet. Here we take Saturn's spin period to be 10 hr 32 min.

(4.2.7), we obtain an expression for \mathcal{D}_L as

$$\mathcal{D}_L \equiv r \frac{d}{dr} [\kappa^2 - (m\Omega - \omega)^2] = -3(1 \mp m)\Omega^2 + \left[\frac{33}{2} + \frac{9}{4}m^2 \pm \frac{3}{4}m \right] J_2\Omega^2. \quad (4.2.23)$$

In deriving this we have kept only terms of order $\mathcal{O}(J_2)$ or lower. The results differ slightly from that given in eq. (19) of Marley and Porco (1993) but the difference only shows up when $(1 \mp m) = 0$. We try to be careful and preserve the difference between Ω and κ because it is important for $|m| = 1$ resonance. We have divided the torque T^L by the surface density of the disk, Σ . This makes the right-hand side independent of disk quantities. This is also convenient when one wants to study the effects on the disk, for instance, compare the resonant torque against the viscous torque. Both scale linearly with Σ . The angular momentum corresponding to the resonant torque is deposited wherever the wave is dissipated.

For bending waves, Shu et al. (1983) obtained the following torque expression,

$$\frac{T^V}{\Sigma} = - \int \int d^2r (\mathbf{r} \times \nabla \Phi_m) = \frac{m\pi^2}{\mathcal{D}_V} \left(\frac{d\Phi_m}{d\theta} \right)^2 \quad (4.2.24)$$

where the right-hand side is evaluated at VR and on the mid-plane. We have

$$\mathcal{D}_V \equiv r \frac{d}{dr} [\nu^2 - (m\Omega - \omega)^2] = -3(1 \mp m)\Omega^2 + \left[-\frac{63}{2} + \frac{9}{4}m^2 \pm \frac{39}{4}m \right] J_2\Omega^2. \quad (4.2.25)$$

Again, this differs slightly from Marley and Porco (1993) and the second term on the right-hand side is only important for apsidal or nodal resonances ($1 \mp m = 0$).

We do not have expressions for waves driven at CR. This was not considered previously since the $m = 0$ perturbation from satellites are time-independent and therefore ignored. This is not so for internal oscillations. While the torque for an $m = 0$ perturbation is exactly zero, the energy it imparts to the rings can be non-zero. We estimate it by multiplying the torque formula (eq. 4.2.22) by the pattern speed (ω/m) and take formally the limit of $m- > 0$ (G. Ogilvie, private communication). The rate of energy deposit is thus,

$$\frac{dE/dt}{\Sigma} = -\frac{\omega\pi^2}{\mathcal{D}_L} \left[r \frac{d\Phi_0}{dr} \right]^2 \quad (4.2.26)$$

By studying various satellite resonances in the C-ring, Rosen et al. (1991) concluded that, empirically, resonances that receive a torque per unit surface density greater than

$T^L/\Sigma \sim 10^{16} \text{ cm}^4 \text{ s}^{-2}$ appear to be associated with gaps with embedded ringlets. This is likely because such a strong torque, when locally deposited, tend to remove material from near the resonance region faster than viscosity can diffuse material back.⁹ They also put a limit of $T^L/\Sigma \geq 10^{13} \text{ cm}^4/\text{s}^{-2}$ as the limit for exciting observable wave trains. So a resonant torque value of $10^{13} \leq T^L/\Sigma \leq 10^{16} \text{ cm}^4 \text{ s}^{-2}$ can launch observable density or bending waves.

4.2.3 Unexplained Features in Voyager I data

Table VIII in Rosen et al. (1991) listed a number of unexplained density wave features in Saturn's C ring, while Marley and Porco (1993) listed a few other features in C & D rings which remain mysterious.

4.3 Inertial Modes as Candidates

Saturn is likely fully convective all the way down to the core. In such a fluid body, buoyancy modes (gravity-modes) have zero frequencies and only¹⁰ pressure modes and inertial modes exist. Here, we explore the role inertial modes may play in exciting density waves in Saturn's rings.

4.3.1 Solutions for Inertial modes

Developing from Bryan (1889), Wu (2005a) showed that equations governing inertial modes in power-law density models can be separated in the ellipsoidal coordinates (x_1, x_2) . One can then obtain semi-analytical solutions without much computational cost. We follow her solution method here.

⁹Cuzzi et al. (1981) also discussed that a stronger perturbation causes more nonlinear waves closer to the resonance and hence a stronger local dissipation, as opposed to gradual dissipation many wavelengths away from the resonance.

¹⁰With the exemption of f-modes, as known as surface gravity waves.

We assume Saturn's density profile to be

$$\rho \propto (1 - r^2)^\beta, \quad (4.3.1)$$

where r is the dimensionless radius normalized by the radius of Saturn. Here we take $\beta = 1.5$ as a good approximation to the realistic models. Fig. 4.2 compares this simple model with the full model which includes a solid core and more realistic equation of state (Saumon and Guillot 2004). It is likely that inertial modes can undergo drastic alterations when the realistic model is used (Ogilvie and Lin 2004). We hope, however, that our simplified study may provide motivations for more sophisticated investigations.

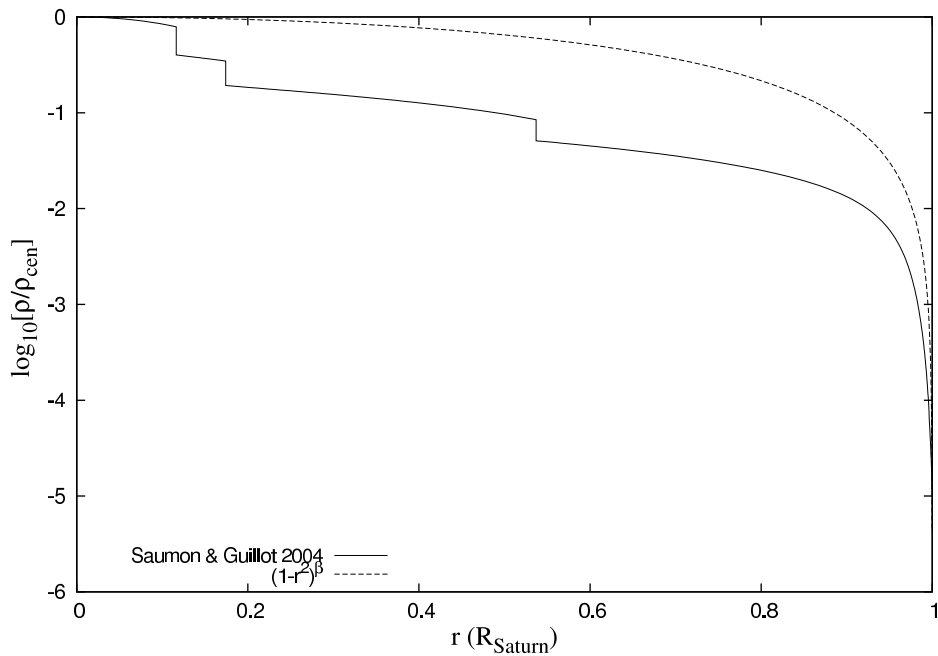


Figure 4.2 Density profile of Saturn as modeled by Guillot (1999). The density is plotted as a function of the dimensionless radius in logarithmic values, normalized by the central density. There are multiple jumps in the density profile associated with various compositional and equation of state variations. In particular, the discontinuity around 0.55 Saturn radius coincides the hydrogen metallic phase transition and helium rain-out. We also show the adopted power-law density profile of index $\beta = 1.5$

The oscillation can be described by a single scalar ψ which is related to the Eulerian

density perturbation as

$$\rho' = \frac{\omega^2 \rho}{c_s^2} \psi e^{i(m\phi - \omega t)}. \quad (4.3.2)$$

It is also related to the displacement vector as (eq. 2.1.18)

$$\boldsymbol{\xi} = \frac{1}{1 - q^2} (1 - iq \mathbf{e}_z \times - q^2 \mathbf{e}_z \mathbf{e}_z \cdot) \nabla \psi. \quad (4.3.3)$$

The scalar eigenfunction ψ satisfies (eq. 2.2.9)

$$(\mathcal{E}_1 - \mathcal{E}_2)\psi = 0, \quad (4.3.4)$$

where the differential operator \mathcal{E}_i is

$$\mathcal{E}_i = \left\{ \frac{\partial}{\partial x_i} \left[(1 - x_i^2) \frac{\partial}{\partial x_i} \right] - \frac{m^2}{1 - x_i^2} + \frac{2\beta x_i (1 - x_i^2)}{x_i^2 - \mu^2} \frac{\partial}{\partial x_i} + \frac{2\mu\beta m}{x_i^2 - \mu^2} \right\}. \quad (4.3.5)$$

The boundary conditions are as in equation (2.3.7) at the surface, and the mode we are interested in can be either even or odd with respect to the equator.

The above equation and boundary conditions are separable in (x_1, x_2) coordinates. For numerical convenience, We transform the variable from $\psi = \psi_1(x_1)\psi_2(x_2)$ to $g_1(x_1)g_2(x_2)$ where

$$\psi_i(x_i) = (1 - x_i^2)^{|m|/2} g_i(x_i). \quad (4.3.6)$$

The solution for g_i can be sought for easily using the shooting method. Fig. 4.3 shows the meridional cut of one such mode we obtain.

4.3.2 Torques by Inertial Modes

The f-modes (Marley and Porco 1993) considered have simple angular dependencies. Each mode is described by a unique Legendre polynomial $Y_{\ell m}(\theta, \phi)$. This is not so for inertial modes. Each inertial mode, even or odd with respect to the equator, can contain multiple $Y_{\ell m}$ components. So we must deviate from the formalism in Marley and Porco (1993) when calculating their gravitational perturbations as well as their torques on the disk.

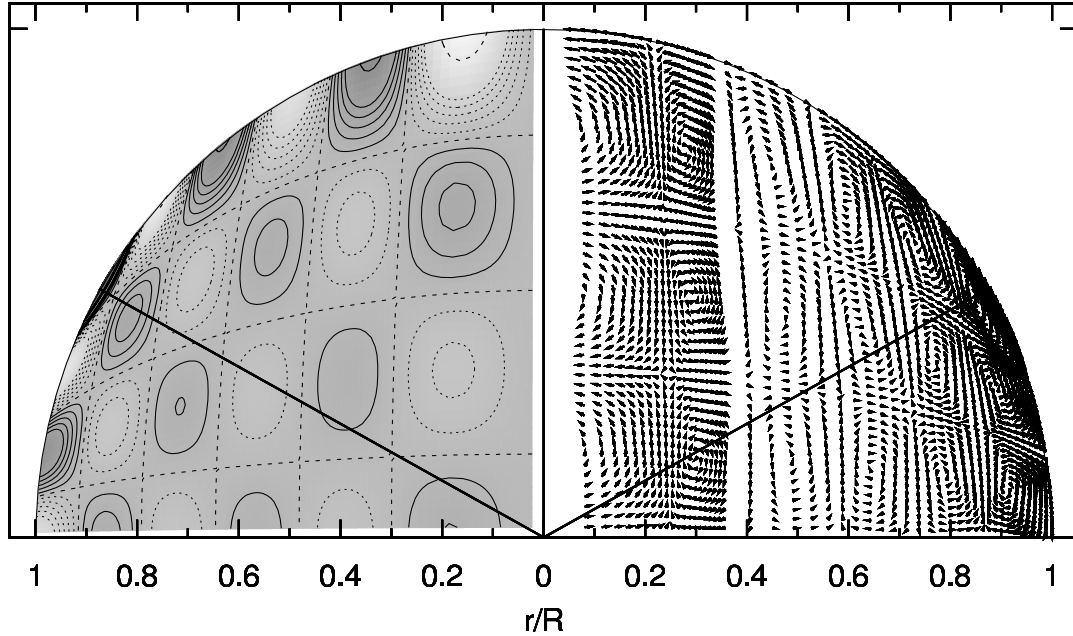


Figure 4.3 A meridional look at an inertial-mode. This mode is symmetric with respect to the equator, retrograde ($m = -2$), and with number of nodes in the x_1, x_2 directions to be $n_1 = 5, n_2 = 3$, respectively. The planet model has a density profile $\beta = 1.5$. The left panel shows the Eulerian density perturbation (ρ'), using both gray-scale and equidistant contours. Lighter regions (and dashed contours) stand for $\rho' < 0$, while darker regions (solid contours) represent $\rho' > 0$. The dotted curves indicate the (x_1, x_2) coordinates. Counting the number of nodes along each coordinate, one recovers n_1 and n_2 . The right panel shows the fluid velocity (v_r & v_θ components only) in the rotating frame as arrows, with the size of the arrows proportional to \sqrt{v} . Both the mode amplitude and the wave-vector remain relatively constant over much of the planet, but rise sharply toward the surface. This rise is most striking near the special angle $|\cos \theta| = \mu = 0.4881$, marked here by straight lines.

Gravitational potential due to inertial mode oscillations (Φ_m) is solved from the Pois-

son equation,

$$\nabla^2 \Phi_m = 4\pi G \rho', \quad (4.3.7)$$

where ρ' is the Eulerian density perturbation due to an inertial mode. It varies as $\exp^{i(m\phi - \omega t)}$ and returns to zero outside the planet. However, Φ_m is not zero (or constant) outside the planet as it has to satisfy boundary condition imposed at the surface of the planet. A general solution to equation (4.3.7) is to use the Green's function $G = -1/(4\pi |\mathbf{r} - \mathbf{r}_1|)$ and write

$$\Phi_m(\mathbf{r}) = - \int \frac{G \rho'(\mathbf{r}_1)}{|\mathbf{r} - \mathbf{r}_1|} d^3 \mathbf{r}_1. \quad (4.3.8)$$

The integration here is over the volume of the planet. Since the Green's function can be written as a summation of $Y_{\ell m}$ functions, Marley and Porco (1993) need only to look at, for a given f-mode, one component of the Green function. Such a convenience does not exist for inertial modes.

Let the spherical coordinates of point \mathbf{r} be (r, θ, ϕ) and that for point \mathbf{r}_1 be (r_1, θ_1, ϕ_1) . We always have $r > r_1$. Green's function satisfy the following expansion into Legendre polynomials,

$$\frac{1}{|\mathbf{r} - \mathbf{r}_1|} = \sum_{\ell=0}^{\infty} \frac{r_1^\ell}{r^{\ell+1}} P_\ell(\cos \gamma), \quad (4.3.9)$$

where P_ℓ is the Legendre polynomial and γ is the angle between \mathbf{r} and \mathbf{r}_1 , and it can be expressed as

$$\cos \gamma = \cos \theta \cos \theta_1 + \sin \theta \sin \theta_1 \cos(\phi - \phi_1). \quad (4.3.10)$$

We resort to the following addition theorem for Legendre polynomials,

$$P_l(\cos \psi) = \frac{4\pi}{2l+1} \sum_{m=-l}^{m=l} (-1)^m Y_l^{-m}(\theta_1, \phi_1) Y_l^m(\theta, \phi), \quad (4.3.11)$$

with the spherical harmonics function related to the associated Legendre polynomials P_ℓ^m as

$$Y_l^m(\theta, \phi) = \sqrt{\frac{2l+1}{4\pi} \frac{(l-m)!}{(l+m)!}} P_l^m(\cos \theta) e^{im\phi}. \quad (4.3.12)$$

Substituting the above relations into equation (4.3.8) and integrate over ϕ_1 , it becomes obvious that Φ_m has the same azimuthal dependence as ρ' and¹¹

$$\begin{aligned}\Phi_m &= - \sum_{\ell=|m|}^{\infty} \frac{(-1)^m 2\pi G}{r^{\ell+1}} P_{\ell}^m(\cos \theta) e^{im\phi} \int \rho'(r_1, \theta_1) r_1^{\ell} P_{\ell}^{-m}(\cos \theta_1) r_1^2 \sin \theta_1 dr_1 d\theta_1 \\ &= \sum_{\ell=|m|}^{\infty} \frac{2\pi G R_S^2}{r^{\ell+1}} \frac{(\ell-m)!}{(\ell+m)!} P_{\ell}^m(\cos \theta) e^{im\phi} \int \rho'(r_1, \theta_1) r_1^{\ell} P_{\ell}^m(\cos \theta_1) r_1^2 \sin \theta_1 dr_1 d\theta_1.\end{aligned}\tag{4.3.13}$$

where in the last line we have normalized the lengths r, r_1 by the radius of Saturn, R_S , and we have used the identity rule for the associated Legendre polynomial,

$$P_{\ell}^{-m} = (-1)^m \frac{(\ell-m)!}{(\ell+m)!} P_{\ell}^m.\tag{4.3.14}$$

Marley and Porco (1993) deal with f-modes, each of which is described by a single spherical harmonics, there is no summation over ℓ for them.

As we adopt the ellipsoidal coordinates to solve for inertial modes, we change variables of integration in equation (4.3.13) to the set (x_1, x_2) , where in particular

$$r_1^2 = 1 - \frac{(x_1^2 - \mu^2)(\mu^2 - x_2^2)}{(1 - \mu^2)\mu^2},\tag{4.3.15}$$

and the Jacobian of the transformation is derived in Wu (2005a) as

$$r_1^2 dr_1 \sin \theta_1 d\theta_1 = \frac{x_1^2 - x_2^2}{(1 - \mu^2)\mu^2} dx_1 dx_2.\tag{4.3.16}$$

We also need the following spatial derivatives:

$$\begin{aligned}r \frac{d\Phi_m}{dr} &= - \sum_{\ell=|m|}^{\infty} \frac{-(\ell+1)\pi G R_S^2}{r^{\ell+1}} \frac{(\ell-m)!}{(\ell+m)!} P_{\ell}^m(\cos \theta) e^{im\phi} \times \\ &\quad \int \rho'(r_1, \theta_1) r_1^{\ell} P_{\ell}^m(\cos \theta_1) r_1^2 \sin \theta_1 dr_1 d\theta_1. \\ \frac{dP_{\ell}^m(\cos \theta)}{d\theta} &= \frac{\ell \cos \theta P_{\ell}^m(\cos \theta) - (\ell+m) P_{\ell-1}^m(\cos \theta)}{\sqrt{\sin^2 \theta}}.\end{aligned}\tag{4.3.17}$$

¹¹The factor 2π comes from ϕ integration, though one should use π in real calculations as we should have used the real part of all quantities.

For our problem, we need to evaluate the potential at the mid-plane ($\cos \theta = 0$). Since the LR torque scales quadratically with $P_\ell^m(\cos \theta)$, while the VR torque scales quadratically with $dP_\ell^m(\cos \theta)/d\theta$, it is obvious that only $\ell + m = \text{even}$ terms contribute to the LR torque, while $\ell + m = \text{odd}$ terms contribute only to the VR torque. This further reduces the number of terms one need to calculate.

4.3.3 Results

To correspond to Fig. 4.1 (which is only schematic), we show in Fig. 4.4 resonance locations associated with individual inertial modes that we obtain. These resonances pop up everywhere in the B,C and D rings.

The biggest assumption we have to make concerns the amplitudes of the modes. We follow Marley and Porco (1993) in fixing the mode energy to be

$$E_{\text{mode}} = \frac{\omega^2}{2} \int d^3r \rho \xi \cdot \xi = 10^{26} \text{ ergs.} \quad (4.3.18)$$

For f-modes considered in Marley and Porco (1993), this corresponds roughly to a displacement amplitude at the surface of $\xi_{\text{max}} = 100 \text{ cm}$. Inertial modes have $\xi_r = 0$ at the surface, and ξ_h reaching maximum values at the critical co-latitude $\cos \theta = \mu$. With the above mode energy, the lowest order inertial mode has maximum $\xi_h = 750 \text{ cm}$, while a medium order inertial mode ($n_1 = n_2 = 5$) has maximum¹² $\xi_h = 13,000 \text{ cm}$. How inertial modes can be excited and reach energy equipartition with convective eddies is yet to be studied.

With this highly uncertain assumption, we obtain gravitational torques associated with individual inertial modes (Fig. 4.4) as well as with f-modes (Fig. 4.5). The latter agree in large with results from Marley and Porco (1993). In particular, we report the quantity T/Σ , torque divided by the local disk surface density. This representation of the torque is independent of the properties of the disk. The tabular form for the same data

¹²High order modes need large amplitudes in order to produce similar energies as low-order modes.

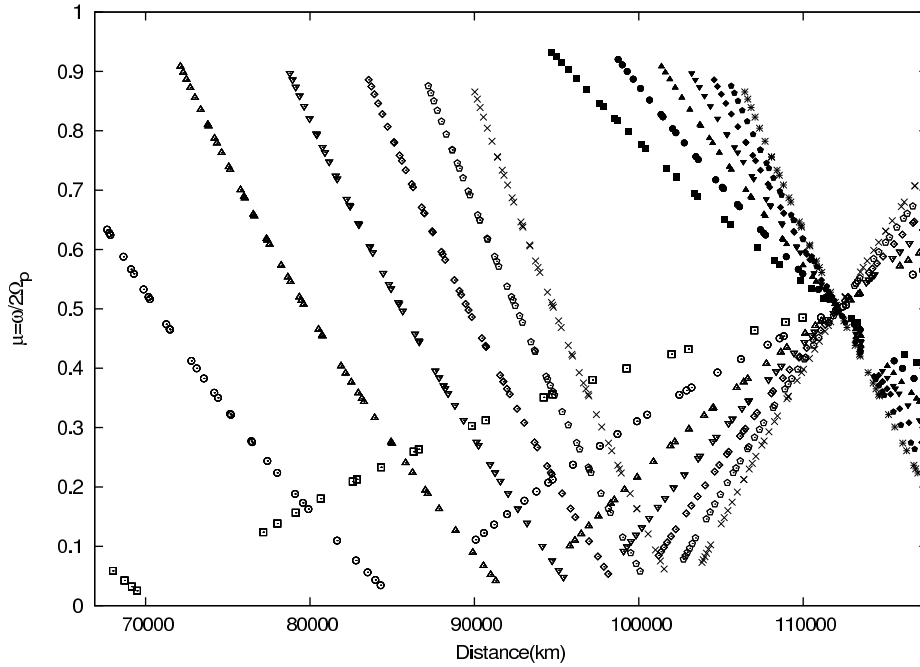


Figure 4.4 Resonant locations of various inertial modes, obtained in a $\beta = 1.5$ power-law model. Squares represent $|m| = 2$ modes, circles $|m| = 3$, triangles $|m| = 4$, upside-down triangles $|m| = 5$, diamonds $|m| = 6$, pentagons $|m| = 7$ and lastly, axes $m = |8|$ modes. Resonance triggered by a retrograde mode is always located farther away from Saturn than that by a pro grade mode of the same $|m|$ value. Filled points represent outer resonances while empty points represent inner resonances. For a given m value, the spectrum of inertial modes is dense within the range $\mu \in [0, 1]$. Only some low order modes are plotted here. The special point at $r/R_S = 1.825$ (110,000 km) corresponds to $\mu = 1/2$, and is the location at which inner resonances with $m < 0$ coincide with outer resonances with $m > 0$.

plotted in Fig. 4.6 is presented in Table 4.1, where we include all resonances that have $T/\Sigma > 10^{10} \text{ cm}^4/\text{s}^2$. Comparing inertial modes with f-modes, it seems that the lowest order inertial modes, at the same mode energy, exert torques on the disk that are either comparable or weaker by a couple magnitudes.

R-modes (with $\ell - |m| = 0$) are not included in Table 4.1. They are largely toroidal modes with small compressibility.

[!htb]

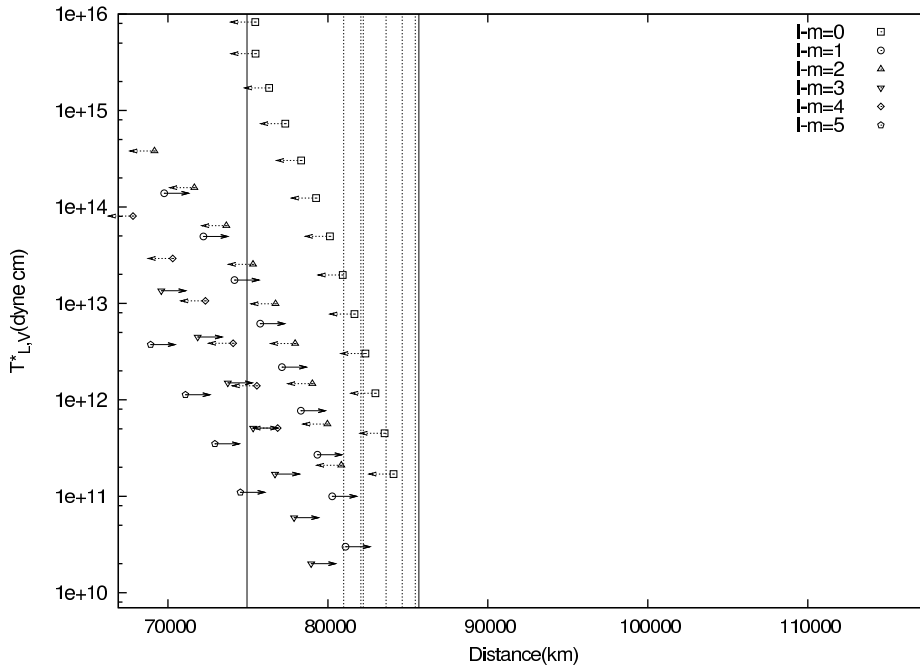


Figure 4.5 Our attempt at reproducing the results of Marley and Porco (1993). Here, torques (measured as T/Σ) by individual f-modes are plotted against their respective resonant locations in the rings. Different symbols stand for modes with different $\ell - m$ values and we adopt a model by Saumon and Guillot (2004). Magnitudes of the torques are compatible with those found by Marley and Porco (1993), but the resonant positions have shifted slightly. Arrows pointing towards Saturn are OLRs and pointing away from Saturn are OVRs. Vertical lines indicate locations where unexplained features exist as observed by Voyager (Rosen et al. 1991), with waves traveling toward Saturn as solid lines, and those away from Saturn as dashed lines.

Table 4.1: Inertial modes that have torque density, $T^* = T_{L,V}/\Sigma > 10^{10} \text{ cm}^4/\text{s}^2$, in the region between *B* to *D* rings. Each mode is labeled by (m, n_1, n_2) , a normalized frequency in Saturn's rotating frame of $\mu = \omega/2\Omega_S$ and a mode index ($\ell - |m|$, last column). Even $\ell - |m|$ modes are symmetric with respect to the equator, while odd $\ell - |m|$ modes are antisymmetric. The column 'type' indicates type of resonances, the column *r* location of the resonance. Column P_{pat} records the pattern period, and the column T^* that of the torque density. Here we have included the strongest modes with $T^* \geq 10^{10} \text{ cm}^4/\text{s}^2$. Each mode is assumed to have equal kinetic energy of $E_{mode} = 10^{26}$ ergs. For $m = 0$ modes, we have calculated the energy flux, multiply it by mode frequency to obtain the torque value here. The physical torque should be identically zero as the pattern speed is zero.

m	n_1	n_2	μ	type	$r(\text{km})$	r/R_{Saturn}	$P_{\text{pat}}(\text{min})$	$T^*(10^{15} \text{ dyne cm})$	$l - m $
-6	0	1	0.2943	ILR	106,474	1.77	708.9	0.00001	2
-5	0	1	0.1667	IVR	101,277	1.68	685.0	0.00003	1
-5	0	1	0.3324	ILR	106,375	1.77	737.4	0.00005	2
-4	0	1	0.2000	IVR	99,393	1.65	710.4	0.00017	1
-4	0	1	0.3822	ILR	106,722	1.77	790.4	0.00022	2
-4	1	1	0.1723	IVR	98,386	1.63	699.6	0.00002	3
-3	0	1	0.2500	IVR	96,724	1.6	767.2	0.00123	1
-3	0	1	0.4503	ILR	108,667	1.8	913.6	0.00087	2
-3	1	1	0.2073	IVR	94,581	1.57	741.9	0.00013	3
-3	1	1	0.3674	ILR	103,298	1.71	846.8	0.00004	4
-3	2	1	0.1768	IVR	93,124	1.55	724.8	0.00001	5
-2	0	1	0.3333	IVR	92,651	1.54	959.0	0.01211	1
-2	1	1	0.2595	IVR	86,389	1.43	863.5	0.00178	3
-2	1	1	0.4322	ILR	103,110	1.71	1125.9	0.00019	4
-2	2	1	0.2128	IVR	82,931	1.38	812.2	0.00026	5
-2	2	1	0.3561	ILR	94,825	1.57	993.0	0.00002	6
0	1	1	0.6794	LCR	91,493	1.52	470.6	0.00196	4
0	1	2	0.7709	VCR	84,098	1.4	414.7	0.00031	5
0	2	1	0.5095	LCR	110,840	1.84	627.5	0.00002	6
0	1	2	0.8276	LCR	80,215	1.33	386.3	0.00027	6
1	1	1	0.6584	OLR	101,757	1.69	276.0	0.00004	4
1	1	2	0.7435	OVR	97,061	1.61	257.1	0.00001	5
2	1	1	0.5178	OVR	111,359	1.85	421.2	0.00010	3
2	3	0	0.0864	ILR	66,907	1.11	588.5	0.00183	6
3	1	0	0.3230	ILR	75,211	1.25	526.1	0.02161	2
3	1	1	0.5163	IVR	70,324	1.17	475.6	0.00329	3
3	1	1	0.5163	OVR	111,633	1.85	475.6	0.00002	3
3	2	0	0.1731	ILR	79,639	1.32	573.2	0.00061	4
3	1	1	0.6276	ILR	67,849	1.13	450.8	0.00684	4
3	2	1	0.3587	IVR	74,245	1.23	516.0	0.00031	5
3	3	0	0.1097	ILR	81,717	1.36	595.8	0.00003	6

Continued on Next Page...

m	n_1	n_2	μ	type	$r(\text{km})$	r/R_{Saturn}	$P_{\text{pat}}(\text{min})$	$T^*(10^{15} \text{ dyne cm})$	$l - m $
3	2	1	0.4742	ILR	71,321	1.18	485.8	0.00064	6
4	1	0	0.3489	ILR	83,234	1.38	544.4	0.00312	2
4	1	1	0.5139	IVR	79,549	1.32	508.7	0.00028	3
4	2	0	0.1946	ILR	87,090	1.45	582.7	0.00006	4
4	1	1	0.6157	ILR	77,472	1.29	488.9	0.00056	4
4	2	1	0.3583	IVR	83,012	1.38	542.2	0.00002	5
4	1	2	0.6868	IVR	76,100	1.26	475.9	0.00008	5
4	2	1	0.4655	ILR	80,588	1.34	518.7	0.00003	6
4	1	2	0.7392	ILR	75,126	1.25	466.8	0.00013	6
5	1	0	0.3658	ILR	88,308	1.47	557.8	0.00053	2
5	1	1	0.5112	IVR	85,442	1.42	530.8	0.00003	3
5	1	1	0.6053	ILR	83,707	1.39	514.7	0.00007	4
5	1	2	0.7239	ILR	81,641	1.35	495.8	0.00001	6
6	1	0	0.3776	ILR	91,840	1.52	567.9	0.00010	2
6	1	1	0.5962	ILR	88,080	1.46	533.4	0.00001	4
7	1	0	0.3862	ILR	94,451	1.57	575.8	0.00002	2

We note here that in order to trigger waves, the resonant torques have to be small (but not much smaller) in strength compared to the viscous torque $T_v = 3\pi\Sigma\nu\Omega r^2$. If the resonant torque is much greater, the rings can not transport away the excess angular momentum and a gap opens. Rosen et al. (1991) found that the minimum torque for detectable feature corresponds to $T/\Sigma \geq 10^{13} \text{ cm}^4/\text{s}^2$, while resonances with torques $T/\Sigma \geq 10^{16} \text{ cm}^4/\text{s}^2$ open gaps.

4.4 Conclusions

We demonstrate here that given comparable mode energies, inertial modes can be as relevant for exciting waves in the rings as f-modes are. Inertial modes also have the advantage of being populous within the D, C and B rings. Even taking only the lowest

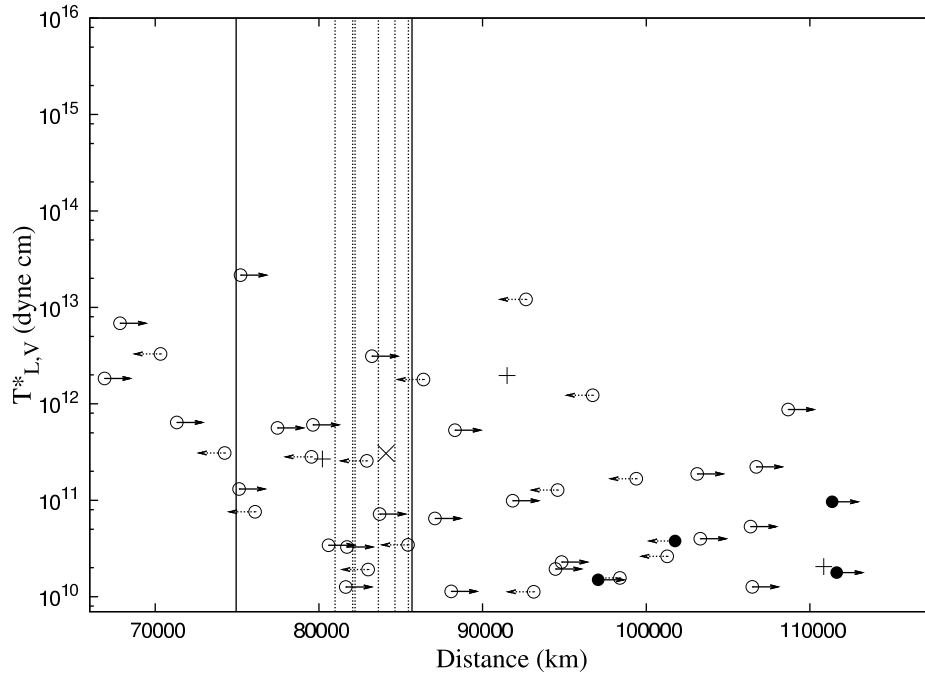


Figure 4.6 Lindblad and vertical torques, normalized by the disk surface density, $T_{L,V}^* = T_{L,V}/\Sigma$, are shown here as a function of ring distance from Saturn. Inertial modes are calculated for a $\beta = 1.5$ density profile, and only those modes that can rise above $T/\Sigma \geq 10^{10} \text{ cm}^4/\text{s}^2$ (an arbitrarily chosen threshold) are included here. Meaning of the myriad set of symbols are: leftward dashed arrows mark the locations of OLR or IVR, while rightward solid arrows those of OVR or ILR; empty circles indicate inner resonances, while filled circles outer resonances. The vertical lines have the same designation as in Fig. 4.5. $m = 0$ modes, exerting zero torque, are not included in this plot. In principle there are many modes that show correspondence in *location* with the observable features, however if the empirical estimations of (Rosen et al. 1991) rosen are considered, then only one mode, the one around $r \sim 75,000$ can be related to the observations, both in the location and in the nature of the mode (the observations used by (Rosen et al. 1991) could not distinguish between OVRs or ILRs, however our model predicts an ILR at that location).

order inertial modes into account, there are plenty locations where one expect to see features.

This paper also serves to highlight the suitability of Saturn's rings as a sensitive seismometer. With a torque sensitivity of $T/\Sigma = 10^{13} \text{ cm}^4/\text{s}^2$, one can observe the effect

of a mountain with mass 10^{13} g, or, 10^{-17} that of Saturn's mass.

Saturn's rings also have high frequency resolution. Assuming a radial resolution of 100 meters, compared this to the ring span of $\sim 100,000$ km, one obtains a frequency resolution of one part in 10^6 .

Chapter 5

Inertial Modes in a Polytrope Model

The pseudo-spectral technique we establish in §3 can in principle be applied to calculate inertial modes in any planetary model. In this section, we test the pseudo-spectral code in two environments, a power-law density planet where the PDE is separable and exact semi-analytical solutions are known (Wu 2005a), and a polytrope density planet where the PDE is not separable. This latter choice is motivated by a few previous studies (Ipser and Lindblom 1990; Lindblom and Ipser 1999; Yoshida and Lee 2000; Lockitch and Friedman 1999; Lee et al. 1992b; Dintrans and Ouyed 2001; Lee et al. 1992a; Papaloizou and Ivanov 2005; Ivanov and Papaloizou 2007; Ipser and Lindblom 1991) where many authors have calculated inertial mode frequencies for polytrope models, using largely the spectral method in spherical coordinates. We will compare our results directly against theirs.

5.1 Solving for the Eigenvalue Problem

Here, we briefly recap the pseudo-spectral method (details see §3.4) and describe in detail our mode finding algorithm.

5.1.1 Finding Eigenvalues and Eigenvectors

The central PDE to be solved (eq. 2.2.13) is converted to the following form (eq. (5.1.1)) after a few changes of variable,

$$(\tilde{\mathcal{F}}_1 - \tilde{\mathcal{F}}_2)g + \frac{C(x_1^2 - \mu^2)(x_2^2 - \mu^2)}{(1 - x_1^2)^{|m|/2}(1 - x_2^2)^{|m|/2}} = 0 \quad (5.1.1)$$

where g is related to ψ as in equation (3.1.2), and two new coordinates (t_1, t_2) are related to the ellipsoidal coordinates (x_1, x_2) linearly as in equation (3.1.3). The expressions for $\tilde{\mathcal{F}}_i$ are given in equations (3.2.7)-(3.2.8). We give here the explicit¹ expression for C , the part that represents the non-separability of the PDE (eq. 2.2.13),

$$C = (1 - x_1^2)^{|m|/2}(1 - x_2^2)^{|m|/2} \times \left\{ -2 \frac{d \ln X}{d \ln t} \left[\frac{(1 - x_1^2)x_1}{(x_1^2 - \mu^2)} \frac{\partial}{\partial x_1} + \frac{(1 - x_2^2)x_2}{(\mu^2 - x_2^2)} \frac{\partial}{\partial x_2} \right. \right. \\ \left. \left. + \frac{m\mu(x_1^2 - x_2^2)}{t} - \frac{|m|x_1}{(1 - x_1^2)} - \frac{|m|x_2}{(1 - x_2^2)} \right] g - \frac{4\Omega^2 R^2}{c_s^2} (x_1^2 - x_2^2)g \right\}. \quad (5.1.2)$$

Again, $X = \rho_{\text{surf}}/\rho = (1 - r^2)^\beta/\rho$ and $t = (x_1^2 - \mu^2)(\mu^2 - x_2^2) = \mu^2(1 - \mu^2)(1 - r^2)$.

Boundary conditions for g (eq. 3.2.9-3.2.10) are

$$\left. \frac{\partial g}{\partial t_1} \right|_{t_1=-1} = -\frac{(m - |m|\mu)\mu}{2(1 + \mu)} g|_{t_1=-1}, \quad (5.1.3)$$

$$\left. \frac{\partial g}{\partial t_2} \right|_{|t_2|=1} = -\text{SIGN}[t_2] \frac{(m - |m|\mu)\mu}{1 - \mu^2} g|_{|t_2|=1}. \quad (5.1.4)$$

We expand the solution for g as (eq. 3.3.7)

$$g(t_1, t_2) = \sum_{N=0}^{N_{\text{max}}} \sum_{M=0}^{M_{\text{max}}} \alpha_{NM} T_N(t_1) T_M(t_2). \quad (5.1.5)$$

where M is chosen to be either even or odd, but not mixed. We adopt square truncation $N_{\text{max}} = M_{\text{max}}$.

The equation of motion (eq. 5.1.1) is evaluated at the Gauss-Lobatto collocation grids in the interior (eq. 3.4.12), while the boundary conditions (eqs. 5.1.3-5.1.4) are

¹We present this expression in terms of variables x_1 and x_2 , as the algebraic expression becomes clumsy in the coordinates t_1 and t_2 . Since we will use the pseudo-spectral method, we do not need the direct algebraic expression in the Chebyshev space, as we can always evaluate t_1 and t_2 at the gridpoints using eq. (3.1.3).

evaluated at the endpoints (eqs. 3.4.13-3.4.14). The spatial derivatives are evaluated analytically using the Chebyshev transformation rules (eq. 3.3.10). This then gives us a linear matrix with $(N_{\max} + 1) \times (M_{\max}/2 + 1)$ rows and equal number of columns, which we invert to solve for equal number of unknowns (one of which is the mode frequency). The matrix form of the homogeneous equation is (eq. 3.3.5)

$$\mathbf{H}(\mu) \cdot \alpha = 0, \quad (5.1.6)$$

where one is free to set a normalization of $\alpha_{00} = 1$ (or $\alpha_{01} = 1$ for odd modes).

If the eigenvalue problem can be phrased in the following form

$$\mathbf{H} \cdot \alpha = \mu \mathbf{J} \cdot \alpha, \quad (5.1.7)$$

where \mathbf{H} and \mathbf{J} are two matrices, and μ is the eigenvalue we are seeking, one can use QR/QZ algorithm which, in one go, produces all possible eigenvalues of the problem. However, our matrix (eq. 5.1.6) can not in general be written in such a form. One is then limited to more local method of finding one eigenvalue at a time.

In our case, the condition for a non-trivial solution of equation 5.1.6,

$$\text{Det}[\mathbf{H}(\mu)] = 0 \quad (5.1.8)$$

constrains the eigenfrequencies. Note that inertial modes have frequencies $\mu \in [0, 1]$. To calculate the above determinant, we use LU decomposition to factorize the matrix into an upper triangular and a lower triangular matrix. The determinant of \mathbf{H} is the product of the determinants for the two triangular matrices, which in turn are simply the products of their diagonal entries, respectively.

However, even if each matrix element contains only orders of μ , this determinant would be a polynomial of degree $I = (N_{\max} + 1) \times (M_{\max}/2 + 1)$. Finding the zeroes of such a large polynomial is tricky, if not conceptually difficult. One issue is round-off error. If evaluation of each matrix element contains a round-off error of $\mathcal{O}(\epsilon)^2$ as the

²We use double precision for all calculations, so the fractional round-off error is $\sim 10^{-16}$.

determinant intrinsically involves computations of I^2 terms, the collective uncertainty scales as $I^2\epsilon$. Alternatively, the accuracies of the eigenvalue is limited to of the same order, or $\sim 10^{-10}$ if $N_{\max} \sim M_{\max} \sim 20$.

Moreover, due to the differential operator \mathcal{F}_i , each matrix element in the matrix \mathbf{H} goes as N^2 (or M^2). The resultant determinant goes as $(I!)^2$. This, if not properly taken care of, causes computer overflow. In practice, when we take the determinant of the LU matrices, we are actually adding up the logarithms of the absolute value of the diagonal terms. This gives us a much larger dynamic range than afforded by a double precision calculation.

Despite this, it is difficult to find true zeroes of the determinant. Due to the truncation error, the eigenvalue can only be pinpointed to 10^{-10} . At this precision, the determinant still hangs around large values, though much smaller than surrounding values. Instead, we use minimization routine to find the eigenvalue. We calculate the determinant scanning through the whole range of μ . This presents a number of minima (see Fig. 5.1). We locate the minima to within a precision range of 10^{-3} . Then we use the Newton Raphson method (Press et al. 1992) to chase after the deepest point. We call the procedure convergent when a precision of 10^{-10} is reached (see above).

For a given converging eigenvalue, we use Gaussian elimination (Press et al. 1992) to invert the matrix and obtain the spectral coefficients.

5.1.2 Spurious Eigenmodes

Results of the pseudo-spectral code needs to be watched carefully. There are two reasons.

First, the minima one finds in the determinant may be real but the inverted spectral coefficients may be off. To protect against this, the most reliable way is to evaluate the residual to the original equations by an independent algorithm (Boyd 2001). A quicker (but less reliable) way is to look at the rate of decrease in the spectral coefficients. If the last coefficient calculated is some 10^{-6} of the largest coefficient, that we have reached

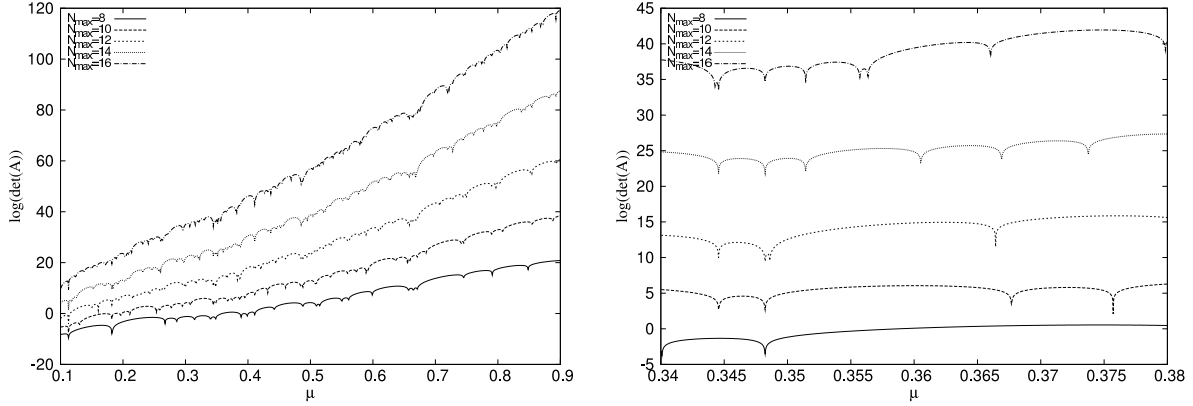


Figure 5.1 A scan of possible eigenmodes in a rotating polytrope of $n = 1.5$. The minimums (spikes) of the plot $\log \det\{A(\mu)\}$ vs μ are possible eigenmodes, the magnitude of the determinant at a given μ increases as the size of the matrix A (higher truncation of the Chebyshev expansion) increases. Boyd (2001) argues that at most half of them are real eigenmodes. (Left) We show here how the determinant of A varies along μ for a series of fixed truncations (they are even because the tidal overlapping problem require even modes, therefore we look for even modes). At a some fixed μ it is easy to see that the minima matches the location of previous ones at different truncations. It is highly likely then that they are real eigenmodes. This is a first criteria to find eigenmodes. It is still required to study the behavior of the spectral coefficients and their convergence. (Right) A zoom-in of the region around $0.34 \leq \mu \leq 0.38$, here we see the lowest order mode, $m = 2$, $n_1 = 1$, $n_2 = 0$, $\mu \sim 0.348$, and mode $m = 2$, $n_1 = 4$, $n_2 = 1$, $\mu \sim 0.344$. All the other minima are either fake modes or high order spurious modes that begin to appear as we add higher degree Chebyshev functions.

convergence of 10^{-6} .

The second reason is the eigenvalue may be spurious. As inherent in any spectral methods with finite expansion terms, one is destined to obtain eigenvalues that are both real and spurious. The spurious ones are typically higher order (say, $n_1 \geq N_{\max}/2$, $n_2 \geq M_{\max}/2$) modes that have their eigenfrequencies misplaced due to the finite truncation and would jump around as the resolution changes. There are also some ‘physical’ spurious modes due to incompatibility between the equation of motion and the boundary conditions. To guard against this, the usual practice is to compare eigenvalues at two different truncations (resolutions). Even this procedure may sometimes fail as inertial modes are everywhere dense inside $\mu \in [0, 1]$.

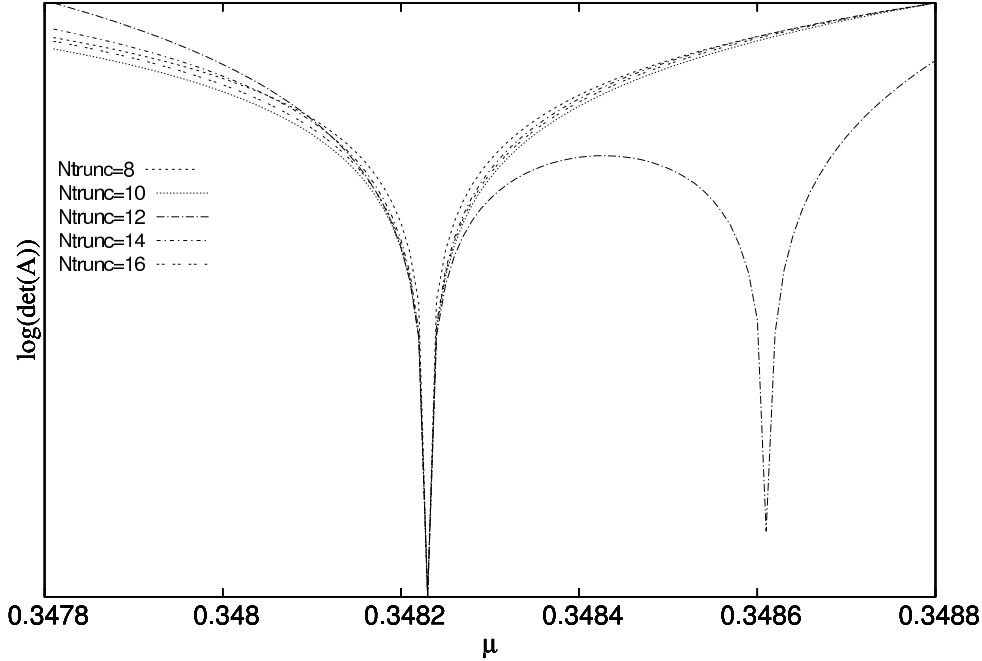


Figure 5.2 A zoom-in of Figure 5.1 around a confirmed mode. Here we normalize the value of $\log \det\{A\}$ in order to show that, for a real eigenmode, the eigenfrequency matches with high precision for different truncations. The mode we show here is the lowest order $m = 2$, $n_1 = 1$, $n_2 = 0$, $\mu \sim 0.348$.

The following is our mode finding algorithm in which we carry out all the requisite safety check:

- we first choose a truncation of $N_{\max} = M_{\max}$ (square truncation). This introduces $(N_{\max} + 1) \times (M_{\max}/2 + 1)$ coefficients. To obtain a mode with (n_1, n_2) nodal lines in the ellipsoidal coordinates, our starting truncation is typically $N_{\max} = M_{\max} \geq (n_1 + n_2)$, since this is when the power-law solution cut-off exactly.
- We calculate the determinant by scanning through the μ range, typically with a μ resolution of 10^{-3} . We then use the Newton-Raphson method to zoom in around the valleys to obtain the very minimum in the determinant. We call the minimization procedure convergent when the resolution in $\mu \leq 10^{-10}$.
- Using a standard normalization of $\alpha_{00} = 1$, we compute the spectral coefficients at each minimum. We can label the eigenfunction that are constructed using these

coefficients according to the number of nodes along the t_1 and t_2 coordinates, respectively. The fact that in a wide range of planet models, the nodal lines always trace the ellipsoidal coordinates closely, speaks volume for the adoption of these coordinates. It is trivial to label the modes and trace them through difference truncations.

- We raise the truncation by, usually, 2 to N'_{\max} and repeat the above steps. Results from **two** subsequent truncations ought to be compared before we proclaim that we have found a real mode:

- when convergence is achieved, the highest degree spectral coefficients should fall below a tolerance threshold. We usually set this to be 10^{-6} .
- for a given eigenfrequency solution that we find at the lower truncation, their counterparts (closest minima in frequency) at the higher truncations need to agree in frequency to within 10^{-8} , the frequency convergence criterion is met. When there is not enough truncation to resolve the mode properly, we typically find that the eigenfrequency (even for a real mode) keeps fluctuating.
- after checking the above criterion, we evaluate the fractional differences between spectral coefficients of the same degree but different truncations. We require that

$$\frac{|\alpha_{NM}(N_{\max}) - \alpha_{NM}(N'_{\max})|}{\alpha_{NM}(N_{\max})} \leq \epsilon, \quad (5.1.9)$$

where ϵ is a user defined tolerance, we set it to be 10^{-2} . Numerically we find that errors in high degree spectral coefficients are greater than those in low degree ones. Fractional errors in these coefficients are also larger because they are themselves smaller. It would be very computational expensive to impose the above criterion on all coefficients. In practice, we require that only coefficients that have values above 10^{-2} to satisfy the above criterion. This is based on two arguments: first, magnitudes of very high degree coefficients,

small as they are, should affect very little mode frequency and structure; second, as shown in Fig. 5.9, even if these high degree spectral coefficients are large and uncertain, as long as the low degree ones are accurate, we should be able to obtain reliable results on the coupling between tide and inertial modes.

- sometimes even after all of the above stringent convergence criteria have been met, we raise the truncation by another 2 to boost confidence level.

Using a 2.3GHz Pentium, we could usually reach truncation as high as 30 in a matter of 30 min for a small root-finding μ range of 10^{-3} .

As an example we present an eigenmode in Figs. 5.3 and 5.4 where we show results from two consecutive truncations.

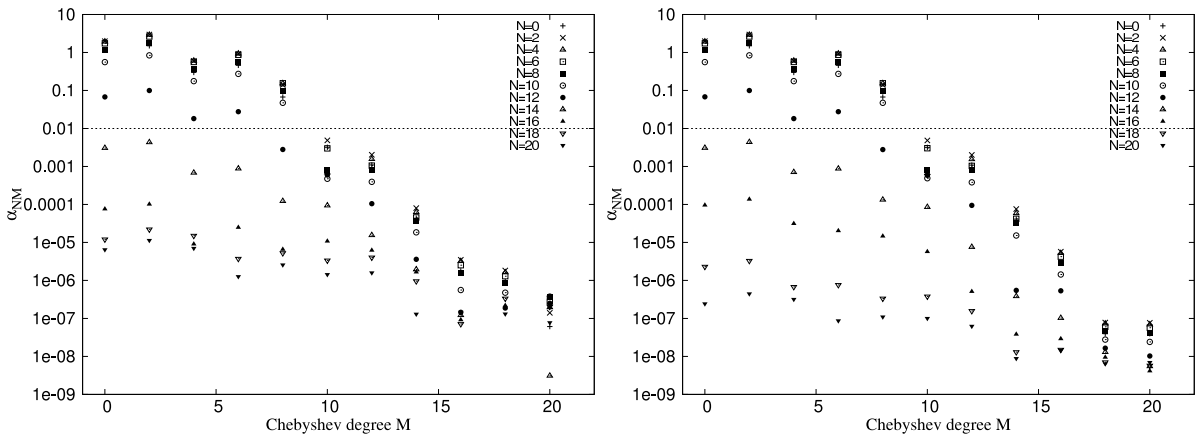


Figure 5.3 Convergence of the Chebyshev spectral coefficients for a mode $m = 2$, $n_1 = 7$, $n_2 = 2$ and $\mu = 0.351436598$ between two subsequent truncations: left-panel, $N_{max} = M_{max} = 20$, right-panel, $N_{max} = M_{max} = 22$. We plot here the magnitudes of the spectral coefficients as functions of their degree M (the horizontal axis), with the degree N indicated by the different types of symbols. This mode is even with respect to the equator so only even M coefficients are non-zero. The highest degree coefficients approach numerical zero, while all coefficients that fall above the dotted line agree between different truncations to better than 1 percent (eq. 5.1.9).

Fig. 5.5 shows a meridional cut for the same eigenmode. In our polytrope density model, the equation for the inertial modes is not separable in the ellipsoidal coordinates. However, the nodal lines run very closely parallel to the coordinate axis. We know this

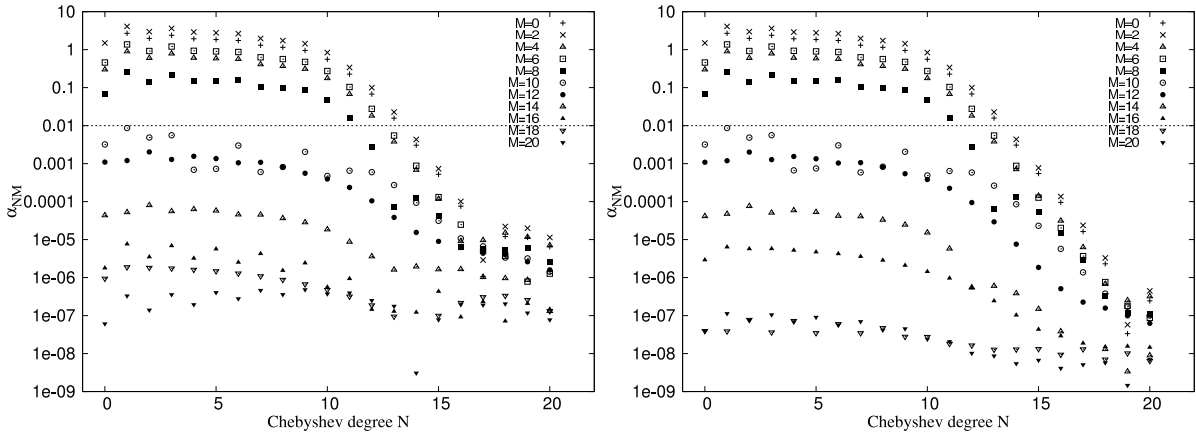


Figure 5.4 Same as in Fig. 5.3 but with the horizontal axis being the degree N and different symbols stand for difference in degree M . Compared to that figure, one notices that the spectral coefficients fall off with degree M more rapidly than with degree N . This is expected as the number of nodes (and therefore richness of spatial structure) in this mode ($n_1 = 7, n_2 = 2$) is higher in the x_1 coordinate. In principle a square truncation ($N_{\max} = M_{\max}$) is not ideal and should be improved upon (see §5.4). Such an insight, incidentally, is not obvious if one insists on solving for inertial modes in spherical coordinates as then the mode typing is ambiguous.

feature occurs for uniform density models (Bryan 1889), power-law density models (Wu 2005a), and now polytrope models. It is then reasonable to expect that it persists for a wide range of density models. As such, we suspect that the quantum numbers one obtains by counting nodal lines along the (x_1, x_2) coordinates are more useful for labeling the modes than counting in any other way (see §5.2).

5.2 Comparison with Previous Studies

We compare our results against those obtained in earlier studies.

We first compare our polytrope results with those using power-law models. There is an exact one-to-one correspondence between modes in two different models (Table 5.2), and the fact that nodal lines always run largely parallel to the (x_1, x_2) coordinates provides accurate mode identification in both models. The difference in eigenfunctions lie in that while for the power-law model, spectral coefficients for inertial modes are zero

Table 5.1. Eigenfrequencies^a of $|m| = 2$ inertial-modes for various density profiles:
comparison between power-law and polytrope.

$(\ell - m)$	parity	$\beta = 1.0$	$p = k\rho^2$	$\beta = 2.0$	$p = k\rho^{3/2}$
1 ^b	o	-0.6667	-0.6667	-0.6667	-0.6667
2	e	-1.1224	-1.1000	-1.0825	-1.0344
	e	0.4860	0.5566	0.6158	0.8277
3	o	-1.3822	-1.3578	-1.3317	-1.2705
	o	-0.5082	-0.5173	-0.5270	-0.5516
	o	0.9761	1.0258	1.0801	1.2171
4	e	-1.5415	-1.5196	-1.4910	-1.4307
	e	-0.8671	-0.8629	-0.8628	-0.8569
	e	0.2364	0.2753	0.3199	0.4569
	e	1.2408	1.2729	1.3150	1.4013

^aEigenfrequencies are listed as $2\mu m/|m| = \text{SIGN}[m]\omega/\Omega$. Therefore positive values denote pro-grade modes, and negative ones retrograde modes. This is opposite to that done in Lockitch and Friedman (1999). Following Wu (2005a) we define $\ell = 2(n_1 + n_2) + |m| - \delta$, where $\delta = 0$ for even-parity and 1 for odd-parity, and n_1, n_2 are the numbers of nodes in the x_1 and x_2 ranges, respectively.

^bThis row represents R-modes. They are mostly toroidal and insensitive to density variations.

Table 5.2. Eigenfrequencies for $|m| = 2$ inertial modes in different polytropes.

$(\ell - m)$	$p = k\rho^2$		$p = k\rho^{5/3}$		$p = k\rho^{3/2}$	
	YL00 ^a	this work	YL00	this work	YL00	this work
1	-0.6667	-0.6667	-0.6667	-0.6667	-0.6667	-0.6667
2	-1.1000	-1.1000	-1.0626	-1.0626	-1.0344	-1.0344
	0.5566	0.5566	0.5566	0.6965	0.8277	0.8277
3	-1.3578	-1.3578	-1.3100	-1.3100	-1.2705	-1.2705
	-0.5173	-0.5173	-0.5356	-0.5356	-0.5516	-0.5516
	1.0259	1.0258	1.1278	1.1278	1.2171	1.2171
4	-1.5196	-1.5196	-1.4722	-1.4721	-1.4307	-1.4307
	-0.8630	-0.8629	-0.8586	-0.8586	-0.8569	-0.8569
	0.2753	0.2753	0.3642	0.3642	0.4569	0.4569
	1.2729	1.2729	1.3419	1.3419	1.4013	1.4013

^aThis and other columns that are marked as YL00 are taken from Table 2 of Yoshida and Lee (2000). Their results agree with those of Lockitch and Friedman (1999) where they overlap.

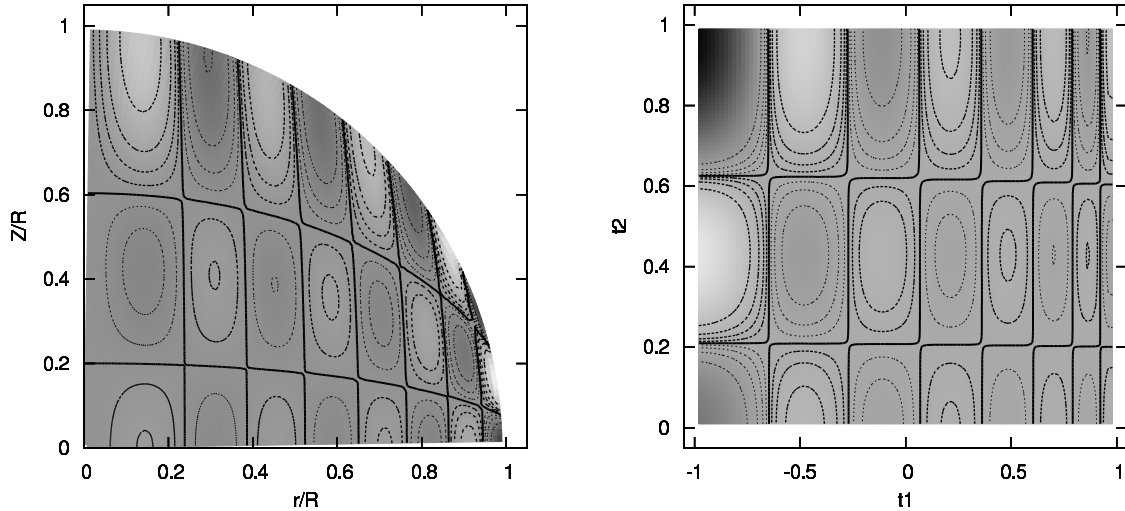


Figure 5.5 A meridional cut for an eigenfunction with quantum numbers $m = 2, n_1 = 7, n_2 = 2$, and eigenfrequency $\mu = 0.351$ in a polytrope model with $n = 1.5$. Left panel: amplitudes for Eulerian density fluctuation plotted in spherical coordinates, with dark patches (light grey dots) being positive values and lighter patches (solid black dots) negative values. Right Panel: the same quantity now projected in ellipsoidal coordinates. The (t_1, t_2) coordinates are linearly morphed from the original (x_1, x_2) coordinates (eq. 3.1.3). Pay attention to the feature that all nodal lines run largely parallel to constant coordinate lines. Moreover, nodes are roughly equally spaced in the ellipsoidal coordinates, while they are more unevenly distributed in spherical coordinates. So to reach the same accuracy, expansion in spherical coordinates will require more number of polynomials.

above certain degrees, they go on to infinity for polytropes. The $m = 2, n_1 = 7, n_2 = 2$ mode shown in Fig. 5.3 has $\mu = 0.350$ for $n_{\text{poly}} = 1.5$ (or $p = k\rho^{5/3}$) while it has a frequency of $\mu = 0.343$ in the $\beta = 1.5$ model (shown in Fig. 5.6).

Many previous studies have also computed (low order) inertial modes in polytrope models. We compare with the most relevant ones, Lockitch and Friedman (1999) for $p = k\rho^2$ polytropes and Yoshida and Lee (2000) for a number of different polytropes, in 5.2 & 5.2. Our frequencies show good agreement with these studies.

We comment on earlier efforts at solving inertial modes. Almost all studies have been

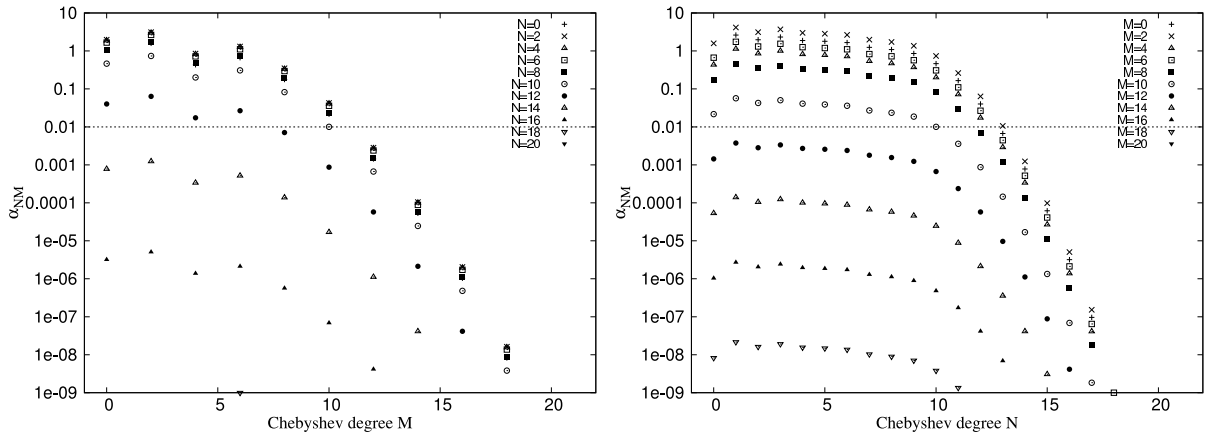


Figure 5.6 Chebyshev spectral coefficients for the mode $m = 2$, $n_1 = 7$ and $n_2 = 2$ in a power-law model with $\beta = 1.5$. This is to be compared to Figs. 5.3-5.4 of the same mode but in a polytrope model ($p = k\rho^{5/3}$). Frequency of the mode in this case is $\mu = 0.343$. Left panel: horizontal axis is degree M and different symbols stand for different N degrees. Right panel: N and M are swapped. The spectral coefficients appear to drop to zero beyond certain Chebyshev degrees. The expansion to a finite truncation is complete. This is related to the fact that solutions to the ordinary differential equations for inertial modes in power-law profile in a polynomial (with finite degrees). Such a clean behaviour is not expected in the polytrope case where coupling between different Chebyshev degrees continues the spectrum to infinity (though the coefficients fall off with spectral degree).

expanding the wavefunction as a sum of spherical harmonics in the spherical angles, and then expand the radial direction as Chebyshev polynomials (Dintrans and Ouyed 2001), as power-laws (Lockitch and Friedman 1999), or directly integrated in the resulting ODEs (Yoshida and Lee 2000; Lee et al. 1992b). While Dintrans and Ouyed (2001); Iper and Lindblom (1990) have used an iterative spectral solver which allows them to go to spherical harmonics as high in degree as 20 or 40, most other codes can only accommodate low ℓ expansions and thus is suitable only for finding inertial modes of the lowest orders. For instance, while Yoshida and Lee (2000) included the centrifugal force as perturbation to the background state, they expanded the eigenfunction in spherical harmonics only up to degree 6, where they agree in the eigenfrequency results. When using such an expansion in higher order inertial modes, one would find that spherical harmonics series

expansion do not converge well with the limited truncation (Lee et al. 1992b).

Since most previous studies are motivated by finding low order inertial modes that are either subject to gravitational radiation instability or can be directly detected on the surface of giant planets, their approaches are reasonable. However, for our tidal problem at hand, we need to find modes to as high order as possible, and (as shown in the next section), as accurately as possible. These goals call for a different PDE solver. We believe our adoption of Chebyshev expansion in ellipsoidal coordinates furnish us with just the requisite tool. We find convergence with a lower truncation than those using spherical harmonics.

We produce two comments here.

For non-rotating spheres, internal oscillation modes are trivially labeled by three quantum numbers, (n, ℓ, m) , where n is the number of radial nodes and ℓ, m are associated with the particular spherical harmonics used to describe the mode. Such an easy typing has proved convenient for studying eigenfrequency dependence on models, inter-comparison between codes, and asteroseismology. However, such a labeling scheme for inertial modes has been lacking. For example, lack of a good alternative, (Dintrans and Ouyed 2001) introduced viscosity to the momentum equation to separate the few lowest modes from a dense spectrum of inertial modes. We propose to solve this problem by adopting the ellipsoidal coordinates. Labeling of the mode in any density profile is simply (m, n_1, n_2) , where n_i is the number of nodes in the x_i coordinates, and m the usual azimuthal number.

We also compare our results against those obtained by Papaloizou and Ivanov (2005) using an expansion in the spherical coordinates. They showed the same inertial mode as that in our Fig. 5.5, their figure is reproduced in Fig. 5.7. The advantage of the ellipsoidal coordinates becomes obvious as one compares the two figures. A clean, converged eigenfunction is essential for computing accurately the interaction between inertial modes and the tidal potential (next section).

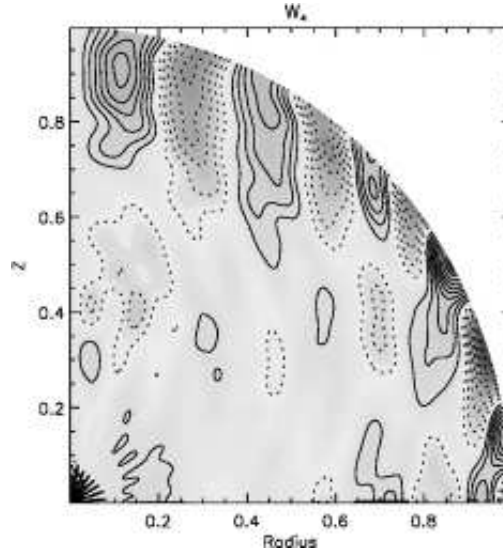


Figure 5.7 An identical eigenmode as that in Figure 5.5, but obtained by Papaloizou and Ivanov (2005) using a polynomial expansion in the spherical coordinates. Convergence of the series is poorer and the resultant eigenfunction much noisier.

5.3 Tidal Overlap Integrals and Implications on Tidal Damping

Now that we have obtained satisfactory inertial mode eigenfunctions for polytrope models, we proceed to calculate the tidal overlap integral. The tidal overlap would have been trivial to calculate if not for the many reversals of the inertial modes inside the planet, which causes severe cancellation (Wu 2005b). In fact, Goodman and Lackner (2009) argued that inertial modes do not couple to the smoothly varying tidal potential at all, lacking an evanescent region in which coupling occurs (as in the case of gravity-modes). We contest against their assertion in chapter 7.

So as is shown in Wu (2005b), the useful parameter that quantifies the tidal coupling is the following normalized tidal overlap integral, C_n ,

$$C_n = \frac{\left| \int \delta\Phi_{\text{tide}} \frac{\omega^2 \rho}{c_s^2} \psi d^3r \right|}{\int \left| \delta\Phi_{\text{tide}} \frac{\omega^2 \rho}{c_s^2} \psi \right| d^3r}, \quad (5.3.1)$$

which measures how severely the cancellation effect is. The subscript $n = (n_1 + n_2)$

indicates that we are studying the dependence on n at a fixed μ .

Taking the $\ell = m = 2$ tidal potential, $\delta\Phi_{\text{tide}} \propto r^2 P_2^2(\theta, \phi)$, transforming the above integral into the ellipsoidal coordinates, and integrating away analytically the azimuthal angle ϕ , we obtain,

$$C_n = \frac{\left| \int_{\mu}^1 \int_{-\mu}^{\mu} (1-x_1^2)(1-x_2^2) \frac{\rho}{c_s^2} \psi \, dx_1 \, dx_2 \right|}{\int_{\mu}^1 \int_{-\mu}^{\mu} \left| (1-x_1^2)(1-x_2^2) \frac{\rho}{c_s^2} \psi \right| \, dx_1 \, dx_2}. \quad (5.3.2)$$

Since only the modes that are symmetric with respect to the equator have non-zero tidal overlap, the range of integration for x_2 can be reduced to $(0, \mu)$.

The results for C_n are shown in Figure 5.8. The oscillating integrand can be tricky to integrate, especially in 2-D. Large cancellations between different patches inside the planet can lead to non-convergent results. Numerically, we integrate first along the x_1 direction using the Romberg (Press et al. 1992) approximation (a variation of the trapezoidal rule), then integrate along the x_2 direction with 1000 grid points.

The polytrope model yields comparable values for C_n as those from a similarly valued power-law model (Wu 2005b). This is perhaps not un-expected. Equation (2.2.16) shows that, for an arbitrary but smooth density profile that deviates slightly from a power-law one, the eigenfunction (transformed in eq. 2.2.15) satisfies roughly the same differential equation, barring some (non-separable) terms that are second order in wavevector. So there should be strong similarity between eigenfunctions in $n_{\text{poly}} = 1.5$ and $\beta = 1.5$ cases, as is demonstrated by comparing spectral coefficients in Fig. 5.3 ($n_{\text{poly}} = 1.5$) and Fig. 5.6 ($\beta = 1.5$).

We study the roles of individual Chebyshev spectral components by substituting $\psi = T_N(t_1)T_M(t_2)$ into equation (5.3.2),

$$C_{NM} = \frac{\left| \int_{\mu}^1 \int_{-\mu}^{\mu} (1-x_1^2)(1-x_2^2) \frac{\rho}{c_s^2} T_N(t_1)T_M(t_2) \, dx_1 \, dx_2 \right|}{\int_{\mu}^1 \int_{-\mu}^{\mu} \left| (1-x_1^2)(1-x_2^2) \frac{\rho}{c_s^2} T_N(t_1)T_M(t_2) \right| \, dx_1 \, dx_2}. \quad (5.3.3)$$

The results for C_{NM} are presented in Fig. 5.9.

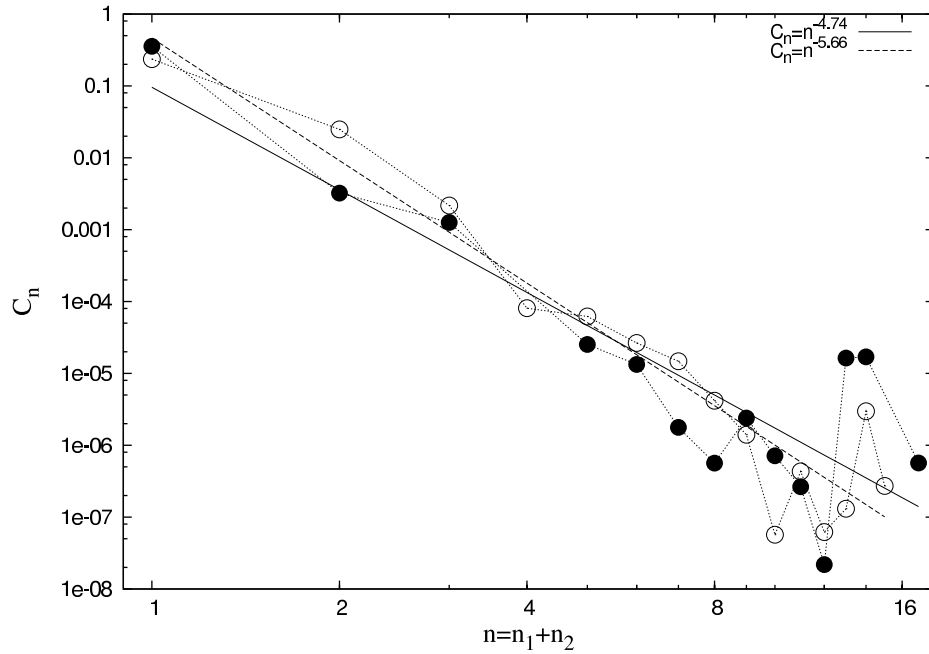


Figure 5.8 The relative tidal overlap integral C_n for a polytrope of $p = k\rho^{5/3}$ ($n_{\text{poly}} = 1.5$, solid circles), plotted here as a function of $n = n_1 + n_2$. For comparison we also show C_n for a power-law density structure of index $\beta = 1.5$ (open circles).

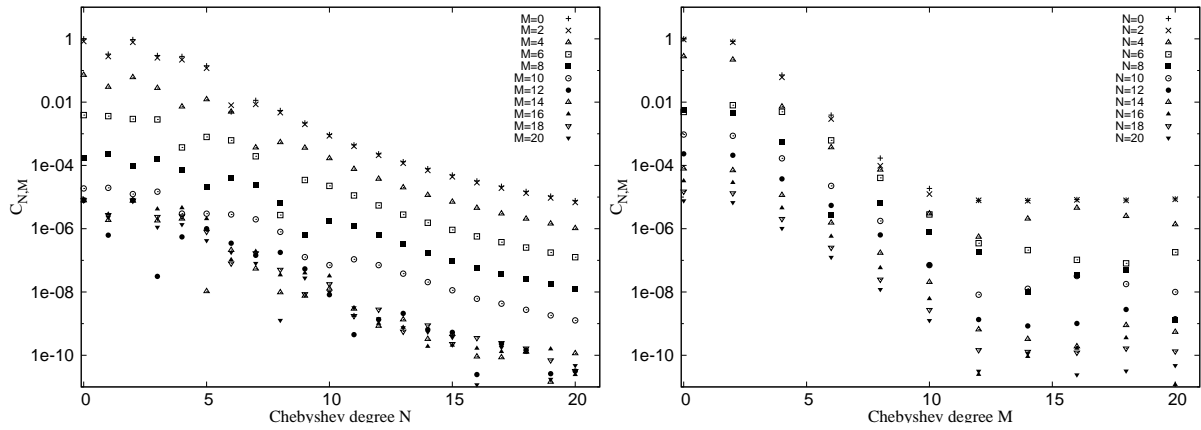


Figure 5.9 Tidal overlap integral for each 2-D Chebyshev spectral component, $T_N(t_1)T_M(t_2)$ for the polytrope model $p = k\rho^{5/3}$. Left panel shows the dependence on degree N with different M degree values represented by different symbols; right panel plots degree M as the horizontal axis.

As expected, C_{NM} falls off with degrees N and M , roughly as power-laws. Higher degree terms have more oscillations and suffer stronger cancellations. As a result, for

a given inertial mode, higher degree terms contribute negligibly in comparison to lower degree terms to the overlap integral. As a result, if we want an accuracy in C_n of order 10^{-6} , we would need a comparable accuracy in, say, $\alpha_{1,0}$, but much lower accuracies in the higher degree coefficients, e.g., 10% in $\alpha_{20,0}$ and of order unity in $\alpha_{20,2}$.

This result also justifies the convergence criterion we enforce when looking for inertial modes: we only ask eq. 5.1.9 to be satisfied for large, low degree coefficients.

A 2-D numerical integrator is more prone to numerical errors than a 1-D one. This is also demonstrated in Figure 5.9. Though one expects that the higher the Chebyshev degree the smaller C_{NM} is, it reaches a floor value of 10^{-5} for $M \rightarrow 20$ and $N = 0, 2, 4$.

In summary, similarity in C_n between the polytrope and the power-law models lead us to conclude that the tidal Q value for the polytropic case is also of the same order of magnitude as that calculated using the power-law model (Wu 2005b). At $Q \sim 10^9$, this is some 2-3 orders of magnitude below the inferred value for Jupiter and hot jupiters.

5.4 Possible Improvements

Here we propose some possibilities for improvement in our inertial mode finding algorithm.

Dintrans and Ouyed (2001) exerted an artificial damping in the equation of motion in order to separate the low order modes from the high order modes. While their purpose is to identify modes and we have no such needs here, the same strategy may be used to remove spurious modes in the pseudo-spectral method. For instance, in Fig. 5.1, at high enough truncations, one observe a lot of minima in the determinant. If one is aiming at looking for some low to intermediate order modes, one can avoid the distraction by spurious high order modes (which are not properly resolved at the given truncation) by damping them away.

When one is interested in looking for high order modes, however, perhaps a strategy

of using the following sideband truncation (Boyd 2001) may prove useful,

$$g(t_1, t_2) = \sum_{N=N_{\min}}^{N_{\max}} \sum_{M=M_{\min}}^{M_{\max}} \alpha_{NM} T_N(t_1) T_M(t_2). \quad (5.4.1)$$

Truncated at both high end and at the low end, this may remove low order modes from polluting the spectrum of higher order modes.

In our truncation of Chebyshev series, we use the ‘square truncation’, namely, truncate whenever $N > N_{\max}$ or $M \geq M_{\max}$ with $N_{\max} = M_{\max}$. This, according to Boyd (2001) (page 119) is not fair. For example, the term $T_{10}(x_1)T_{10}(x_2)$ varies more rapidly than the term $T_{11}(x_1)T_0(x_2)$ and should be discarded when one is looking for a low order mode. Moreover, when we have eigenmodes with $n_1 \gg n_2$ or vice versa, a square truncation is not reasonable. One could experiment with a ‘ellipse’ truncation, where $\sqrt{(N/n_1)^2 + (M/n_2)^2} \leq I_{\max}$.

Where there are discontinuities in density or its gradient (as in the core/envelope border, or the putative plasma phase transition point), or discontinuities in equation of motion (as in the radiative-convective boundary), one can expand the wavefunction in different domains by different set of basis functions. Insisting on continuity across the domain boundary provides the needed constraints to close the system of equations (see p. 479 Boyd 2001). This so-called ‘spectral element method’ may be used to advantage in models where there is, e.g., a radiative envelope on top of a convection zone (hot jupiters), or vice versa (solar-type stars).

Ipsier and Lindblom (1990) described an iterative scheme to reach convergence of eigenfunction and eigenfrequency. This involves guessing initially a simple form for the eigenfunction ($\psi(r, \theta)$), then solve for its eigenfrequency using the variational principle, resubstitute the new eigenfrequency into the equation to obtain a more refined expression for the eigenfunction, and so on and so forth. They use this strategy to successfully obtain solutions of ‘ $\ell = m$ ’ f-modes in fast rotating stellar models, by using non-rotating solutions as initial guesses. An accuracy of 10^{-3} is reached after 5 – 10 iterations. This

is a worthy venue of improvement. We could look for the desired inertial mode taking the corresponding eigenfunctions in, say, the power-law density profile as an initial guess. The convergence should be rapid and more computationally economic.

Chapter 6

Density discontinuity inside Jupiter

Wu (2005b) suggested that a density discontinuity inside Jupiter may generate a greater tidal response. At the same time she did not expect that the solutions for the inertial mode eigenfunction would change significantly when a discontinuity is introduced as inertial modes are insensitive to the density structure, therefore the only quantity sensitive to the structure was the tidal overlap integral itself (explicitly dependent of the sound speed and the density).

Our current knowledge for the equation of state in giant planets is incomplete. Both *ab initio* calculations and high pressure lab experiments suggest that under high pressure, molecular hydrogen transitions into metallic hydrogen (Saumon et al. 1995). This occurs at $\sim 80\%$ radius for Jupiter. The nature of the phase transition is uncertain and it could be first order in which case density undergoes a finite jump.

Guillot (1999) produced two models that we planned to study. Model D has a first order phase transition, and it is of the order of 10% in density, and model B has a second order phase transition with a density gradient varying about 50%.

Enlightening for our studies is the work of Ivanov and Papaloizou (2007), who studied how the inertial mode eigenfunctions were modified by a density jump. In their model they expanded the solutions as a summation of radial functions times associated Legendre

polynomials. Then they forced this solution to run across the discontinuity and found that convergence was very poor. Their aim was the problem of tidal capture of highly eccentric objects, where the interaction was only reduced to a fly by of the planet near the periastron. Highly accurate eigenfunctions were not needed, and at the same time only few low-order ‘global’ modes were important when the tidal interaction is reduced to the interaction at that location.

In the case of a permanent tidal forcing, we looked for a similar solution, using what we call a ‘brute-force’ method, where we propose and expand the eigenfunction exactly in the same way we did for the polytropic case. As the reader can see in section 5, the only term that is sensitive to the density structure is $X = (1 - r^2)^\beta/\rho$ throughout its derivative $d \ln X/d \ln t$.

6.1 Technical problems

Soon after we tried this approach, we experienced problems finding convergence in the coefficients at consecutive truncations, even for the low order modes. One would expect that, since the wavelength of low order modes are much larger than the actual discontinuity thickness or $\lambda \gg \Delta r/R = 10^{-6}$ for Jupiter D model, and $\Delta r/R = 10^{-3}$ for the FWHM of the B model where the density jump is of second order.

We can understand the lack of convergence as non-negligible contribution of high degree Chebyshev polynomials while trying to map the density jump. This is a common problem when one tries, for example, to expand a step-function wave (square wave) in terms of Fourier series. The more degrees one adds, the worse the sampling near the discontinuity. This effect is known as the ‘Gibbs phenomenon’ (Arfken and Weber 2005).

The net effect is then the existence of non-negligible high-degree spectral coefficients, and therefore a failure to satisfy the criteria, yielding different non-convergent values of overlap integrals, especially when cancellation is expected to be large.

A technical problem related to the above is the inaccuracy in the Jupiter numerical models, that may present themselves as small, but finite, density jumps and may also contribute to inaccurate determination of C_n for large n (Wu 2005b), when the cancellation effects become strong. We do not expect to find numerically exact eigenmodes (coefficients) and C_n at large n , as for those cases high truncation in the expansion would contribute to many sources of pollution in our frequency root-finding algorithm¹. However the order of magnitude of C_n is important in order to define a scaling of C_n as a function of n . This scaling is important, as Wu (2005b) found that modes around $n = n_1 + n_2 \sim 30$ are the most relevant for tidal dissipation: these resulted from a balance between cancellation in the overlap integral, damping and likelihood of resonance driven by the tidal disturbing object (host star). As Wu (2005b) showed, the energy dissipated per orbit is proportional to C_n^2 and therefore Q is inversely proportional to it (e.g. see equation 1.1.1).

In order to avoid numerical inaccuracies of realistic Jupiter models, we studied a toy model. We used a density profile that is a disturbance to the analytical power-law density profile. This disturbance is included in order to generate a parametrized and controlled density jump. We also allocated the density jump along one of the ellipsoidal coordinate axis as we wanted to understand how the geometry may affect the way in which high order modes are transmitted and reflected.

The test density profile is defined in the ellipsoidal coordinate system $x_1 \in [\mu, 1]$, $x_2 \in [-\mu, \mu]$ as:

$$\rho = [1 + \Lambda\{-\tanh((x_1 - x_{1c})/\Delta) + 1\}] \times (1 - r^2)^\beta, \quad (6.1.1)$$

where x_{1c} is the center of the jump, Δ is proportional to the width of the jump, and Λ is the amplitude of the jump.

Figure 6.1 shows how the jump looks like in the ellipsoidal and meridional planes.

¹We also expect that, for high order modes, the computing times become quite demanding, as the size of the pseudo-spectral matrix increases.

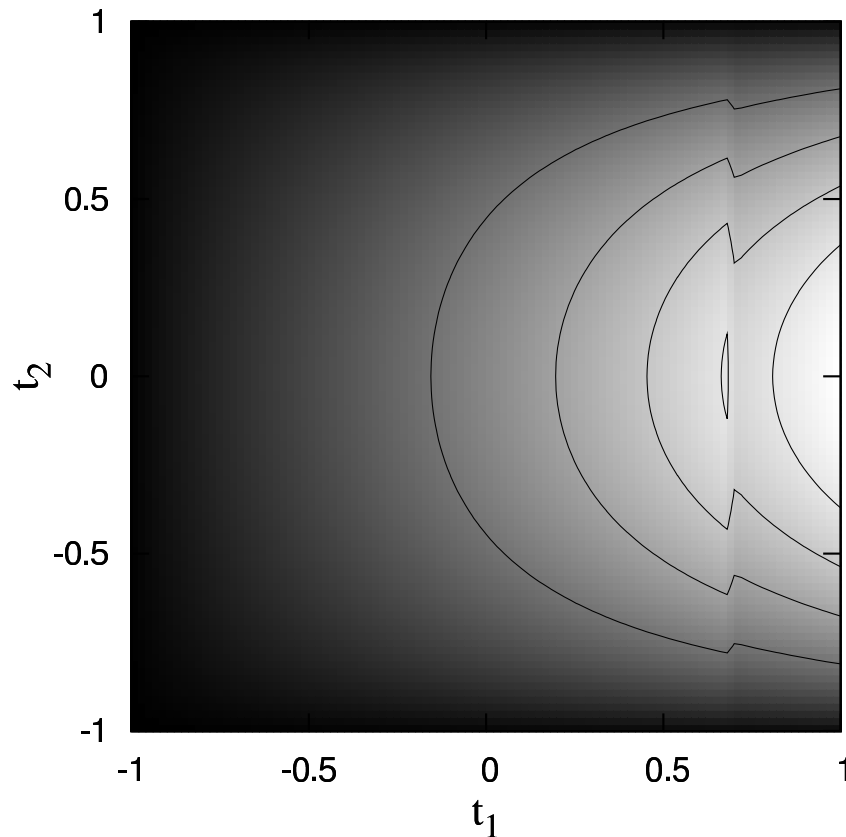


Figure 6.1 Test density profile in the Chebyshev space for the mode $m = 2$, $n_1 = 7$, $n_2 = 2$, and $\mu \sim 0.343$. The jump is located at $t_1(x_1 = 0.9) \sim 0.7$, has a width of $\Delta = 10^{-3}$, and an amplitude of $\Lambda = 10^{-1}$.

We expect that when $\Lambda = 0$ (and Δ is finite) we should recover the eigenmodes for the power-law density profile (Figure 5.6) of index β . We then study the convergence of the Chebyshev coefficients when different values of Δ and Λ are used, specifically, values that closely resemble realistic density profiles that include a phase transition.

Here we present results based on the same medium-order mode $n_1 = 7$, $n_2 = 2$, $m = 2$ that we have been using to illustrate convergence in the coefficients for smooth density profiles.

For values of $\Lambda < 10^{-1}$ and $\Lambda < 10^{-3}$ convergence above the threshold is achieved at the usual truncation found using the spectral method $N_{max} = l - |m| = 2(n_1 + n_2)$, but the coefficients below the threshold become larger in magnitude compared to the power law case. Convergence in the eigenfrequency is also achieved, and the value remains the same as in the power law case. Figures 6.2 and 6.3 reflect these results.

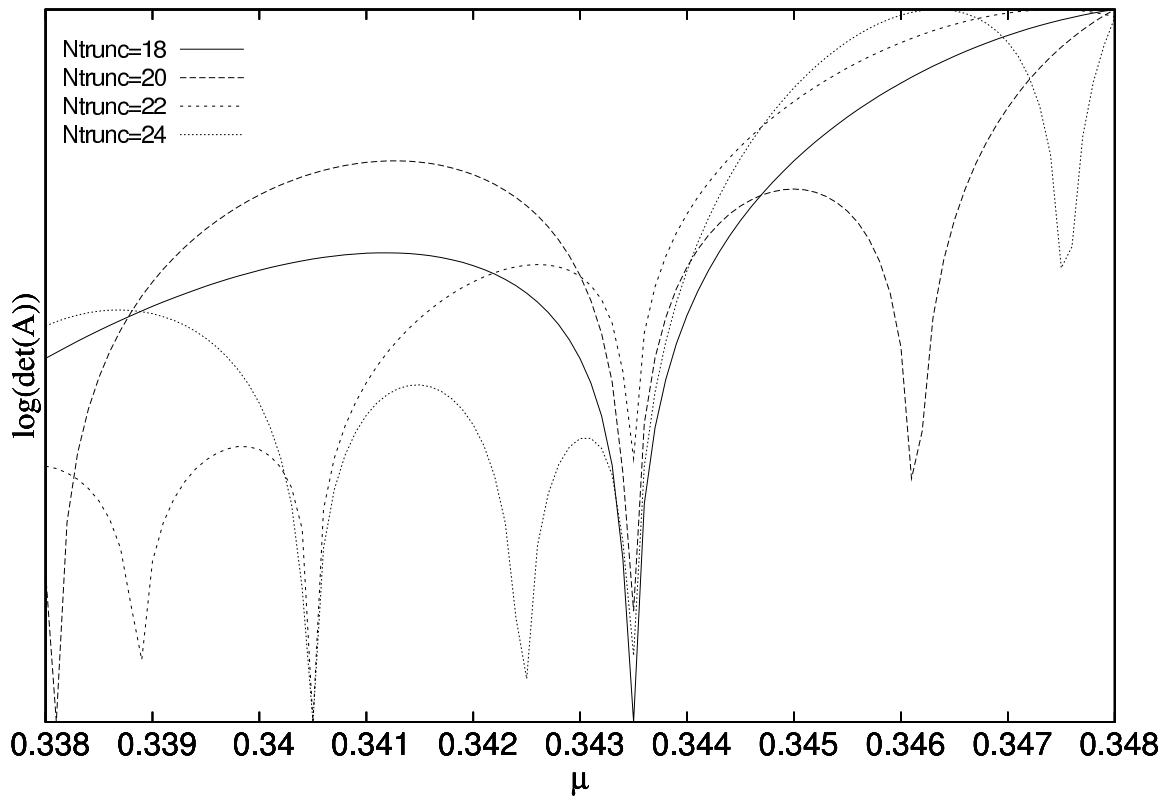


Figure 6.2 A mode scan similar to Figure 5.2, this time for a different mode in a ‘test’ density profile of width of $\Delta = 10^{-3}$, and an amplitude of $\Lambda = 10^{-3}$. Here we normalize the value of $\log \det\{A\}$ in order to show that, for a specific eigenmode, the eigenfrequency of the minima stays at the same location, showing convergence. The mode we show here, highlighted by thick sections is $m = 2$, $n_1 = 7$, $n_2 = 2$ and $\mu = 0.3434800519$.

However for a test density profile that has a width of $\Delta = 10^{-1}$, and an amplitude of $\Lambda = 10^{-2}$, as shown in figure 6.1 we start finding convergence problems, this is evident when we look at how the spectral coefficients change as the truncation changes.

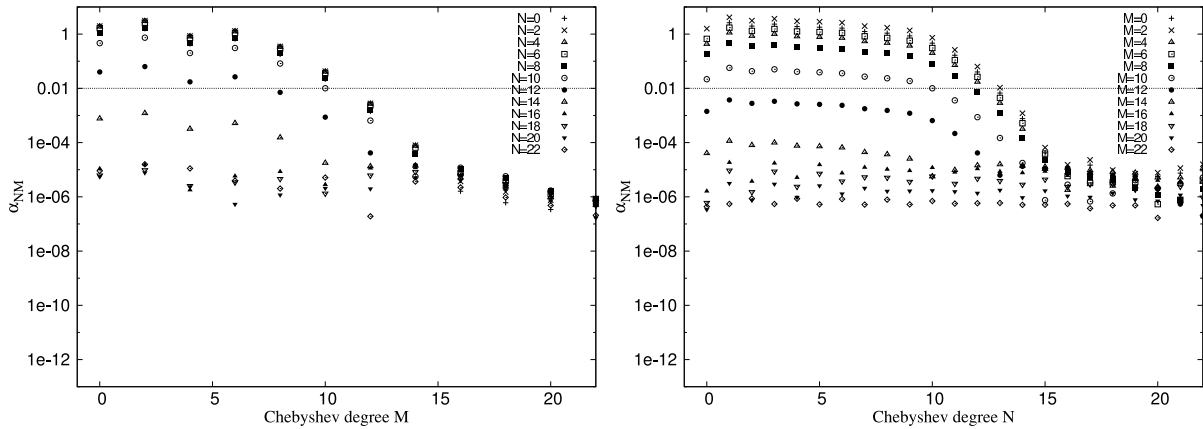


Figure 6.3 Mode $n_1 = 7$, $n_2 = 2$, $m = 2$, and $\mu = 0.3434800519$ when a test density profile is used. The test density profile has a width of $\Delta = 10^{-3}$, and an amplitude of $\Lambda = 10^{-3}$. Compare these coefficients with the ones calculated for the power-law case in Figure 5.6. Above the threshold line, all the coefficients converge for consecutive truncations, and have fractional error of $\epsilon = 0.01$ with previous truncation, and with the mode when the power-law density profile remains undisturbed. The difference in frequency μ of this mode with the power-law mode is negligible (fractional error smaller than 10^{-8}). The truncation at which this mode starts to converge is two Chebyshev degrees higher ($N_{max} = 20$) than in the power-law case ($N_{max} = 18$).

This effect can also be seen when we search for this mode in a plot $|A(\mu)|$ vs μ for consecutive truncations. The minima oscillates and does not remains steady near the power-law value of $\mu = 0.3434800519$.

The spectral coefficients show poor convergence, higher degrees begin to dominate.

As the previous tests show, the ‘brute-force’ approach may not adequate in order to find convergent inertial modes when there is a density jump in the planet. And since we can not rely on the eigenmode we can not rely on C_n .

We may speculate that the lack of a solution for inertial modes when a density discontinuity is included, may be a sign of partial internal reflection, that needs to be addressed as it could alter the tidal response in a significant way.

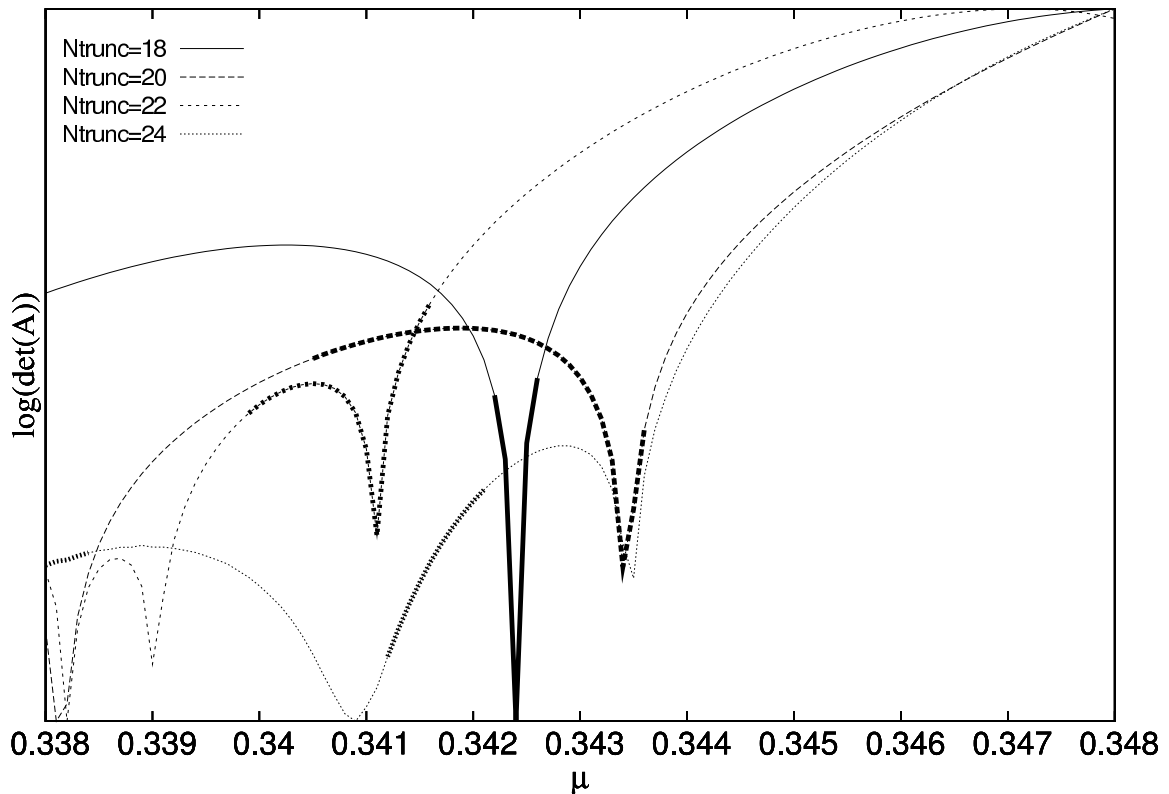


Figure 6.4 A mode scan similar to Figure 6.2 for the he test density profile of width of $\Delta = 10^{-1}$, and an amplitude of $\Lambda = 10^{-2}$. Here we normalize the value of $\log \det\{A\}$ in order to show that, for a specific eigenmode, the eigenfrequency of the minima oscillates for different truncations. The mode we show here, highlighted by thick sections is $m = 2$, $n_1 = 7$, $n_2 = 2$. Outside the thick sections, our node counter finds different modes with larger or smaller values of n_1 and n_2 .

6.1.1 1-d confined sound waves

Because of the possibility that a large set of Chebyshev polynomials may be needed in order to map the discontinuity, we can not conclude that the lack of convergence of the spectral coefficients under the presence of density jumps has the physical explanation of partial reflection (or perhaps ergodic waves).

In order to numerically simplify the problem and understand the technicalities of the pseudo-spectral method, we studied a 1-d sound wave problem, where the wave equation

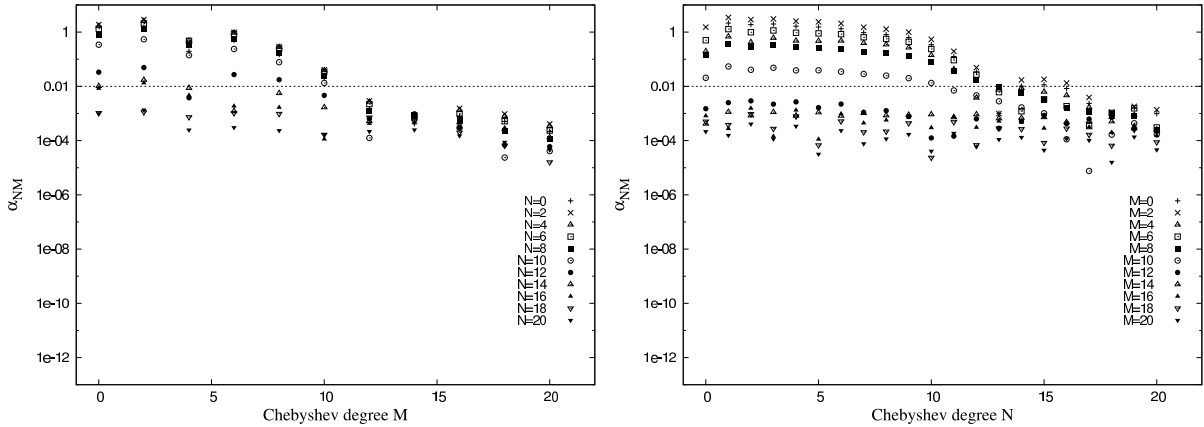


Figure 6.5 Mode $n_1 = 7$, $n_2 = 2$, $m = 2$, and $\mu = 0.3410845798$ when a test density profile is used. The test density profile has a width of $\Delta = 10^{-1}$, and an amplitude of $\Lambda = 10^{-2}$. Compare these coefficients with the ones calculated for the power-law case in Figure 5.6. Above the threshold line, all the coefficients will not converge for consecutive truncations, since they have fractional errors above $\epsilon = 0.01$. The truncation used for this mode is $N_{max} = 22$ whereas in the power-law case is $N_{max} = 18$.

resembles the full² inertial mode equation (2.1.20).

The equation to solve is:

$$c_s^2 \frac{d^2 \psi_k}{dx^2} = \omega^2 \psi_k, \quad (6.1.2)$$

where ψ is the eigenfunction, ω the eigenfrequency, and c_s is the sound speed. The boundary conditions satisfy $\psi(x = 0) = \psi(x = 1) = 0$. For exploratory reasons we use a sound speed that is a constant plus a small Gaussian function:

$$c_s = c_{s0} \left(1 + \frac{\Lambda}{\delta x \sqrt{\pi}} e^{-\left(\frac{x-x_0}{\delta x}\right)^2} \right). \quad (6.1.3)$$

Where c_{s0} is a constant (set to be 1), Λ sets the amplitude in the same way it did in equation (6.1.1), δx is the spread of the Gaussian function which is proportional to the FWHM, and x_0 is the center of the Gaussian.

This function behaves like a constant in most of the interval $x \in [0, 1]$, however, near x_0 it behaves as a Gaussian peak³. This function resembles the equation for the

²As we mentioned in section 2.1 we neglect the sound speed term.

³In fact, in the limit $\delta x \rightarrow \infty$, the sound speed, as defined, is exactly a constant plus a Dirac delta at x_0 .

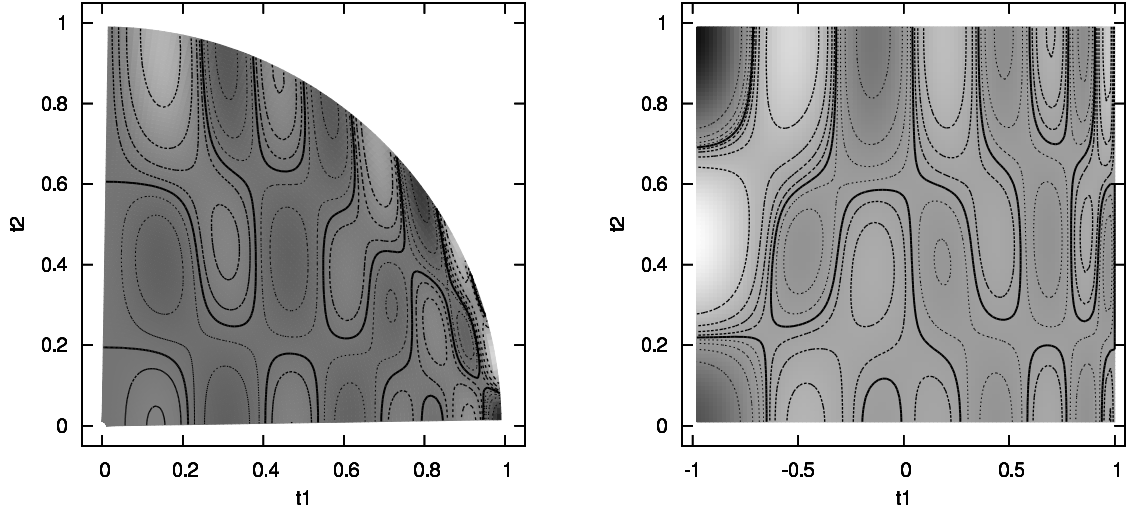


Figure 6.6 A meridional cut for an even eigenfunction with quantum numbers $m = 2, n_1 = 7, n_2 = 2$, and eigenfrequency $\mu = 0.351$ in the test model with $\beta = 1.5, \Lambda = 10^{-1}$ and $\Delta = 10^{-2}$. Left panel: amplitudes for Eulerian density fluctuation plotted in spherical coordinates, with dark patches (light gray dots) being positive values and lighter patches (solid black dots) negative values. Right Panel: the same quantity now projected in ellipsoidal coordinates. The (t_1, t_2) coordinates are linearly morphed from the original (x_1, x_2) coordinates (eq. 3.1.3). Pay attention to the feature that now the nodal lines do not run parallel to constant coordinate lines.

density jump (6.1.1), since the logarithm of the density gradient appears explicitly on the inertial mode equation (2.1.20) as H . In the case of an inertial mode where the density is a power-law plus a jump (equation 6.1.1), H^{-1} behaves just like c_s^2 does in this toy model.

In order to solve equation (6.1.1), we use the same Chebyshev pseudo-spectral technique that we have been using to solve the inertial mode equation. This means that we have to map the interval $x \in [0, 1]$ to the Chebyshev interval $t \in [-1, 1]$, and then, expand the eigenfunction as $\psi_k = \sum_{n=0}^{N_{trunc}} \alpha_N T_N(t)$. Also, in order simplify this experiment, we fix $\Lambda = \delta x$.

As a first attempt to study this problem, we aim to find eigenfunctions for the lowest

order sound wave, $n = 0$. We test two different FWHMs: $\delta x = 0.1$ and $\delta x = 0.01$. Figure 6.7 shows that the eigenfunction of this mode is barely affected by the jump, since its wavelength is large compared to the size of the jump. In Figure 6.8 we show fast convergence of the spectral coefficients; for the case of $\delta x = 0.1$ it seems that Chebyshev degrees of index larger than $N = 100$ do not contribute significantly to the eigenfunction. For $\delta x = 0.01$ it seems that only degrees of $N < 1000$ are important. This illustrates the slow convergence of the pseudo-spectral coefficients when density jumps are present, at the same time the physics of the problem becomes clear, the mode exists, it is not affected by the jump and the solutions are convergent. The frequency is affected when comparing different FWHM, but also converges when comparing different truncations.

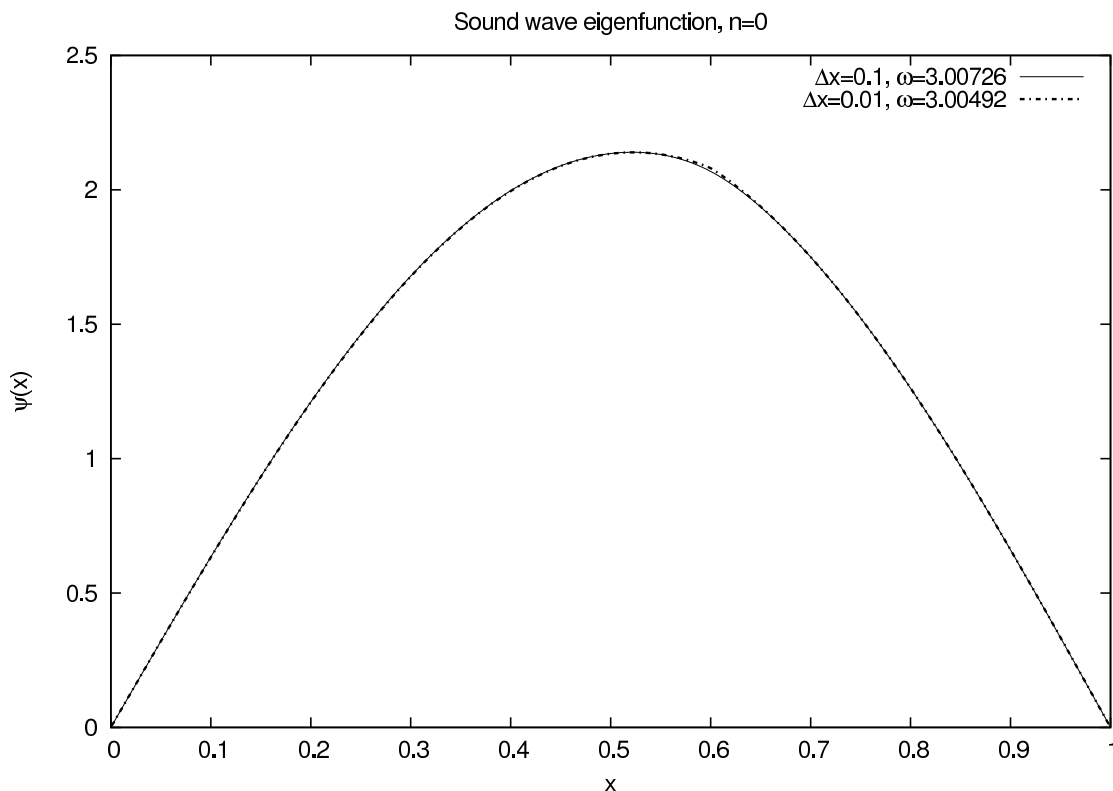


Figure 6.7 The eigenfunctions of the mode $n = 0$ (zero nodes inside the region $0 < x < 1$) for FWHMs $\delta x = 0.1$ and $\delta x = 0.01$. The differences are almost negligible.

Secondly we study the effect of the jump on a higher-order mode, $n = 48$ for two different FWHMs: $\delta x = 0.1$ and $\delta x = 0.01$. As in the previous case, we found that

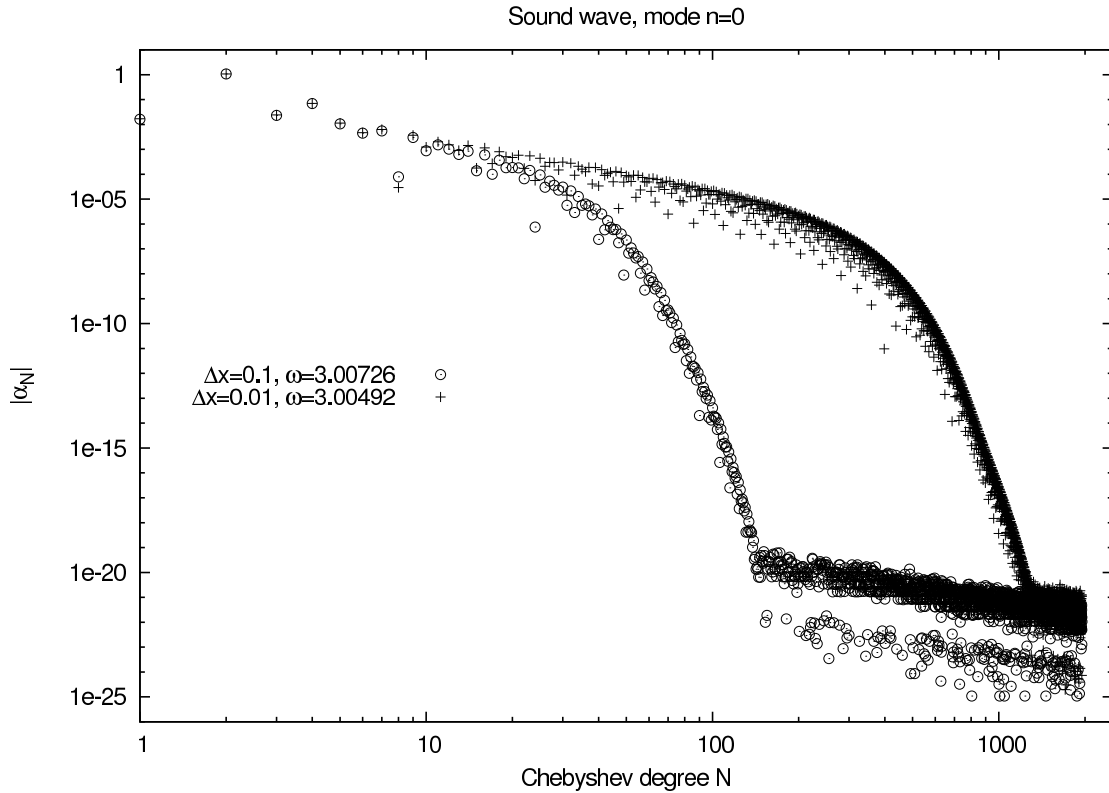


Figure 6.8 The spectral coefficients of the mode $n = 0$ for FWHMs $\delta x = 0.1$ and $\delta x = 0.01$. Here we can clearly see the effect of the jump. While the eigenfunctions and eigenfrequencies are not significantly affected, the convergence of the coefficients becomes slower when we reduce the size of the FWHM of the jump, in this case is by almost an order of magnitude.

convergence of the spectral coefficients depends on the FWHMs, roughly at the same truncations as in the previous case. The convergence implies that the mode exists, and its accuracy only depends on the truncation of the series. This mode in particular, crosses the jump modifying its local amplitude and wavelength. Effect that is expected as the mode wavelength is comparable to the FWHM of the jump. Figure 6.7 shows the different shape of mode $n = 48$ for the two different FWHMs.

The 1-d sound wave problem allowed us to understand the 2-d inertial mode solutions. We expect spectral convergence, i.e., inertial mode existence, once we allow enough Chebyshev degrees to describe the eigenfunction, or, in other words, increase the truncation.

The pseudospectral method seems to work quite well for smooth density profiles, but

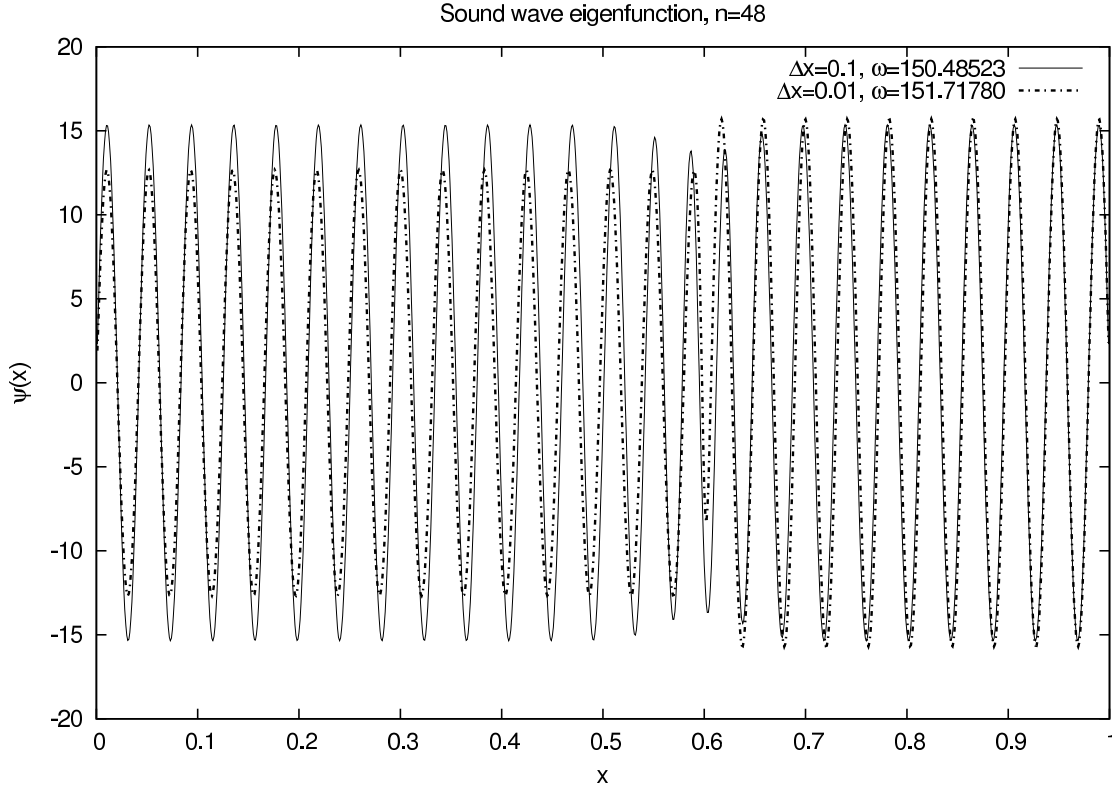


Figure 6.9 The eigenfunctions of the mode $n = 48$ (48 nodes inside the region $0 < x < 1$) for FWHMs $\delta x = 0.1$ and $\delta x = 0.01$. This time, the difference is significant across the jump.

it presents many problems when there are density discontinuities. One way to avoid the effect of the density jump, is to define a functional form in the region that surrounds and includes the density jump. One can figure out boundary conditions for the functional form of the solution at every side of the density jump.

Lee et al. (1992a) also investigated how inertial modes are affected by core-envelope boundary, as well as the presence of a phase transition that involves a density discontinuity. They found that three inertial cavities are produced, and there are modes trapped in each of the cavity as well as interface modes (modes that are concentrated in the density jumps).

They have calculated low order inertial modes inside Jupiter.

‘Free-slip’ boundary conditions are applied at the corresponding interfaces. This imply:

$$\delta p|_{-}^{+} = 0, \quad \xi_r|_{-}^{+} = 0, \quad (6.1.4)$$

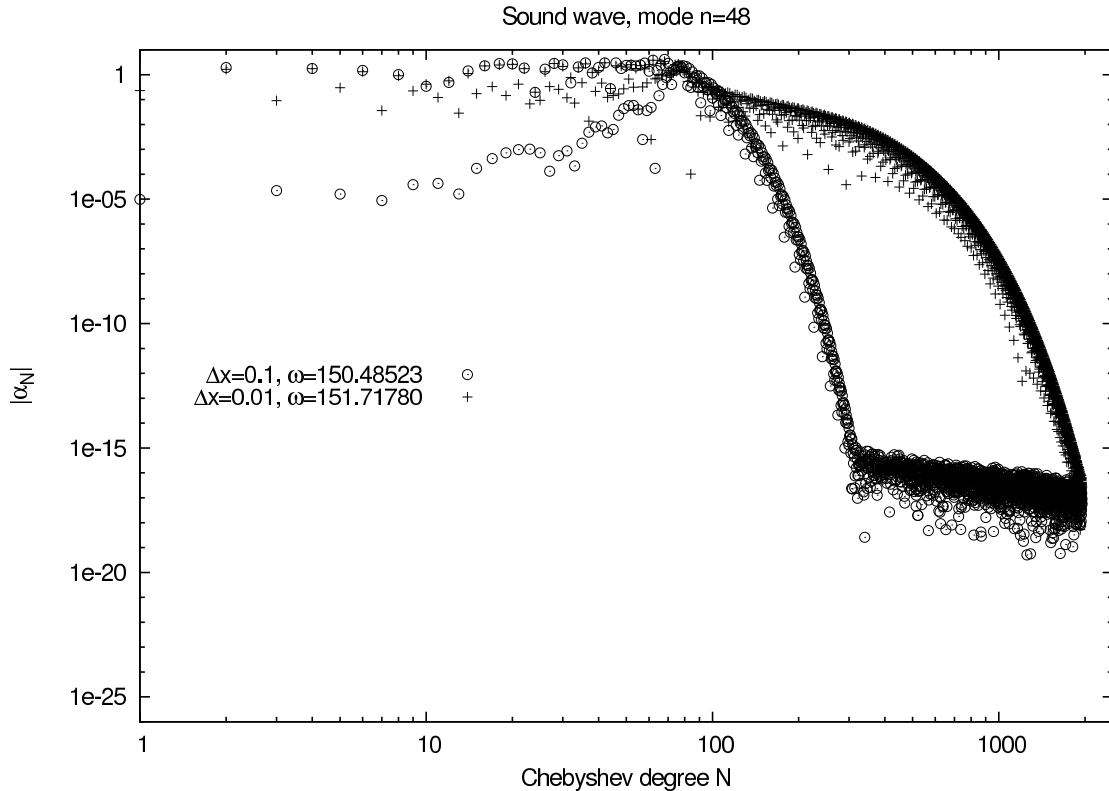


Figure 6.10 The spectral coefficients of the mode $n = 48$ for FWHMs $\delta x = 0.1$ and $\delta x = 0.01$. Here we also can see the effect of the jump. The convergence of the coefficients becomes slower when we reduce the size of the FWHM of the jump, in this case is by almost an order of magnitude.

where the ‘ \pm ’ symbols denote evaluations at the low and upper boundaries. Significantly differences were found for Jupiter models with and without PPT (Plasma phase transition). Therefore an obvious next step for our work, is to include the region around the jump in a explicit form in the equation of motion, or by introducing a new set of boundary conditions surrounding the jump.

6.2 The presence of a solid core

In the entire thesis work we have assumed that there is no solid core inside Jupiter and hot-Jupiters, and that these objects are entirely convective. Current planetary models (Saumon et al. 1995; Saumon and Guillot 2004) predict a rocky core in Jupiter of less than $8 M_{\oplus}$, but more recent calculations have shown that the core size could eventually

be larger, with masses around 14-18 M_{\oplus} (Militzer et al. 2008).

As we have seen, a density discontinuity is not straightforwardly treated by our pseudo-spectral method. Not only does it become difficult to find convergence in the spectral coefficients, but the ellipsoidal coordinate system also fails to describe internal boundaries, as they can no longer be defined along constant ellipsoidal coordinate curves. Therefore the inclusion of a solid boundary could suppress the existence of inertial modes at all.

Ogilvie and Lin (2004) have found that, when the core is larger than $r_{core}/R_{planet} > 0.01$, free global inertial modes no longer exist, and the disturbances tend to be concentrated along wave attractors, i.e., regions inside the planet where the characteristic rays tend to be concentrated. They have argued that the tidal quality factor Q , does not depend on the viscosity, and that inertial modes can provide an efficient mechanism for tidal dissipation.

It remains a challenge to include a core in our formalism, low-order global inertial modes can still exist if the core is small. The study of the effect of the density discontinuity when a PPT exist can lead us to find a way to include a core in our formalism.

6.3 Future work

The 1-D sound wave model shows that increasing the spectral resolution produce convergence in the spectral coefficients and therefore improve the reliability of the eigenfunctions, crucial for the calculation of the overlap integrals. For the 2-D inertial mode problem, a discontinuity located parallel to one of the ellipsoidal coordinates axes, may allow convergence in the spectral coefficients if a large (time-consuming) spectral resolution is used.

However, more research is needed in the case of a discontinuity located at a fixed spherical radius, it is not obvious that a very high spectral resolution may produce highly

accurate inertial modes. It is possible that this is the case in which standing waves are not possible and only ergodic waves are allowed, as studies of free inertial waves, by Ogilvie and Lin (2004) suggest.

Chapter 7

The Effect of The Compressional Term – Response to Goodman and Lackner (2009)

Goodman and Lackner (2009) is a good read in the subject area of dynamical tides for rotating bodies. They first discussed uniform density models under a tidal forcing which is a polynomial of degree 2 in the Cartesian coordinates. The solution to the wavefunction ψ is also a polynomial of the same degree and there is no wave-like response. The lack of short wavelength dynamical tide in this model indicates that tidal dissipation must be highly ineffective¹.

After discussing in detail the response of a uniform density model with a central high density core, and showing that the response can be rather complicated and ray-like, Goodman and Lackner (2009) went on to calculate the tidal response of a power-law density model but keeping the compressional term in the boundary condition where it can be important. For a particular toy model they chose, they concluded that the wave-like tidal response is again absent. As a result, they concluded that tidal dissipation

¹While agreeing with the final conclusion, Wu (2005b) obtained it by showing that short-wavelength free oscillations do exist in the planet, however they do not couple to the tidal potential.

in a coreless isentropic body is very weak. And they suggested that the non-zero tidal response results in Wu (2005b) may be contaminated by the neglect of the sound speed term near the surface.

Here we follow their approach but instead conclude that inclusion of the compressional term does not alter conclusions made in Wu (2005b) that tidal response of a core less isentropic body is weak but non-zero.

We carry out this task in two steps. We first examine the particular toy model used in Goodman and Lackner (2009). We then go on to include the compressional term into our pseudo-spectral code and calculate the exact tidal response at the presence of finite compressibility.

7.1 Toy model of Goodman and Lackner (2009)

The approach taken by Wu (2005b) is the anelastic approximation where sound waves are filtered out as the oscillations are slow compared to the sound travel. Here, we retain the compressional term as is done in the toy model of Goodman and Lackner (2009). To solve for the tidal response analytically, we take a density $\rho \propto W^n$, pressure $p \propto W^{n+1}$, and $c_s^2 = W/n$, where W is the enthalpy and satisfies

$$W = (n + 1) \frac{P}{\rho} = W_0 (1 - r^2) = W_0 [1 - (x^2 + y^2 + z^2)]$$

with r being the dimensionless planetary radius and n the polytropic index. In particular, W_0 is related to the sound speed at $r = 0$ as $W_0 = nc_s^2(r = 0) = nc_{s0}^2$.

With such a setup, the density profile is identical to the power-law case with $\beta = n$. The pressure profile is not consistent with the mass distribution, but as has been argued (Wu 2005b; Goodman and Lackner 2009), this has little influence on the overall tidal overlap.

The Eulerian enthalpy perturbation is related to those of density and pressure as

$$W' = (n + 1) \left(\frac{P}{\rho} \right)' = (n + 1) \left(\frac{p'}{\rho} - \frac{\rho' p}{\rho \rho} \right). \quad (7.1.1)$$

We write $p'/p = (1 + 1/n)\rho'/\rho$ as the background state and the perturbations are both adiabatic. This yields,

$$\frac{W'}{W} = \frac{\rho'}{\rho}. \quad (7.1.2)$$

This allows us to rewrite the equations that govern the tidal response of the fluid as (Goodman and Lackner 2009)

$$\begin{aligned} -i\omega \mathbf{v} + 2\boldsymbol{\Omega} \times \mathbf{v} + \nabla W' &= -\nabla \Phi_{\text{tide}}, \\ -i\omega W' + \mathbf{v} \cdot \nabla W + \frac{1}{n} W \nabla \cdot \mathbf{v} &= 0. \end{aligned} \quad (7.1.3)$$

Goodman and Lackner (2009) proceeded to argue that as Φ_{tide} of concern is a polynomial of the form, say, $\Phi_{\text{tide}} \propto (x + iy)^2$, and similarly for the enthalpy, $W \propto [1 - (x^2 + y^2 + z^2)]$, there is a simple long-wavelength solution to the above equations as well as the boundary conditions. Goodman and Lackner (2009) drew the conclusion that if the sound speed term is properly included in the boundary condition, there should be no wave-like response excited by the smoothly varying tidal potential.

7.1.1 Tidal Overlap of Waves in the Toy Model

Here, we first compute the homogeneous solution to equations (7.1.3), having in mind that, in our description $W' = \psi$. This turns out fortuitously easy as both the PDE and the boundary conditions are separable in the ellipsoidal coordinates. We argue that the tidal response of the wave-like solution is comparable to that obtained ignoring compression.

We start from the full equation (7.1.4) describing adiabatic oscillations in isentropic, rotating planets,

$$\nabla^2 \psi - q^2 \frac{\partial^2 \psi}{\partial z^2} = \frac{1}{H} \left(\frac{\partial \psi}{\partial r} - q^2 \cos \theta \frac{\partial \psi}{\partial z} - \frac{mq}{r} \psi \right) - (1 - q^2) \frac{\omega^2}{c_s^2} \psi. \quad (7.1.4)$$

All symbols are as defined in §2.1. In particular, H is the density scale height with $H \equiv -dr/d \ln \rho$.

When the density takes a power-law form, both the left-hand side and the first term in the right-hand side are separable in the ellipsoidal coordinates Wu (2005a). Interestingly, when one takes the toy model parameters of Goodman and Lackner (2009), the second term in the right-hand side is also separable. The full equation is now,

$$(\mathcal{F}_1 - \mathcal{F}_2) \psi = 0, \quad (7.1.5)$$

where the operator \mathcal{F}_i is related to the operator \mathcal{E}_i in equation (2.2.10) as

$$\begin{aligned} \mathcal{F}_i &= \mathcal{E}_i + \frac{4\Omega^2 R^2 (1 - \mu^2) \mu^2}{c_{s0}^2 (x_i^2 - \mu^2)} \\ &= \frac{\partial}{\partial x_i} \left[(1 - x_i^2) \frac{\partial}{\partial x_i} \right] - \frac{m^2}{1 - x_i^2} + \frac{2\beta x_i (1 - x_i^2)}{x_i^2 - \mu^2} \frac{\partial}{\partial x_i} \\ &\quad + \frac{2\mu\beta m}{x_i^2 - \mu^2} + \frac{4\Omega^2 R^2 (1 - \mu^2) \mu^2}{c_{s0}^2 (x_i^2 - \mu^2)}. \end{aligned} \quad (7.1.6)$$

Compared to the case where sound speed is taken to be infinity (Wu 2005a), this operator has an extra term – the last term.

It is straightforward to compare the last two terms in the above expression and show that the compressional term (the last term) is smaller by $\Omega^2 R^2 / c_{s0}^2 \ll 1$ as long as the planet is not spinning close to break-up.² This is a constant factor independent of location inside the planet. We can safely ignore this term in our calculation.

Goodman and Lackner (2009) argued that ignoring the compressional term in the boundary condition, however, can cause inaccuracies in the tidal overlap integral and in fact, cause one to overestimate the tidal integral.

We retain the form of the full boundary condition (eq. 2.3.5) at the surface. As such, the boundary condition in equation (2.3.7) in the presence of the compressional term

²Exception occurs when $m = 0$ but these are modes we are not concerned with.

becomes

$$\begin{aligned}\frac{\partial\psi}{\partial x_1}\Big|_{x_1=\mu} &= \left[-\frac{m}{1-\mu^2} + \mu\frac{4\Omega^2 R}{g}\right] \psi|_{x_1=\mu}, \\ \frac{\partial\psi}{\partial x_2}\Big|_{|x_2|=\mu} &= \text{SIGN}[x_2] \left[-\frac{m}{1-\mu^2} + \mu\frac{4\Omega^2 R}{g}\right] \psi|_{|x_2|=\mu},\end{aligned}\quad (7.1.7)$$

where the compressional effects show up as the last terms in the right-hand side. They are of order $\mathcal{O}(\Omega/\Omega_{\text{breakup}})^2$ smaller than the first terms in the right-hand side, except where $m = 0$. The compressional term does not introduce undue influence even close to the surface, because while it increases towards the surface, so do other terms.

So in conclusion, at least for the toy model of Goodman and Lackner (2009), the compressional term introduces negligible difference to both the equation of motion and the boundary condition for inertial modes. Their coupling to the tidal potential should behave similarly to the results presented in Wu (2005b).

7.1.2 Tidal Excitation as an Initial Value Problem

While agreeing that there are wave-like homogeneous solutions, Goodman and Lackner (2009) argued that they were not present before the tidal potential is slowly 'turned on' and therefore should always remain zero. These wave-like responses, for instance, do not satisfy $\mathbf{W} = \nabla \times \mathbf{v} = 0$. Their presence before the 'turned-on' is incompatible with the planet having no extra vorticity other than its own spin-related vorticity, $2\boldsymbol{\Omega}$, initially.

We examine this argument here.

The initial value problem can be specialized to the following question: can a potential force (e.g., the tidal potential) create vorticity in a non-homogeneous, rotating medium? Kelvin's circulation theorem states that circulation around a fluid parcel (measured in the inertial frame) is conserved

$$\frac{d}{dt} \oint \mathbf{v} \cdot d\mathbf{l} = \frac{d}{dt} \int_s \mathbf{W} \cdot d\mathbf{s} = 0, \quad (7.1.8)$$

as long as the fluid is inviscid, is only under potential forces and its equation of state

is barotropic. Or the vorticity is 'frozen-in' with the fluid.³ The background state for a uniformly rotating planet under its self gravity is necessarily barotropic ($p = p(\rho)$) because the hydrostatic equilibrium is (taking $\mathbf{v} = 0$ in the rotating frame in eq. 2.1.4)

$$0 = -\frac{\nabla p}{\rho} - \nabla\Phi + \frac{1}{2}\nabla(\Omega^2 r^2 \sin^2 \theta). \quad (7.1.9)$$

Taking the curl of this yields $\nabla p \times \nabla \rho = 0$.

The circulation theorem still allows local vorticity to be modified through stretching and tilting of the fluid elements. The time evolution of vorticity is obtained below by rewriting the equation of motion into the following form

$$\frac{\partial \mathbf{v}}{\partial t} + \mathbf{W} \times \mathbf{v} = -\frac{1}{\rho} \nabla P - \frac{1}{2} \nabla v^2 - \nabla \Phi, \quad (7.1.10)$$

where we have used the vector identity $1/2 \nabla(\mathbf{v} \cdot \mathbf{v}) = \mathbf{v} \cdot \nabla \mathbf{v} + \mathbf{v} \times \mathbf{W}$. We convert the equation of motion from describing the acceleration to one that describes the vorticity evolution, by taking the curl of both sides of equation 7.1.10

$$\frac{\partial \mathbf{W}}{\partial t} + \nabla \times (\mathbf{W} \times \mathbf{v}) = 0, \quad (7.1.11)$$

where the right-hand side vanishes because we could express the Eulerian pressure perturbation as

$$P' = \Gamma_1 \frac{P}{\rho} \rho'. \quad (7.1.12)$$

With a barotropic background profile, the Eulerian perturbation to $\nabla p \times \nabla \rho$ also vanishes.

Defining a new variable $\mathbf{Z} = \mathbf{W}/\rho$, and using the mass conservation equation, we can recast equation (7.1.11) into a neater form (Vallis 2006),

$$\frac{d\mathbf{Z}}{dt} = \frac{\partial \mathbf{Z}}{\partial t} + (\mathbf{v} \cdot \nabla) \mathbf{Z} = (\mathbf{Z} \cdot \nabla) \mathbf{v}. \quad (7.1.13)$$

So local vorticity is not conserved and can be modified by motion of certain forms.

³Caution against taking the curl directly of the original equation of motion, as $\nabla \times d/dt \neq d/dt \nabla$, the two operators do not commute.

Also, the presence of viscosity can cause vorticity to be diffused across the boundary between fluid elements. Heuristically, the viscosity term appear in the above equation as,

$$\frac{d\mathbf{Z}}{dt} = (\mathbf{Z} \cdot \nabla)\mathbf{v} + \nu \nabla^2 \mathbf{Z}, \quad (7.1.14)$$

where ν is the kinematic viscosity.

So while in the inviscid case, the circulation is exactly conserved and indeed an initially uniformly rotating planet can not harbor inertial oscillations, the presence of viscosity in realistic situations removes this constraint. Vorticity can be transferred between different parts of the planet as necessary. We conjecture that this relaxes the initial condition problem and allows inertial modes to be excited by a potential force.

7.2 Including Compressional Term for the Power-law Density Models

We have also used our pseudo-spectral code to solve for the inertial modes when keeping the compressional term in both the equation of motion and the boundary condition, for a model of $\rho \propto (1 - r^2)^\beta$ and self-consistent pressure and sound-speed profile. As Figure (7.1) shows, the difference between keeping the compressional term or not, is negligible.

7.3 Summary

The neglect of the sound speed (pressure) term in equation (7.1.4) is a common practice when calculating the inertial mode eigenfunction is the main intention. The frequency range of both inertial and sound waves do not to overlap. In rotating objects that are synchronized with the tidal potential, the sound speed term in the inertial wave equation (eq. 7.1.4) is very small by a factor of $\Omega^2 R^2 / c_{s0}^2$, making the anelastic approximation an obvious choice.

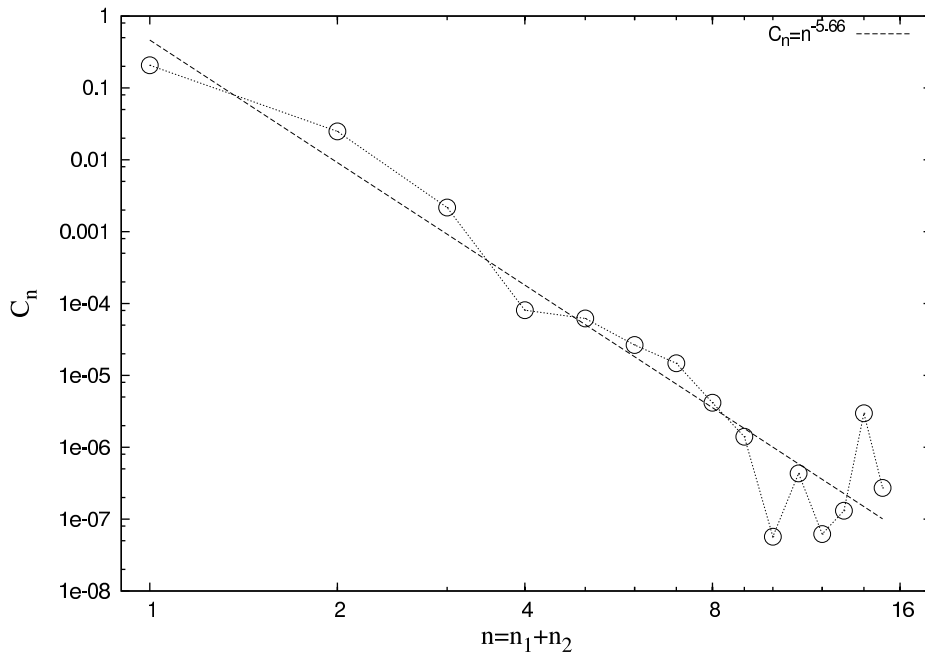


Figure 7.1 The relative tidal overlap integral C_n for inertial modes that are solutions of eq. (7.1.5) for a power law density structure of $\beta = 1.5$. The difference with overlap integrals of similar modes when we neglect the sound speed (see Figure 5.8) term is negligible.

However Goodman and Lackner (2009) commented that neglecting this term tend to overestimate the tidal coupling, instead of obtaining perfect cancellation. We have demonstrated both analytically and numerically that this is not correct, in particular we show that the tidal overlap integrals difference between modes that include the sound speed terms and those that do not is negligible.

The next comment of Goodman and Lackner (2009) to Wu (2005b) toy model, was that the response of the rotating barytropic fluid to a tidal perturbation is entirely long-wavelength. We argue that they have only considered a ‘particular⁴’ fluid response of the rotating fluid to the tidal potential. We have also shown that inertial modes can be excited by slowly varying tidal potential over a rotating fluid that does not harbor modes. The existence of viscosity allows for the transfer of vorticity inside the planet,

⁴In the sense of solutions to the eigenfunction of forced harmonic oscillators, both particular and homogeneous.

with the consequent excitation of inertial waves, including short-wavelength modes.

Chapter 8

Conclusions and future work

In this Thesis we have study inertial modes in fully convective bodies. The inertial mode equation depends explicitly on the density gradient. When general and smooth density profile are used, we have found accurate solutions to this equation.

These solutions represent a substantial improvement in prior studies (Lockitch and Friedman 1999; Lindblom and Ipser 1999; Yoshida and Lee 2000; Papaloizou and Ivanov 2005; Wu 2005a) on inertial modes inside isentropic bodies. Not only do we match the eigenfrequencies and wave behavior of the inertial modes found in previous studies, but also we improve dramatically the convergence of the eigenfunctions.

We believe that the ellipsoidal coordinate system deserves some exploration, as it has been proven that it traces the nodal lines along constant coordinates, making mode labeling an easy task. Labels can be assigned as simple as counting the number of nodes along coordinates ϕ (' m '), x_1 (' n_1 ') and x_2 (' n_2 ').

We have also confirmed numerically in section 7, that the usual practice of discarding the compressional term in the inertial mode equation (2.1.20) is accurate (Lockitch and Friedman 1999; Lee et al. 1992b,a; Dintrans and Ouyed 2001; Papaloizou and Ivanov 2005; Wu 2005a), even in the case of calculating the tidal response of the fluid to an external potential. This term gives rise to sound waves, of much higher frequency than

inertial modes.

As a side (but very interesting) project, we have explored¹ a way to observe indirectly inertial modes, using Saturn’s rings as a seismograph that records the perturbations to Saturn’s external potential due internal density oscillations. So far inertial waves have not being observed outside the Earth, but experiments are underway to detect oscillations in giant planets. Inertial modes are among the most interesting kind to observe as they penetrate deep into the interior of the planet. In section 4.1 we have shown that inertial waves may excite resonant oscillations on Saturn’s rings particles, and, given some conditions, launch observable traveling waves.

Even though we have obtained significant insight about inertial modes, the main purpose of the thesis, understanding tidal dissipation in extrasolar planets has not being achieved. While the accuracy of the solutions for smooth density profiles was high, the tidal quality factor remains a high $Q \sim 10^9$, as predicted for power-law density profiles (Wu 2005b). This result is smaller than the predicted value of the equilibrium tide $Q_{eq} \sim 10^{13}$ (Goldreich and Nicholson 1977), but several orders of magnitude larger than the constrained value of $Q_{observed} \sim 4 \times 10^4$ (Lainey et al. 2009). We used a ‘brute-force’ (§6) approach in order to obtain inertial eigenmodes when a density discontinuity (of 1st or 2nd order) is present. However the global and smooth nature of our proposed solution could not produce reliable eigenmodes when the width of the discontinuity is several times smaller than the wavelength of the modes. A couple of techniques remain unexplored, and we plan to test them in next projects.

We have assumed that the convection zone extend all the way to the outer edge. This may be reasonable for Jupiter but unrealistic for hot-Jupiters where strong irradiation from the host star (Lubow et al. 1997) keeps the atmosphere isothermal (and radiative). When a radiative layer exists, buoyancy becomes important, and this allows the existence of inertial-gravity waves (or ‘Hough-waves’). The structure of the overall inertial mode

¹Based on a similar study of Marley and Porco (1993) for f-modes.

may be considerably affected by this layer. We plan to develop a model that combine our inertial modes in the convective zone with Hough modes in the radiative zone. Ogilvie and Lin (2004) have indicated that the effective boundary condition on the interface implies that the radial displacement there is zero (rigid boundary), while the azimuthal components of the displacement remain continuous across the interface.

The application of this scheme concerns both irradiated exoplanets as well as solar-type stars. Solar-type stars have convective outer envelope and radiative interior – they are in structure, inverted planets. Tidal interaction (as mentioned in the introduction) in solar-type stars is also a puzzle. We hope to use to extend our results in order to explore how internal modes look alike in these rotating bodies.

One of my next research goals, that involves many of the techniques developed during this PhD Thesis project, is to produce observables of non-adiabatic, non-radial pulsations of isolated and rapidly rotating stars. Space observatory mission like COROT, MOST and Kepler are starting to measure high precision asteroseismologic data. Fast rotation adds a non-negligible correction to the pulsation spectrum, identifying and labeling these modes is a task related to the inertial modes.

Rotation deforms the structure of the star, and therefore the structure of the modes. The pseudo-spectral technique may be well suited to this problem, as it gives freedom to chose a coordinate set that best suits the problem. One also is free to choose the set of basis that produce the most accurate and faster results.

Bibliography

- M. Abramowitz and I. A. Stegun. *Handbook of Mathematical Functions*. 1972.
- F. Allard, P. H. Hauschildt, D. R. Alexander, A. Tamanai, and A. Schweitzer. The Limiting Effects of Dust in Brown Dwarf Model Atmospheres. *ApJ*, 556:357–372, July 2001. doi: 10.1086/321547.
- J. D. Anderson and G. Schubert. Saturn’s Gravitational Field, Internal Rotation, and Interior Structure. *Science*, 317:1384–, September 2007. doi: 10.1126/science.1144835.
- G. B. Arfken and H. J. Weber. *Mathematical methods for physicists 6th ed.* 2005.
- M. R. Bate, G. I. Ogilvie, S. H. Lubow, and J. E. Pringle. The excitation, propagation and dissipation of waves in accretion discs: the non-linear axisymmetric case. *MNRAS*, 332:575–600, May 2002. doi: 10.1046/j.1365-8711.2002.05289.x.
- J. Binney and S. Tremaine. *Galactic dynamics*. 1987.
- P. Bodenheimer and J. B. Pollack. Calculations of the accretion and evolution of giant planets The effects of solid cores. *Icarus*, 67:391–408, September 1986. doi: 10.1016/0019-1035(86)90122-3.
- A. P. Boss. Giant planet formation by gravitational instability. *Science*, 276:1836–1839, 1997. doi: 10.1126/science.276.5320.1836.
- J.P. Boyd. *Chebyshev and Fourier Spectral Methods*. Dover, Mineola, second edition edition, 2001.

- G. H. Bryan. The Waves on a Rotating Liquid Spheroid of Finite Ellipticity. *Royal Society of London Philosophical Transactions Series A*, 180:187–219, 1889.
- J. A. Burns, L. E. Schaffer, R. J. Greenberg, and M. R. Showalter. Lorentz resonances and the structure of the Jovian ring. *Nature*, 316:115–119, July 1985. doi: 10.1038/316115a0.
- D. Charbonneau, L. E. Allen, S. T. Megeath, G. Torres, R. Alonso, T. M. Brown, R. L. Gilliland, D. W. Latham, G. Mandushev, F. T. O’Donovan, and A. Sozzetti. Detection of Thermal Emission from an Extrasolar Planet. *ApJ*, 626:523–529, June 2005. doi: 10.1086/429991.
- G. Colombo. Rotational Period of the Planet Mercury. *Nature*, 208:575–+, November 1965. doi: 10.1038/208575a0.
- A. C. M. Correia and J. Laskar. Mercury’s capture into the 3/2 spin-orbit resonance as a result of its chaotic dynamics. *Nature*, 429:848–850, June 2004. doi: 10.1038/nature02609.
- A. C. M. Correia, J. Laskar, and O. N. de Surgy. Long-term evolution of the spin of VenusI. theory. *Icarus*, 163:1–23, May 2003. doi: 10.1016/S0019-1035(03)00042-3.
- Alexandre C. M. Correia and Jacques Laskar. Mercury’s capture into the 3/2 spin-orbit resonance including the effect of core-mantle friction, 2009. URL doi:10.1016/j.icarus.2008.12.034.
- T. G. Cowling. The non-radial oscillations of polytropic stars. *MNRAS*, 101:367–+, 1941.
- J. N. Cuzzi, J. J. Lissauer, and F. H. Shu. Density waves in Saturn’s rings. *Nature*, 292: 703–707, August 1981. doi: 10.1038/292703a0.
- P. J. Davis. *Interpolation and Approximation*, volume 14. 1975.

- D. Deming, M. J. Mumma, F. Espenak, D. E. Jennings, T. Kostiuk, G. Wiedemann, R. Loewenstein, and J. Piscitelli. A search for p-mode oscillations of Jupiter - Serendipitous observations of nonacoustic thermal wave structure. *ApJ*, 343:456–467, August 1989. doi: 10.1086/167719.
- D. Deming, L. J. Richardson, and J. Harrington. 3.8- μm photometry during the secondary eclipse of the extrasolar planet HD209458b. *MNRAS*, 378:148–152, June 2007. doi: 10.1111/j.1365-2966.2007.11754.x.
- M. D. Desch and M. L. Kaiser. Voyager measurement of the rotation period of Saturn’s magnetic field. *Geophys. Res. Lett.*, 8:253–256, March 1981. doi: 10.1029/GL008i003p00253.
- B. Dintrans and R. Ouyed. On Jupiter’s inertial mode oscillations. *A&A*, 375:L47–L50, August 2001. doi: 10.1051/0004-6361:20010989.
- A. Duquennoy and M. Mayor. Multiplicity among solar-type stars in the solar neighbourhood. II - Distribution of the orbital elements in an unbiased sample. *A&A*, 248:485–524, August 1991.
- F. A. Franklin, G. Colombo, and A. F. Cook. A possible link between the rotation of Saturn and its ring structure. *Nature*, 295:128–130, January 1982. doi: 10.1038/295128a0.
- G. Giampieri, M. K. Dougherty, E. J. Smith, and C. T. Russell. A regular period for Saturn’s magnetic field that may track its internal rotation. *Nature*, 441:62–64, May 2006. doi: 10.1038/nature04750.
- G. Giuricin, F. Mardirossian, and M. Mezzetti. Orbital circularization in early-type detached close binaries. *A&A*, 134:365–367, May 1984.
- P. Goldreich and P. D. Nicholson. Turbulent viscosity and Jupiter’s tidal Q. *Icarus*, 30:301–304, February 1977. doi: 10.1016/0019-1035(77)90163-4.

- P. Goldreich and S. Soter. Q in the Solar System. *Icarus*, 5:375–389, 1966. doi: 10.1016/0019-1035(66)90051-0.
- P. Goldreich and S. Tremaine. The dynamics of planetary rings. *ARA&A*, 20:249–283, 1982. doi: 10.1146/annurev.aa.20.090182.001341.
- P. Goldreich and S. Tremaine. The excitation of density waves at the Lindblad and corotation resonances by an external potential. *ApJ*, 233:857–871, November 1979. doi: 10.1086/157448.
- H. Goldstein, C. Poole, and J. Safko. *Classical mechanics*. 2002.
- J. Goodman and C. Lackner. Dynamical Tides in Rotating Planets and Stars. *ApJ*, 696: 2054–2067, May 2009. doi: 10.1088/0004-637X/696/2/2054.
- H.P. Greenspan. *The theory of rotating fluids*. Cambridge University Press, Cambridge, 1980. ISBN 0-521-29956-X.
- T. Guillot. A comparison of the interiors of Jupiter and Saturn. *Planet. Space Sci.*, 47: 1183–1200, October 1999.
- T. Guillot. THE INTERIORS OF GIANT PLANETS: Models and Outstanding Questions. *Annual Review of Earth and Planetary Sciences*, 33:493–530, January 2005. doi: 10.1146/annurev.earth.32.101802.120325.
- T. Guillot and A. P. Showman. Evolution of “51 Pegasus b-like” planets. *A&A*, 385: 156–165, April 2002. doi: 10.1051/0004-6361:20011624.
- T. Guillot, D. Gautier, G. Chabrier, and B. Mosser. Are the giant planets fully convective? *Icarus*, 112:337–353, December 1994. doi: 10.1006/icar.1994.1188.
- T. Guillot, A. Burrows, W. B. Hubbard, J. I. Lunine, and D. Saumon. Giant Planets at Small Orbital Distances. *ApJ*, 459:L35+, March 1996. doi: 10.1086/309935.

- T. Guillot, D. J. Stevenson, W. B. Hubbard, and D. Saumon. *The interior of Jupiter*, pages 35–57. 2004.
- M. M. Hedman, J. A. Burns, M. S. Tiscareno, P. D. Nicholson, and C. C. Porco. Possible Resonances with Saturn’s Rotation in the Rings. *AGU Fall Meeting Abstracts*, pages A189+, December 2007.
- J. B. Holberg, W. T. Forrester, and J. J. Lissauer. Identification of resonance features within the rings of Saturn. *Nature*, 297:115–120, May 1982. doi: 10.1038/297115a0.
- S. S. Hough. On the Application of Harmonic Analysis to the Dynamical Theory of the Tides. Part I. On Laplace’s ”Oscillations of the First Species,” and on the Dynamics of Ocean Currents. *Royal Society of London Philosophical Transactions Series A*, 189: 201–257, 1897.
- W. B. Hubbard. Tides in the giant planets. *Icarus*, 23:42–50, September 1974. doi: 10.1016/0019-1035(74)90102-X.
- P. Hut. Tidal evolution in close binary systems. *A&A*, 99:126–140, June 1981.
- J. R. Ipser and L. Lindblom. The oscillations of rapidly rotating Newtonian stellar models. *ApJ*, 355:226–240, May 1990. doi: 10.1086/168757.
- J. R. Ipser and L. Lindblom. On the adiabatic pulsations of accretion disks and rotating stars. *ApJ*, 379:285–289, September 1991. doi: 10.1086/170503.
- P. B. Ivanov and J. C. B. Papaloizou. Dynamic tides in rotating objects: orbital circularization of extrasolar planets for realistic planet models. *MNRAS*, 376:682–704, April 2007. doi: 10.1111/j.1365-2966.2007.11463.x.
- Z. Kopal. *Close binary systems*. 1959.

- V. Lainey, J.-E. Arlot, Ö. Karatekin, and T. van Hoolst. Strong tidal dissipation in Io and Jupiter from astrometric observations. *Nature*, 459:957–959, June 2009. doi: 10.1038/nature08108.
- K. Lambeck. *Geophysical geodesy - The slow deformations of the earth*. 1988.
- U. Lee, T. E. Strohmayer, and H. M. van Horn. Inertial mode oscillations of Jupiter. *ApJ*, 397:674–685, October 1992a. doi: 10.1086/171823.
- U. Lee, T. E. Strohmayer, and H. M. van Horn. Inertial mode oscillations of Jupiter. *ApJ*, 397:674–685, October 1992b. doi: 10.1086/171823.
- C. C. Lin and F. H.-S. Shu. Density wave theory of spiral structure. In *Astrophysics and general relativity, Vol. 2, p. 235 - 329*, volume 2, pages 235–329, 1971.
- L. Lindblom and J. R. Ipser. Generalized r-modes of the Maclaurin spheroids. *Phys. Rev. D*, 59(4):044009–+, February 1999. doi: 10.1103/PhysRevD.59.044009.
- K. H. Lockitch and J. L. Friedman. Where are the R-Modes of Isentropic Stars? *ApJ*, 521:764–788, August 1999. doi: 10.1086/307580.
- S. H. Lubow, C. A. Tout, and M. Livio. Resonant Tides in Close Orbiting Planets. *ApJ*, 484:866–+, July 1997. doi: 10.1086/304369.
- G. J. F. MacDonald. Tidal Friction. *Reviews of Geophysics and Space Physics*, 2:467–541, 1964.
- M. S. Marley and C. C. Porco. Planetary acoustic mode seismology - Saturn’s rings. *Icarus*, 106:508–+, December 1993. doi: 10.1006/icar.1993.1189.
- M. S. Marley, W. B. Hubbard, and C. C. Porco. Saturnian Nonradial p - Mode Oscillations and C Ring Structure. In *Bulletin of the American Astronomical Society*, volume 19 of *Bulletin of the American Astronomical Society*, pages 889–+, June 1987.

- M. Mayor and J. C. Mermilliod. Orbit Circularization Time in Binary Stellar Systems. In A. Maeder and A. Renzini, editors, *Observational Tests of the Stellar Evolution Theory*, volume 105 of *IAU Symposium*, pages 411–+, 1984.
- T. Mazeh. Observational Evidence for Tidal Interaction in Close Binary Systems. In M.-J. Goupil and J.-P. Zahn, editors, *EAS Publications Series*, volume 29 of *EAS Publications Series*, pages 1–65, 2008. doi: 10.1051/eas:0829001.
- S. Meibom and R. D. Mathieu. A Robust Measure of Tidal Circularization in Coeval Binary Populations: The Solar-Type Spectroscopic Binary Population in the Open Cluster M35. *ApJ*, 620:970–983, February 2005. doi: 10.1086/427082.
- N. Meyer-Vernet and B. Sicardy. On the physics of resonant disk-satellite interaction. *Icarus*, 69:157–175, January 1987. doi: 10.1016/0019-1035(87)90011-X.
- F. Mignard. The lunar orbit revisited. III. *Moon and Planets*, 24:189–207, April 1981. doi: 10.1007/BF00910608.
- B. Militzer, W. B. Hubbard, J. Vorberger, I. Tamblyn, and S. A. Bonev. A Massive Core in Jupiter Predicted from First-Principles Simulations. *ApJ*, 688:L45–L48, November 2008. doi: 10.1086/594364.
- A. Moorhead and F. Adams. Eccentricity Evolution of Giant Planet Orbits due to Circumstellar Disk Torques. In *AAS/Division of Dynamical Astronomy Meeting*, volume 38 of *AAS/Division of Dynamical Astronomy Meeting*, pages 04.02–+, July 2007.
- B. Mosser. Giant planets seismology. In E. Fossat, editor, *Sounding Solar and Stellar Interiors*, volume 181 of *IAU Symposium*, pages 251–+, 1997.
- B. Mosser, D. Mekarnia, J. P. Maillard, J. Gay, D. Gautier, and P. Delache. Seismological observations with a Fourier transform spectrometer - Detection of Jovian oscillations. *A&A*, 267:604–622, January 1993.

- B. Mosser, P. Galdemard, P. Lagage, E. Pantin, M. Sauvage, P. Lognonne, D. Gautier, F. Billebaud, T. Livengood, and H. U. Kaufl. Impact Seismology: A Search for Primary Pressure Waves Following Impacts A and H. *Icarus*, 121:331–340, June 1996. doi: 10.1006/icar.1996.0091.
- C. D. Murray and S. F. Dermott. *Solar System Dynamics*. February 2000.
- G. W. Null, E. L. Lau, E. D. Biller, and J. D. Anderson. Saturn gravity results obtained from Pioneer 11 tracking data and earth-based Saturn satellite data. *AJ*, 86:456–468, March 1981. doi: 10.1086/112905.
- G. I. Ogilvie and D. N. C. Lin. Tidal Dissipation in Rotating Giant Planets. *ApJ*, 610: 477–509, July 2004. doi: 10.1086/421454.
- J. Papaloizou and J. E. Pringle. Non-radial oscillations of rotating stars and their relevance to the short-period oscillations of cataclysmic variables. *MNRAS*, 182:423–442, February 1978.
- J. C. B. Papaloizou and P. B. Ivanov. Oscillations of rotating bodies: a self-adjoint formalism applied to dynamic tides and tidal capture. *MNRAS*, 364:L66–L70, November 2005. doi: 10.1111/j.1745-3933.2005.00107.x.
- H. Poincaré. Mémoires et observations. Sur l'équilibre d'une masse fluide animée d'un mouvement de rotation. *Bulletin Astronomique, Serie I*, 2:109–118, 1885.
- W. H. Press, S. A. Teukolsky, W. T. Vetterling, and B. P. Flannery. *Numerical recipes in FORTRAN. The art of scientific computing*. 1992.
- E. S. G. Rainey and O. Aharonson. Estimate of Tidal Q of Mars Using MOC Observations of the Shadow of Phobos. In S. Mackwell and E. Stansbery, editors, *37th Annual Lunar and Planetary Science Conference*, volume 37 of *Lunar and Planetary Inst. Technical Report*, pages 2138–+, March 2006.

- P. L. Read, T. E. Dowling, and G. Schubert. Saturn's rotation period from its atmospheric planetary-wave configuration. *Nature*, 460:608–610, May 2009. doi: 10.1038/nature04750.
- P. A. Rosen and J. J. Lissauer. The Titan-1:0 nodal bending wave in Saturn's Ring C. *Science*, 241:690–694, August 1988. doi: 10.1126/science.241.4866.690.
- P. A. Rosen, G. L. Tyler, E. A. Marouf, and J. J. Lissauer. Resonance structures in Saturn's rings probed by radio occultation. II - Results and interpretation. *Icarus*, 93: 25–44, September 1991. doi: 10.1016/0019-1035(91)90161-L.
- D. Saumon and T. Guillot. Shock Compression of Deuterium and the Interiors of Jupiter and Saturn. *ApJ*, 609:1170–1180, July 2004. doi: 10.1086/421257.
- D. Saumon, G. Chabrier, and H. M. van Horn. An Equation of State for Low-Mass Stars and Giant Planets. *ApJS*, 99:713–+, August 1995. doi: 10.1086/192204.
- A. K. Schenk, P. Arras, É. É. Flanagan, S. A. Teukolsky, and I. Wasserman. Non-linear mode coupling in rotating stars and the r-mode instability in neutron stars. *Phys. Rev. D*, 65(2):024001–+, January 2002. doi: 10.1103/PhysRevD.65.024001.
- F.-X. Schmider, E. Fossat, and B. Mosser. Possible detection of Jovian global oscillations. *A&A*, 248:281–291, August 1991.
- S. Seager, L. J. Richardson, B. M. S. Hansen, K. Menou, J. Y.-K. Cho, and D. Deming. On the Dayside Thermal Emission of Hot Jupiters. *ApJ*, 632:1122–1131, October 2005. doi: 10.1086/444411.
- F. H. Shu, J. N. Cuzzi, and J. J. Lissauer. Bending waves in Saturn's rings. *Icarus*, 53: 185–206, February 1983. doi: 10.1016/0019-1035(83)90141-0.
- B. A. Smith, L. Soderblom, R. F. Beebe, J. M. Boyce, G. Briggs, A. Bunker, S. A. Collins, C. Hansen, T. V. Johnson, J. L. Mitchell, R. J. Terrile, M. H. Carr, A. F.

- Cook, J. N. Cuzzi, J. B. Pollack, G. E. Danielson, A. P. Ingersoll, M. E. Davies, G. E. Hunt, H. Masursky, E. M. Shoemaker, D. Morrison, T. Owen, C. Sagan, J. Veverka, R. Strom, and V. E. Suomi. Encounter with Saturn - Voyager 1 imaging science results. *Science*, 212:163–191, April 1981. doi: 10.1126/science.212.4491.163.
- B. A. Smith, L. Soderblom, R. M. Batson, P. M. Bridges, J. L. Inge, H. Masursky, E. Shoemaker, R. F. Beebe, J. Boyce, G. Briggs, A. Bunker, S. A. Collins, C. Hansen, T. V. Johnson, J. L. Mitchell, R. J. Terrile, A. F. Cook, J. N. Cuzzi, J. B. Pollack, G. E. Danielson, A. P. Ingersoll, M. E. Davies, G. E. Hunt, D. Morrison, T. Owen, C. Sagan, J. Veverka, R. Strom, and V. E. Suomi. A new look at the Saturn system - The Voyager 2 images. *Science*, 215:504–537, January 1982. doi: 10.1126/science.215.4532.504.
- D. J. Stevenson. Are Saturn's rings a seismograph for planetary inertial oscillations? *Eos, Transactions of American Geophysical Union*, 63:1020, August 1982.
- D. J. Stevenson and E. E. Salpeter. The phase diagram and transport properties for hydrogen-helium fluid planets. *ApJS*, 35:221–237, October 1977. doi: 10.1086/190478.
- A. Toomre. On the gravitational stability of a disk of stars. *ApJ*, 139:1217–1238, May 1964. doi: 10.1086/147861.
- W. Unno, Y. Osaki, H. Ando, H. Saio, and H. Shibahashi. *Nonradial oscillations of stars*. 1989.
- G. K. Vallis. *Atmospheric and Oceanic Fluid Dynamics*. November 2006. doi: 10.2277/0521849691.
- M. G. Witte and G. J. Savonije. Orbital evolution by dynamical tides in solar type stars. Application to binary stars and planetary orbits. *A&A*, 386:222–236, April 2002. doi: 10.1051/0004-6361:20020155.

- Y. Wu. Origin of Tidal Dissipation in Jupiter. I. Properties of Inertial Modes. *ApJ*, 635: 674–687, December 2005a. doi: 10.1086/497354.
- Y. Wu. Origin of Tidal Dissipation in Jupiter. II. The Value of Q. *ApJ*, 635:688–710, December 2005b. doi: 10.1086/497355.
- Y. Wu. Tidal Circularization and Kozai Migration. In D. Deming & S. Seager, editor, *Scientific Frontiers in Research on Extrasolar Planets*, volume 294 of *Astronomical Society of the Pacific Conference Series*, pages 213–216, 2003.
- C. F. Yoder. Astrometric and Geodetic Properties of Earth and the Solar System. In T. J. Ahrens, editor, *Global Earth Physics: A Handbook of Physical Constants*, pages 1–+, 1995.
- S. Yoshida and U. Lee. Inertial Modes of Slowly Rotating Isentropic Stars. *ApJ*, 529: 997–1010, February 2000. doi: 10.1086/308312.
- J.-P. Zahn. Tidal friction in close binary stars. *A&A*, 57:383–394, May 1977a.
- J.-P. Zahn. The dynamical tide in close binaries. *A&A*, 41:329–344, July 1975.
- J.-P. Zahn. Tidal friction in close binary stars. *A&A*, 57:383–394, May 1977b.
- J.-L. Zhou, D. N. C. Lin, and Y.-S. Sun. Post-oligarchic Evolution of Protoplanetary Embryos and the Stability of Planetary Systems. *ApJ*, 666:423–435, September 2007. doi: 10.1086/519918.